8-2008

INFERRING MECHANICAL RESONANCES IN MICRO - AND NANOCANTILEVERS USING THE HARMONIC DETECTION OF RESONANCE (HDR) METHOD TO DEVELOP A NOVEL SENSING PLATFORM

Gayatri Keskar
Clemson University, gkeskar@clemson.edu

INFERRING MECHANICAL RESONANCES IN MICRO - AND NANOCANTILEVERS USING THE HARMONIC DETECTION OF RESONANCE (HDR) METHOD TO DEVELOP A NOVEL SENSING PLATFORM

A Dissertation
Presented to
the Graduate School of
Clemson University

In Partial Fulfillment
of the Requirements for the Degree
Doctor of Philosophy
Materials Science and Engineering

---

by
Gayatri Keskar
August 2008

Accepted by:
Dr. Apparao Rao, Committee Chair
Dr. John Ballato
Dr. Jian Luo
Dr. Igor Luzinov

ABSTRACT

During the past two decades, advances in microelectromechanical systems (MEMS) have spurred efforts worldwide to develop sensing platforms based on smart microcantilevers. A microcantilever beam is one of the simplest MEMS structures which forms the basis for portable, fast and highly sensitive schemes that are capable of measuring small deflections in static or dynamic response due to changes in external parameters such as mass, pressure, charge, etc.

In this dissertation, I mainly focus on MEMS sensors with transducers in the form of microcantilevers. Variations in the microcantilever's response such as resonant frequency, amplitude, phase and quality factor when exposed to external stimuli are measured. Recently, we have developed a fully electrical sensing platform called the harmonic detection of resonance (HDR) method by which a silicon microcantilever (or a multiwalled carbon nanotube) can be electrically actuated and its resonance parameters electrically detected [4, 5] through capacitance changes. It is well known that a large interfering signal coming from the inherent parasitic capacitance in the circuit at the driving frequency Ω, is present in the platforms which use the capacitive readout method. However, we found that by driving the cantilever at Ω and detecting its response at higher harmonics of Ω, the parasitic capacitance can be avoided, facilitating the measurement of dynamic capacitance with high sensitivity in micro and nano-cantilevers [1, 2]. A significant part of this dissertation is devoted to the study of the nonlinear dynamics of microcantilevers under varying gas environments and pressures using HDR

[3]. I also discuss the characteristics of an electrostatically driven microcantilever which exhibits Duffing-like behavior using HDR. The first experimental demonstration of its potential use as a highly sensitive sensing platform is discussed. [4]. We also discuss the behavior of an unfunctionalized microcantilever sensor which can be used for active sensing of gaseous species under ambient conditions. Our sensing platform measures the changes in the mechanical response (in amplitude and/or phase) of the vibrating microcantilever in air at its resonant frequency when exposed to several vapors and gases [5]. Finally I present the preliminary results on sensing toxic gases using functionalized microcantilevers.

In the final chapter, I present evidence for the fact that HDR method is scaleable and can be adapted for nanoscale cantilevers. In particular, I introduce the reader to bending modulus measurements of multiwalled carbon nanotubes performed in Prof. Rao's group. One of the key factors in these measurements is an accurate knowledge of density of carbon nanotubes. I provide in-depth discussion of the gradient sedimentation technique which enables one to measure the density of both single- and multi-walled carbon nanotubes.

DEDICATION

I dedicate this work to my mother, Madhavi Keskar, father Deepak Keskar and to my brother Hrishikesh Keskar. I take this opportunity to express my sincere gratitude towards all my family for their unconditional love, good wishes and continuous support.

ACKNOWLEDGMENTS

I would like to thank those who were instrumental in my development as a scientist especially my advisor, Dr. Apparao Rao; Dr. Malcolm Skove; my labmate, Bevan Elliott and my roommate Sonia Ramnani.

Dr. Apparao Rao, has given me his valuable guidance and wholehearted support for all this time. My research has been inspiring and challenging with his constructive criticism and words of encouragement in all aspects of my work. Besides being an excellent advisor, he has been a fatherly figure to me. I am fortunate to have him as my mentor in my life. I am very grateful to all other committee members: Dr. J. Ballato, Dr. J. Luo and Dr. I. Luzinov for reviewing my dissertation.

Dr. Malcolm Skove has been actively involved in this project right from day one. It was his knowledge of the electronics and the lock-in amplifiers that helped us develop the HDR method. He has worked out the theory for HDR particularly for chapters 3 and 4. We have worked closely together in the lab for the last three years everyday learning something new from him.

Bevan has always guided me in the right direction with his valuable inputs. In addition to his contributions to this research, Bevan has become a great friend. He has always inspired me to keep going and has always trusted that I would overcome each and every challenge faced in graduate school and in life.

Sonia with whom I have a relationship like no one else, has always motivated me with a positive energy and right spirit. I am very fortunate to have her everytime with me

to solve all my problems which mean a lot to me. To Sonia, without your unconditional love and support, I would not have ever made it this far.

I would like to thank Jay Gaillard who has developed this HDR technique for teaching me HDR which is the backbone of my work. I have spent the most important period of my graduate school learning all about MEMS and NEMS from him. Some of his results about measuring the resonance on nanoscale are explained briefly in chapter 6. I would also like to thank Razvan for developing the mathematical model for determining the density of carbon nanotubes along with the determination of Young's modulus of a Multiwall carbon nanotube used in chapter 6. I would like to acknowledge those in the group with whom I have worked directly or indirectly and have spent time enjoying this graduate experience like Rahul, Ted, Jason, J D, Rama and Yang.

I would like to thank Qi Lu and Dr. L. Larcom for their valuable contribution in the gradient sedimentation study. I would like also to thank Joan and Amar at the AMRL for their willingness to lend their expertise, time and effort which were necessary in the completion of this dissertation. Special thanks to the staff of Department of Physics and Astronomy and Materials Science and Engineering.

Last but not the least I give my deepest and most sincere gratitude to all my friends for their friendship and support throughout my graduate career. Special thanks to my close friends Malay, Gauri, Nikhil, Niten, Tanuja, Radhika, Shail and Sudeep for making this whole journey towards my doctorate so memorable.

TABLE OF CONTENTS

Page

Table of Contents (Continued)

Page

LIST OF TABLES

LIST OF FIGURES

List of Figures (Continued)

Figure Page

List of Figures (Continued)

Figure Page

List of Figures (Continued)

Figure Page

List of Figures (Continued)

Figure Page

List of Figures (Continued)

Figure Page

List of Figures (Continued)

Figure Page

List of Figures (Continued)

Figure Page

CHAPTER ONE

INTRODUCTION

The advent of microprocessors has enabled the development of sensors which can be actuated by different methods to detect and monitor the various analytes [6]. Nevertheless, the challenges faced in the development of improved sensing platforms still continue with a view towards achieving enhanced selectivity, markedly reduced power dissipation and rapid response at a reasonable cost. The invention of atomic force microscopy (AFM) which primarily involves microfabricated cantilevers is an important milestone for sensors based on MEMS. The functionality of MEMS sensors heavily rely on the mechanical displacements and deformations of their micromachined components such as single-clamped suspended beams (cantilevers), double-clamped suspended beams (bridges) or suspended diaphragms [7].

The latest breakthrough developments in IC and CMOS technologies offer smart cantilevers [8], extremely small cantilevers, or large arrays of cantilevers. The commercially available cantilevers are typically made of silicon, silicon nitride or silicon oxide in a variety of different shapes, dimensions and force sensitivities. Thus, individual or arrays of microcantilevers are ideal candidates for chemical and biological sensors. Label free systems can be easily quantified (in gas phase) and can be highly sensitive compared to conventional analytical methods. Microcantilever based sensors offer various benefits such as requirement of only minute sample volumes, ability to detect cantilever motion with subnanometer precision, ability to be fabricated into a multi-element sensor array and ability to work in air, vacuum or in liquids and convenient

parallelization because of batch silicon micro-machining techniques [9]. The microcantilevers can be heated and cooled with a thermal time-constant less than a millisecond due to their low thermal mass. This is beneficial for regenerating the sensor through rapid reversal of molecular absorption processes which is essential for *in situ* sensing platforms [10].

History of microcantilever based sensors

These miniaturized devices perform based on the underlying principle of mechanical stress and deformations induced due to variations in the surrounding environment. Since the 1920s, macroscopic cantilever devices and mechanical resonators were well established for measuring the mechanical responses to adsorbate-induced stresses using optical means in chemical and biological sensors. But, macroscale mechanical transducers could hardly satisfy the demand for highly specific sensing performance because of extremely high susceptibility to external vibrations stemming from large suspended masses and relatively low resonance frequencies and thus 1/f noise. Hence, these transducers failed to achieve practical importance until microcantilevers and more precise detection schemes were widely available enabling from a macro to micro-mechanical transition [7].

Resonance Response

Depending on the measured parameter i.e. either cantilever deflection or resonance frequency, the mode of cantilever operation can be referred to as (1) static: for example, functionalizing one side of the cantilever with a sensing layer so that the cantilever bends due to the surface stress due to a specific reaction between the analyte and the sensing layer [3] or (2) dynamic: detects the shift in resonant frequency of the cantilever due to specific mass adsorption (Fig. 1.1) [11]

Static cantilever deflections may arise from either external forces acting on the cantilever or intrinsic stresses generated within or on the cantilever surface. These intrinsic stresses may be result from thermal expansion, interfacial processes or physicochemical variations of the cantilever. In the dynamic mode, the resonant frequency essentially varies with the adsorbed mass and viscoelastic properties of the medium around the cantilever. The broad range of transduction modes stems from the fact that a stimulus of each type may affect the cantilever directly or may undergo several transformations before affecting the mechanical parameters of the cantilever under study. The transduction efficiency of the static mode increases with the reduction of the stiffness of the cantilever. Hence, longer cantilevers with small spring constant are suitable for the operation in the static (adsorption-bending) mode. Whereas shorter, higher resonant frequency cantilevers are ideal for the frequency shift based approach The sensitivity of the resonant mode increases with the operation frequency[12].

Sensing Techniques

Microcantilever sensors can be physical, chemical, or biological sensors depending upon the nature of the input stimuli. The shift in the resonant frequency can be used as an indicator to detect any change in the surrounding environment that affects the mass, elasticity or damping of the microcantilever. Applications as sensitive physical sensors include detection of the changes in the physical parameters such as viscosity, pressure, density, and flow rate [13]. The detection limit of the microcantilever based physical sensors is ~ 1 pN for measuring forces and for displacement measurements, 0.1 nm. The viscosity of gases and liquids can also be determined using the resonance response of a microcantilever [14].

Using microcantilever based biosensors, the detection of protein adsorption, antibody-antigen recognition, and DNA hybridization has been successfully demonstrated [15, 16] as they can be operated in liquid. However, the liquid medium damps the resonance response of a microcantilever to approx. one order of magnitude smaller than while operating in air [17-19]. Thus the main problem is the high damping and not the biological preparation for the microcantilever based biosensors.

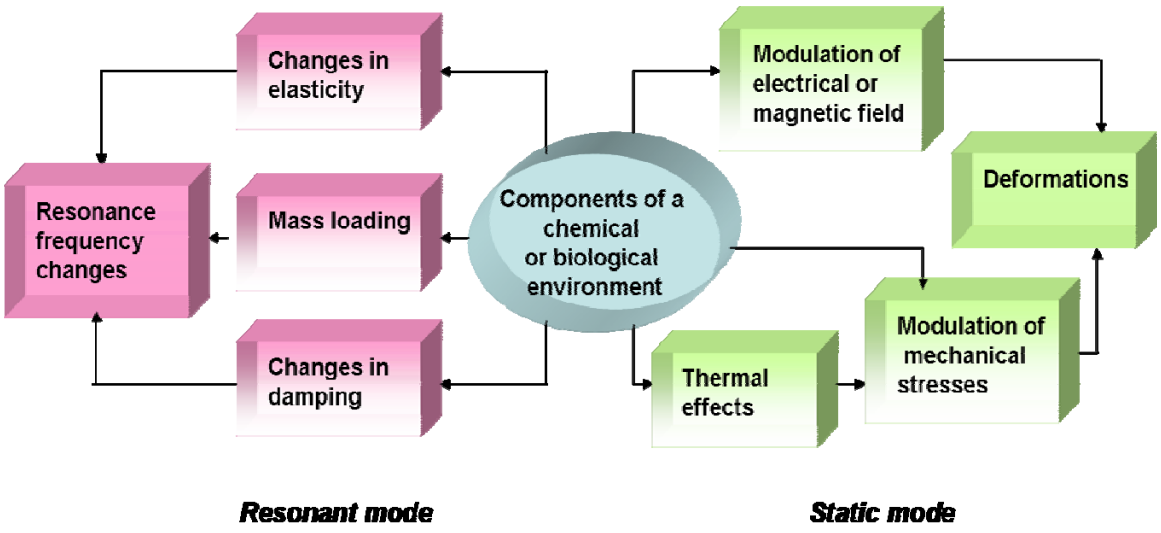

Figure 1.1 Various transduction mechanisms implemented by cantilever transducers to convert input stimuli into output signals [7].

A chemical sensor comprised of a physical transducer and a chemically selective layer produces output signals as a response to the chemical stimuli. The affinity of the targeted analytes for the specific binding sites in the highly selective receptor layers helps in the recognition of various molecules. There can be two types of gas- solid interactions: bulk-like absorption and surface- like adsorption [20]. In general, adsorption decreases the surface energy. The extent of cantilever deflection depends directly on the changes in the surface energy due to molecular adsorption. This in turn varies with the deviation in free energy per adsorbate and the total number of molecules involved in the adsorption process.

The adsorption-induced forces are large enough to rearrange the lattice locations of the surface and subsurface atoms on a clean surface, causing surface relaxations and reconstructions. Molecular adsorption on a cantilever coated on only one side causes bending because of adsorption induced changes in the surface stress [10, 21, 22]. Whereas for the cantilever with two differently coated chemical surfaces, molecular adsorption results in a differential stress between the top and bottom surfaces of the cantilever leading to it's bending.

The ability to functionalize one surface of the silicon microcantilever so that a given molecular species will be preferentially bound to that surface upon exposure to a vapor stream vastly enhances the selectivity of the detection. Thus functionalized microcantilevers enable the sensor to perform as chemical/artificial nose [9]. Analyte detection using miniaturized chemical sensors has various applications in different fields such as quality and process control, biomedical analysis, gas-sensing devices, forensic investigations, fragrance design and oenology [23].

Sensor Applications

1) Mass sensor - A microcantilever can be used as a microbalance with femtogram mass resolution [9] by measuring the shifts in the resonant frequency. For mass sensitive gas sensors, the sensors response depends on the mass of an absorbed analyte which in turn depends on the concentration of the analyte and its molecular weight. Mass sensitive transducers are the active devices and are commonly classified as Bulk Acoustic Wave (BAW) and Surface Acoustic Wave (SAW) sensors. These

transducers are piezoelectrically excited in which the resonance frequency is a measure of the mass of the transducer, and is affected by the analyte concentration to be determined [24].

2) Temperature sensor - Berger et al. [25] and Thundat et al. [13, 26] pioneered cantilever based sensors and their work involved the measurements nanoscale deflections due to an external stimuli. The bending along with the static deflections of the cantilever has been attributed to the surface stress changes involving heat transfer from chemical reactions or phase transitions.

3) Optical sensors - Thundat et al. [27] also demonstrated the detection of ultraviolet radiation at pJ levels based on the microcantilevers coated with UV- sensitive polymers. The cross-linking of a polymer due to UV- radiation exposure results in a change in the cantilever resonant frequency and the spring constant.

4) Magnetic sensors – Many research groups have reported the measurements of the magnetic properties of magnetic and superconducting materials using a microcantilever [28-30]. Using the torque induced by an applied field, Rossel et al [28] studied the magnetization of small (< microgram) samples mounted at the ends of a cantilever with peizoresistive read-out (discussed in next chapter). Such cantilevers are capable of sensing torques that are approx. 10^{-14} Nm. In case of an applied field of 1T, magnetic moments as small as approx. $10^{-14}Am^2$ can be measured with microcantilevers, which is 3 orders of magnitude greater than the commercial SQUID (superconducting quantum interference device) magnetometers.

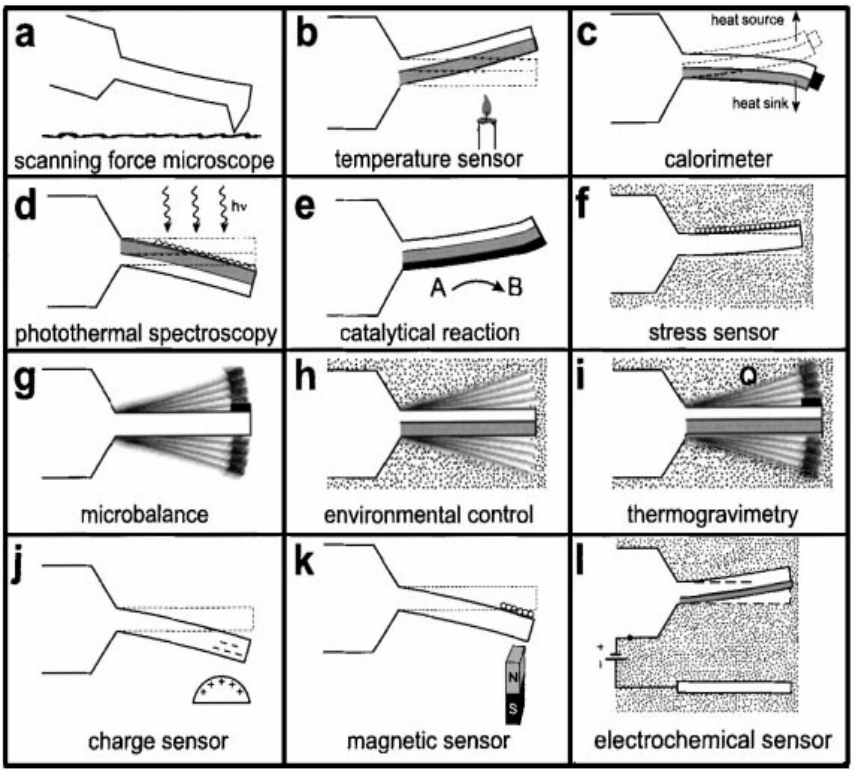

Figure 1.2: Summary of the wide spectrum of applications that can be realized using micro-cantilevers [23].

Figure 1.2 summarizes some of the techniques which have evolved from a scanning force microscope (SFM) which uses a smart cantilever. A cantilever with an integrated sharp tip can be used to study the surface profile of a sample as shown in Fig. 1.2(a) [31]. A one side metal-coated cantilever is useful as a micron scale temperature sensor in which the bending is induced by the temperature change around the microcantilever. The small thermal mass of the cantilevers enables very small heat energy (~ nJ) to be measured and accurate changes in temperature have been measured

with a resolution of ≈10 μK (Fig. 1.2(b)). Detection of exothermic and endothermic phase transitions involving ng amounts of material attached to the cantilever is feasible [32] (Fig. 1.2(c)). Photothermal spectroscopy performed on the biomaterial cantilevers can be used to measure the heat produced upon light irradiation, Fig. 1.2.(d) [33]. Fig. 1.2(e) [34] describes the reaction of hydrogen and oxygen forming a water molecule catalyzed by a platinum coated biomaterial cantilever using the oscillatory behavior (the figure indicates the bending). Gold-thiol chemistry has been reported to self assemble a monolayer of akylthiols on a gold coated cantilever. This in turn causes a change in the surface stress which (as seen in Fig. 1.2(f)) [35] increases with increasing the chain length of the alkylthiols. The change in mass due to gain or loss in the mass of the sample attached to the apex of a cantilever can be measured by determining the shift in the resonant frequency. The mass change that can be detected is in the range of 1 pg, Fig. 1.2(g). The change in the resonant frequency of a functionalized cantilever can be used to monitor the variation in the environmental conditions (such as change in humidity based on temperature). For thermogravimetric applications, the change in the mass of a sample can be monitored as a function of the temperature by mounting a sample on the apex of the vibrating cantilever, Fig 1.2(i) [36]. Using a cantilever deflection scheme, the various forces such as electrostatic forces Fig. 1.2(j), or magnetic forces Fig. 1.2(k), can also be detected.

CHAPTER TWO

GENERAL THEORY

Actuation Methods

Microcantilever based sensors often measure shifts in the resonant frequency. The cantilever can be driven by just the thermal noise k_BT in the absence of external actuation, where k_B is the Boltzman constant and T is the temperature [10]. However, at room temperature the thermal energy is small and dependent on the environment in which the cantilever resonates. Hence, cantilevers are often driven externally using common actuation techniques for reliable use in many applications. The common actuation techniques implemented to drive the microcantilevers externally are discussed here,

Piezoelectric actuation

The most commonly used actuation method to drive the cantilever is a piezoelectric device. They are used extensively with AFM microcantilevers. Commercially available scanning probe microscopes actuate the cantilevers by an externally driving a piezoelectric device mounted close to the cantilever [38]. This method utilizes certain crystalline materials, such as $PbZrTiO_3$, which expand and contract upon application of an electric field. For the AFM, a piezoelectric sheet is sandwiched between two metal plates. One sheet is attached to the frame of the AFM. A small (~3mm × 5mm rectangle) chip is placed on the other and the cantilever attached to the chip. The frequency of the applied voltage is swept to provide a spectrum of the

response of the cantilever. From this spectrum, the fundamental resonant frequency of the cantilever can be determined. The resonance induced with this method has limitations while operating in liquid.

Magnetic actuation

Magnetic forces can be used for the actuation of the cantilever. These forces can be induced by evaporating a magnetic layer on the cantilever or placing a magnetic particle at the end of the cantilever and applying an external magnetic field by using a solenoid. This method of actuation is used for AFM cantilevers in the tapping mode while operating in liquids and for biological samples [37-41].

Electrostatic actuation

Among all the possible actuation techniques, electrostatic actuation is the most preferred method in MEMS and nanoelectromechanical systems NEMS [42-44]. It is convenient to incorporate this technique while fabricating microcantilever based systems. A parallel plate configuration is implemented between the counter electrode and the cantilever in order to vibrate the latter at its resonance. The basic principle here is to determine the resonant frequency of the cantilever by sweeping the frequency of the ac voltage. As can be seen in Fig. 2.1, an ac and a dc voltage are applied to counter electrode, while the other plate which is a cantilever is connected to ground. The time dependent force drives the motion of the cantilever, and when its frequency matches a

resonance of the cantilever, the amplitude of oscillating cantilever attains a maximum value.

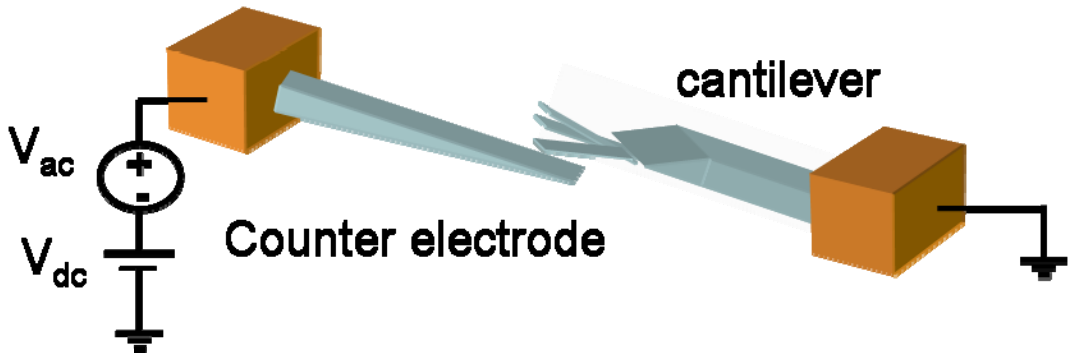

Figure 2.1: Schematic illustration of electrostatic actuation. The ac voltage along with dc offset is applied to the counter electrode. The cantilever is grounded to maintain a potential difference. The cantilever is driven into resonance by sweeping the frequency of ac voltage.

Detection methods

The vital part of any cantilever based sensor is its deflection detection scheme from which the changes in a specific parameter (directly related to its deflection in real time) can be determined, often with at least nanometer accuracy [7]. In general, the amplitude and the phase with respect to the driving force of a Fourier component of the motion of the cantilever are measured as a function of the driving frequency. The detection schemes are broadly classified as optical and electrical. While the optical beam

deflection technique is efficient and widely used in devices involving microcantilevers, it is ineffective in the emerging technologies which involve the use of nanocantilevers. This is due to the fact that nanocantilevers cannot reflect sufficient light for accurate photodetection of a change in the deflection. This has led to the exploration of new detection methods which can not only measure deflection in nanoscale cantilevers, but can also be incorporated with MEMS and NEMS.

Optical method

The most commonly implemented detection scheme in modern AFM for measuring cantilever deflections are optical beam deflection and optical interferometry [45, 46]. The laser beam is focused near the free end of the cantilever which reflects it onto a split photo diode or position - sensitive detector (Fig. 2.2). The reflected light moves on the photodetector surface corresponding to the bending of cantilever. Two pieces of the detector are measured in opposition, giving a null signal when the beam is centered, and a large signal as the beam moves away from the center position. Using this signal, cantilever displacements up to 10^{-14} m can be measured. This detection scheme is very beneficial due to its linear response, simplicity, reliability, and need of no electric connections to the cantilever.

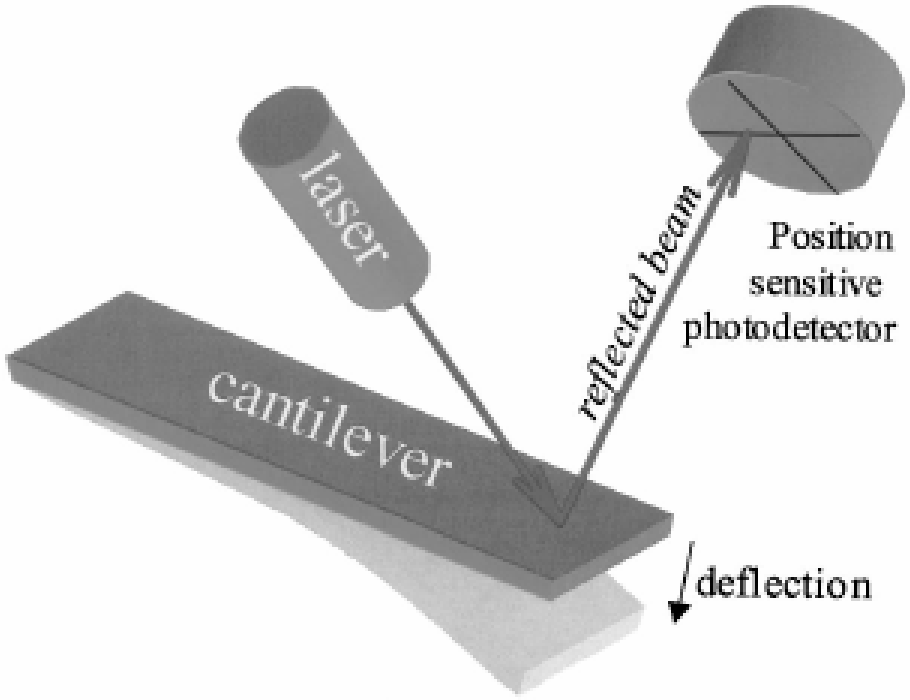

Figure 2.2: The optical detection scheme commonly used to measure deflections of microfabricated cantilever probes in AFM [7].

Visual detection

"Visual" detection is typically used for detecting the resonance in micro and nanocantilevers including nanofabricated silicon cantilevers as well as cantilevered nanotubes, nanowires, and nanobelts (Fig. 2.3). The various visual detection tools such as transmission electron microscope [47], scanning electron microscope [48], field emission microscope [49], or an optical microscope [50] can be used to measure electrically induced mechanical oscillations in such cantilevers. However, the requirement of

portable sensing device for the measurements of environmental changes, such as pressure, temperature, or presence of impurities limits its application.

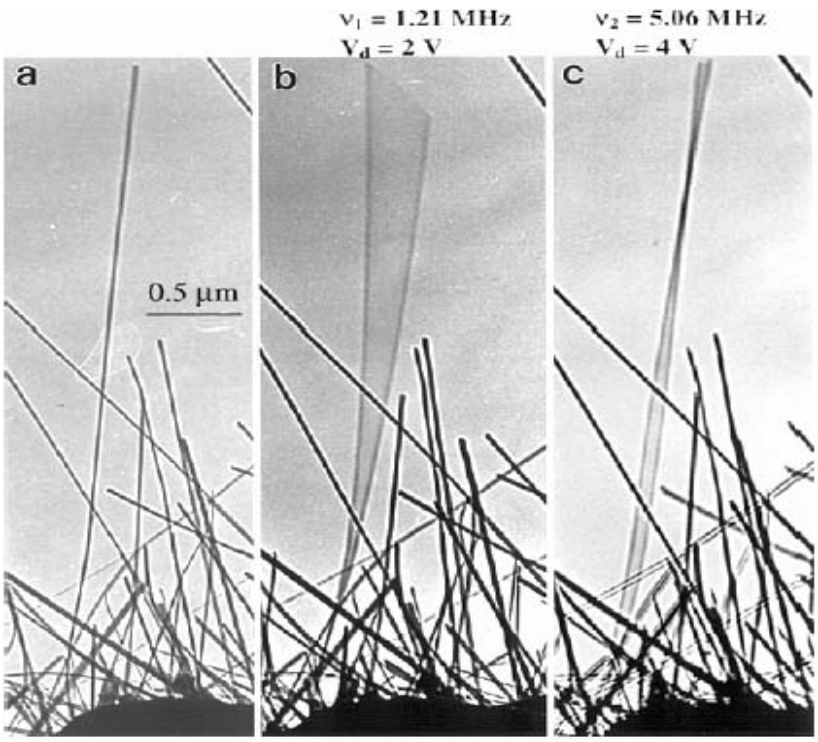

Figure 2.3: Measuring resonance of individual carbon nanotubes by in situ TEM [51]. A carbon nanotube which is (a) initially at its equilibrium position is electrically actuated to resonate at its (b) first mode frequency (f_1 = 1.21 MHz) and (c) at the second mode frequency (f_2 = 5.06 MHz).

Electrical Detection

The commonly used electrical detection techniques are the piezoresistance, piezoelectric and capacitance detection [7].

1) Piezoresistance method: It is a phenomenon which results in a change in the crystal's electrical conductivity when the crystal is stressed. This method can be readily implemented to monitor the stress induced in a cantilever, and therefore its deflection from its equilibrium position. Stress sensors can be integrated on a chip containing a cantilever and a Wheatstone bridge to measure the resisitivity. When a doped silicon cantilever [52, 53] is deformed, it leads to a change in its resistance. Piezoresistive cantilevers are designed with two identical legs in order to measure the resistance by making electric connections to the two legs (Fig. 2.4 (a)). It is advantageous as compared to the standard optical techniques as it involves no bulky and expensive optical components. In addition it has ease of integrating it on the same chip using CMOs technology without dealing with the tedious optical alignment. The main problem of this technique is the current flow through the cantilever resulting in heating up of cantilever and subsequent thermal shifts. It is ineffective in conducting liquids. The cantilevers must have a double structure, which gets difficult to form on the nanoscale.

2) Piezoelectric method: The deposition of piezoelectric material, such as ZnO (Fig. 2.14 (b)), is necessary on the cantilever for this technique. During this effect, the deformation of the cantilever induces the transient charges in the piezoelectric layer [54, 55]. One of the drawbacks of this technique is the thickness of the piezoelectric layer is required to be well above the optimal one in order to obtain large output.

The main disadvantage limiting the application of both piezoelectric and piezoresistive methods in MEMS sensors is the need of electric connections to the cantilever.

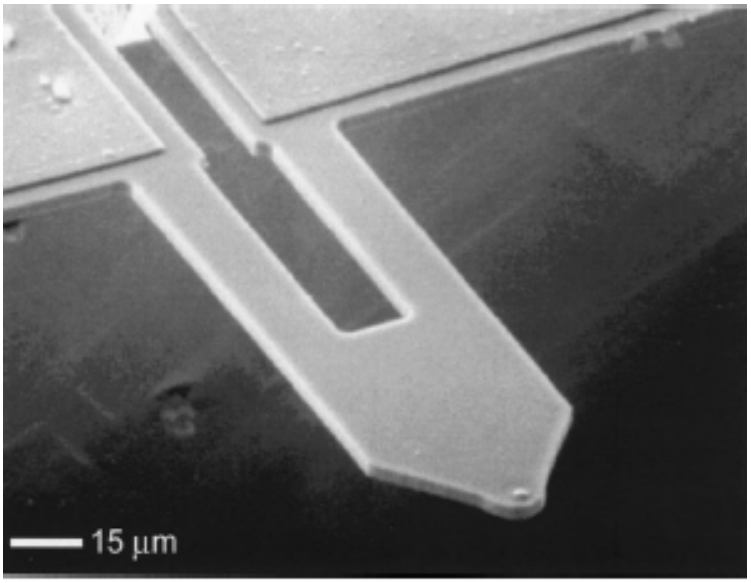

(a)

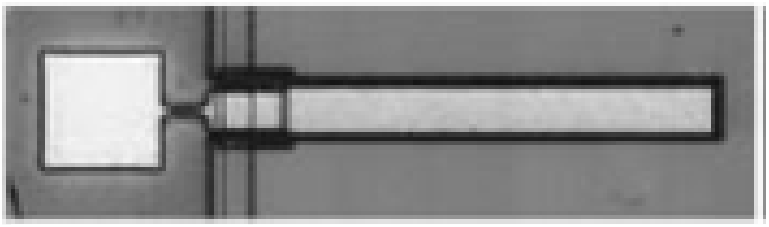

(b)

Figure 2.4 (a): Piezoresistive cantilever which can be used for AFM as well as MEMS senors [7], (b): Optical image of a piezoelectric (ZnO) multimorph [55].

Capacitance method

The most promising capacitance readout method is based on measuring the capacitance between two parallel conductor plates, where one is the cantilever and the other is the fixed conductor on the substrate separated by a small gap [56]. The fixed conductor is driven by applying an ac voltage with a dc offset and its frequency is swept till it matches with the resonant frequency of the cantilever.

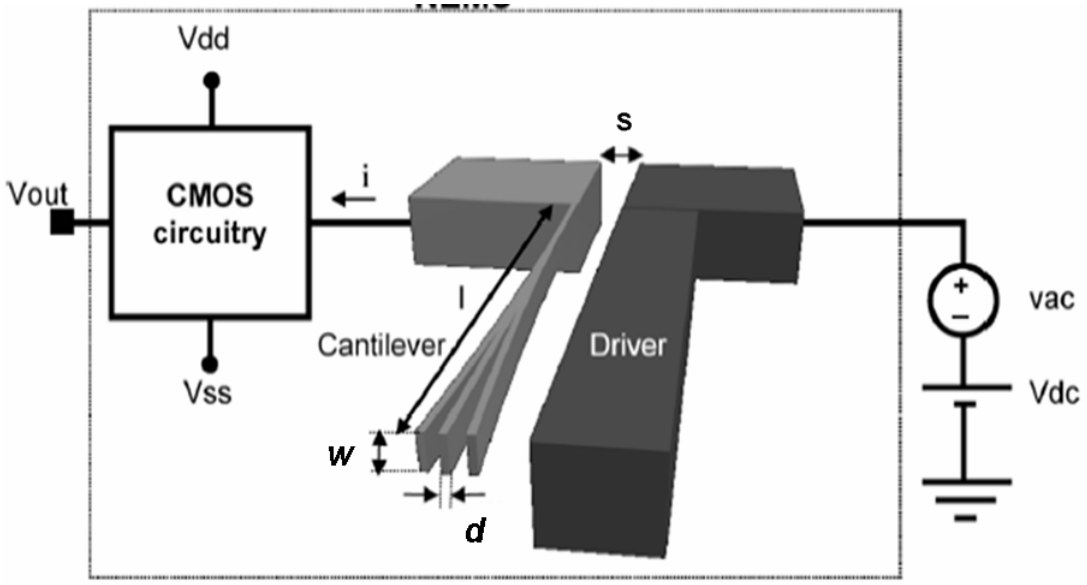

Figure 2.5: Capacitive readout technique commonly used for electrically excited cantilevers[57].

Since, the capacitance is inversely proportional to the gap distance (s), the sensitivity of this technique depends upon very small gap distance between the cantilever

and the substrate. The deformation of the cantilever causes the gap distance to change which in turn changes the capacitance between the two conductor plates. The main advantage of this method is that it can be easily integrated into MEMS and NEMS devices which are fully compliant with standard CMOS technology (Fig. 2.5). This work is mostly limited to the detection of the dynamic capacitance between a cantilever and its counter electrode. When the cantilever is in resonance the change in the capacitance of the system creates a dynamic signal given as [58]:

$$I(t) = \frac{d(CV)}{dt} = C(t)\frac{dV(t)}{dt} + V(t)\frac{dC(t)}{dx(t)}\frac{dx(t)}{dt} \tag{2.1}$$

where x is the deflection of the cantilever perpendicular to its surface. The first term in equation (2.1) corresponds to a signal created by the ac voltage applied to the static capacitance, whereas the oscillation of the cantilever contributes the second term. Experimentally, the first term in equation (2.1) is generally larger than a signal strictly arising from the static capacitance between the cantilever and the counter electrode. This can be attributed to the overall electrical pickup in the system and the large electric field created between the contacts compared to the cantilever. All these signals added to the first term in equation (2.1) contribute towards parasitic capacitances. Hence this method has limitations owing to the signal coming from the parasitic capacitances being much larger than the desired signal coming from the dynamic capacitance. Many research groups are actively investigating a way to design the geometry in order to minimize the parasitic capacitance using intricate micro and nano- fabrication schemes incorporated with CMOS on-chip circuitry [57, 58]. However, very little or no desired results have

obtained yet from these efforts. In spite of the parasitic capacitance, capacitive detection still remains the most suitable detection scheme for electrically excited cantilevers [59].

Theory of cantilever beams

Determination of Young's modulus of a silicon microcantilever

The Euler-Bernoulli Model of Beams and Cantilevers is used to determine Young's modulus of silicon microcantilever [60].

Assumptions:

1) A homogeneous, straight and an untwisted beam with a constant cross section (Fig. 2.6).

2) The beam thickness (d) and width (w) small compared to its length (L) reducing the system to a one-dimensional problem along the length of the beam.

3) The normal stresses (σ_x and σ_y) in the lateral directions are considered negligible.

4) A deflection in this model smaller than the radius of gyration (K). If the maximum deflection approaches K, additional non-linear terms must be considered.

Based on all these assumptions, the only remaining normal stress σ_z can be written as:

$$\sigma_z = kx \tag{2.2}$$

where k is a constant and $x = 0$ lies in the center of the beam. The total internal force has to be zero, and is given by:

$$F_{\text{int}} = \int_A \sigma_z dA = 0 \tag{2.3}$$

The total bending moment is equal to the moment due to internal forces considering no external momentum applied, which from equation (2.2) are only non-vanishing in the y direction:

$$M = M_y = \int_A x\sigma_z dA = k\int_A x^2 dA \tag{2.4}$$

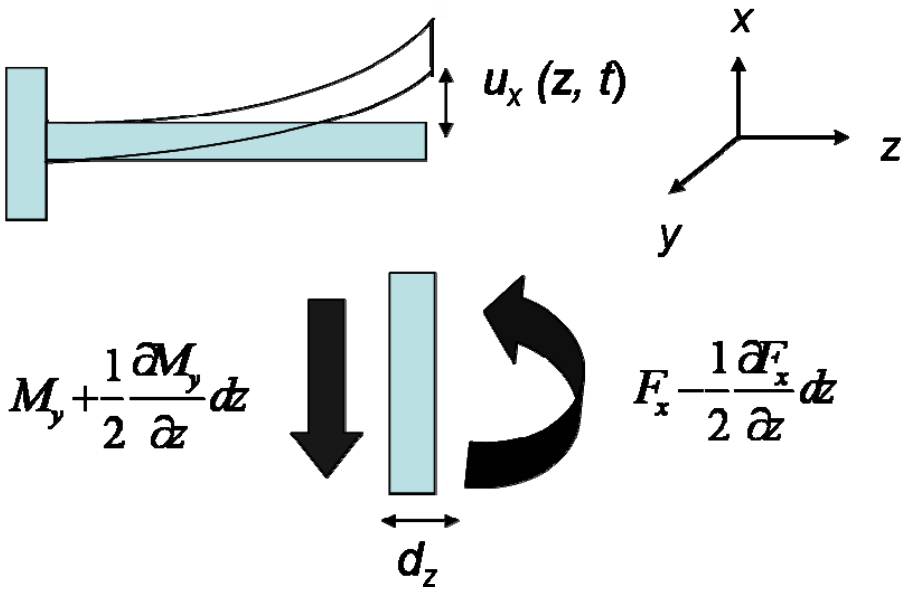

Figure 2.6: Flexural behavior of a straight beam and its stress distribution [60].

Defining the moment of inertia as:

$$I_y = \int_A x^2 dA \tag{2.5}$$

From equations (2.4)-(2.5):

$$k = \frac{M_y}{I_y} \tag{2.6}$$

and the cross sectional stress is given by:

$$\sigma_z = \frac{M_y x}{I_y} \tag{2.7}$$

Using Hook's law, the strain is given by:

$$\varepsilon_z = \frac{\sigma_z}{E} = \frac{M_y x}{E I_y} \tag{2.8}$$

where E is Young's modulus.

If $u_x(z,t)$ is the displacement of the beam in x direction and the deflection is small, $(du_x / dx \ll 1)$, then the second derivative of the deflection which is approximately the inverse of the radius of curvature r is given as:

$$\frac{\partial^2 u_x(z,t)}{\partial z^2} \approx \frac{1}{r} \tag{2.9}$$

The strain can be calculated as:

$$\varepsilon = \frac{dl - dl_0}{dl_0} = \frac{(r-x)d\theta - rd\theta}{r \sin d\theta} = \frac{-x}{r} \tag{2.10}$$

The Euler-Bernoulli law of elementary beam theory can be obtained by combining equations (2.8) and (2.10),

$$M_y = -EI_y \frac{\partial^2 u_x(z,t)}{\partial z^2} \tag{2.11}$$

In the absence of external forces or bending moments, the equation of motion becomes:

$$m \frac{\partial^2 u_x(z,t)}{\partial t^2} = \sum F_{\text{int}} \tag{2.12}$$

and as the total moment has to be zero,

$$\sum M_{\text{int}} = 0 \tag{2.13}$$

The relationship between the bending moment and the force:

$$F_x = -\frac{\partial M_y}{\partial z} \tag{2.14}$$

The mass of the beam can be given as,

$$m = \rho A d_z \tag{2.15}$$

where ρ is the density of the beam, A is its cross sectional area and d_z is its dimension along the z- direction. Using equation (2.15), we can write the equation of motion (2.12) as,

$$\rho A \frac{\partial^2 u_x(z,t)}{\partial t^2} = -\frac{\partial^2 M_y}{\partial Z^2} \tag{2.16}$$

After substituting equation (2.11) we get the final equation of motion:

$$\rho A \frac{\partial^2 u_x(z,t)}{\partial t^2} + EI_y \frac{\partial^4 u_x(z,t)}{\partial z^4} = 0 \tag{2.17}$$

Using

$$\alpha = \sqrt[4]{\frac{\rho A}{EI_y}} \tag{2.18}$$

and solving equation of motion (2.17) we get,

$$U_x(z,\omega) = B_1 \sin(\alpha z\sqrt{\omega}) + B_2 \cos(\alpha z\sqrt{\omega}) + B_3 \sinh(\alpha z\sqrt{\omega}) + B_4 \cosh(\alpha z\sqrt{\omega}) \tag{2.19}$$

For a clamped-free cantilever, the boundary conditions at the clamped end are:

$$U_x(0,\omega) = 0 \quad \frac{dU_x}{dz}(0,\omega) = 0 \tag{2.20}$$

and at the free end ($z = L$) with no bending moments or shear forces acting on the beam are:

$$\frac{d^2U_x(L,\omega)}{dz^2} = 0 \qquad \frac{dU^3{}_x(L,\omega)}{dz^3} = 0 \tag{2.21}$$

The first boundary conditions forces $B_2 = B_4$ and $B_1 = -B_3$, whereas applying the last conditions the solution reduces to:

$$\frac{2 + 2\cos(\alpha L\sqrt{\omega})\cosh(\alpha L\sqrt{\omega})}{\sin(\alpha L\sqrt{\omega}) - \sinh(\alpha L\sqrt{\omega})} = 0 \tag{2.22}$$

There is no analytical solution but can be solved numerically using the substitution:

$$\beta = \alpha L\sqrt{\omega} \tag{2.23}$$

The natural resonant angular frequencies can be calculated as,

$$\omega_i = \frac{\beta_i^2}{L^2}\sqrt{\frac{EI_y}{\rho A}} \tag{2.24}$$

The moment of inertia of a beam with circular cross section is given by:

$$I_y = \frac{\pi D^4}{64} \tag{2.25}$$

where D is the diameter of the beam and the inertia for rectangular cross section is:

$$I_y = \frac{wd^3}{12} \tag{2.26}$$

where w is the width and d is the thickness of the beam respectively. The final solution is the same for the clamped - clamped and free- free beam with the only difference from the cantilever in the factor β_i, given in the Table 2.1.

	β_i^2	β_i^2
i	Clamped –free cantilever	Clamped-clamped beam
1	3.516	22.373
2	22.034	61.678
3	61.701	120.903
4	120.912	199.860
5	199.855	298.526

Table 2.1: Solution of the equation of motion for a cantilever beam.

I now calculate the Young's modulus (E) from resonance frequency f_0 of a clamped –free (diving board) silicon microcantilever, oscillating perpendicular to the plane of largest area of the cantilever using equation (2.24),

$$E = \frac{\rho A(\omega_i)^2 L^4}{(\beta_i^2)^2 I_y} \tag{2.27}$$

Note the E in an elastically anisotropic material is equal to $1/s_{ii}$, where s_{ii} is a component of the compliance tensor and the i direction is parallel to the long edge of the cantilever. The cantilevers we use are lightly doped single crystal silicon, with the edges along the <110> direction.

Microcantilever Dimensions according to manufacturer (Mikromasch):

Length: $L = 350$ [μm]

Width: $w = 35$ [μm]

Thickness: $d = 2$ [μm]

Area: $A = wd$

Material Properties of Cantilever:

Density: $\rho = 2330$ [kg/m^3]

Resonant Frequency: $f_0 = 17.74$ [kHz]

The resonant frequency (f_0) of the Si microcantilever reported above is measured using the Harmonic Detection of Resonance (HDR) technique (discussed in chapter 3). Hence, using equations (2.26) and (2.27) with $\omega_0 = 2\pi f_0$ we get,

$$E_{Si} = \frac{12\rho(2\pi f_0)^2 L^4}{(\beta_i^2)^2 d^2}$$

$$E_{Si} = \frac{12(2330)(2\times\pi\times 17,740)^2(350\times10^{-6})^4}{(3.516)^2(2\times10^{-6})^2}\frac{kg}{s^2 m} = 105.5GPa$$

From *Nye*[61], for a cubic material,

$$\frac{1}{E} = s_{11} - 2\left(s_{11} - s_{12} - \frac{1}{2}s_{44}\right)\left(l_1^2 l_2^2 + l_1^2 l_3^2 + l_2^2 l_3^2\right)$$

where the *l*'s are the direction cosines of the direction in which *E* is measured.with respect to crystal axes Mikromasch states that *L* is along the <110> direction, for which $l_1 = l_2 = \frac{1}{\sqrt{2}}, l_3 = 0$. From *Landolt-Bornstein* (1978), $s_{11} = 7.74 \times 10^{-12} Pa^{-1}$, $s_{12} = -2.16 \times 10^{-12} Pa^{-1}, s_{44} = 12.6 \times 10^{-12} Pa^{-1}$. Thus

$$\frac{1}{E} = \left[7.74 - 2(7.74 + 2.16 - 6.3)\left(\left(\frac{1}{\sqrt{2}} \right)^2 \left(\frac{1}{\sqrt{2}} \right)^2 + 0 + 0 \right) \right] \times 10^{-12} Pa^{-1} = 5.94 \times 10^{-12} Pa^{-1}$$

or E_{110} = 168 GPa. (The manufacturer gives E_{110} = 169 GPa). Mikromasch states the resonance frequency as 17-24 kHz, presumably because of variation in the dimensions, and our measurement is within these tolerances. We did not measure the dimensions of cantilevers ourselves.

CHAPTER THREE

USING ELECTRIC ACTUATION AND DETECTION OF OSCILLATIONS IN MICROCANTILEVERS FOR PRESSURE MEASUREMENTS

Introduction

Cantilever structures are the simplest structures that can be easily micro-machined, mass produced and integrated into (MEMS/NEMS) [60]. The microcantilever's response depends on any variable that changes the vibration of the cantilever, and is measured as a change in the resonance frequency, amplitude, phase and/or quality factor. These response characteristics of a microcantilever can serve as a measure of a change in absolute pressure in the range of 10^{-4} to 10^{3} torr. The major difficulty in making these measurements is mostly the ancillary equipment such as lasers or high magnetic fields that must be used. For these measurements it is advantageous if the resonating system is portable and therefore a capacitive readout of the mechanical vibration is ideal. In addition, the static capacitance between the microcantilever and a counter electrode as well as the parasitic capacitance of the rest of the circuitry overwhelm the signal making it difficult to detect the mechanical oscillations. The various techniques currently available to overcome this difficulty mainly involve (i) single electron transistors [62], which often operate at low temperatures, and (ii) sensing elements such as comb drives along with on-chip circuitry [57, 63] which involve intricate multi-element designs increasing the cost of production and probability to breakdown. To this end, it would be very convenient to have the resonance of the microcantilever actuated and detected electrostatically.

Harmonic Detection of Resonance

Recently, we have developed an electrical readout system using a technique called the harmonic detection of resonance (HDR) [1, 2, 64]. In this technique, the microcantilever is forced into resonance by electrostatic actuation applying an ac voltage (V_{ac}) with a dc offset (V_{dc}) to the counter electrode which is a tungsten (W) tip. The W wire was etched in NaOH to form a sharp conical W tip [65]. The cantilever is aligned near the counter electrode over the dark field microscope such that the long axis of the cantilever intersects the axis of the conical tip, and the plane of the cantilever is parallel to the nearby surface of the conical tip (see inset in Fig. 3.1). The electrical signal due to the modulated charge created on the cantilever by the dynamic capacitance as well as the electrostatic driving signal is measured by an A250 charge sensitive preamplifier. It is also possible to measure the fA current going to and from the cantilever directly. The charge induced on the cantilever is a function of the forcing voltages and the position of the cantilever. This charge on a microcantilever has a rich harmonic structure and measuring it at higher harmonics away from the driving frequency avoids the parasitic capacitance problem. The lock-in amplifier detects the output of the A250 at the higher harmonics of the frequency of the forcing ac voltage, which in turn is referenced to the signal generator (Fig. 3.1). We have shown that this enables easy determination of the resonance frequency of individual microcantilevers with a substantial signal to background ratio. Using HDR, we have measured mechanical resonances (f_0) in silicon microcantilevers at 2^{nd}, 3^{rd} 4^{th} , 5^{th} and 6^{th} harmonics [2]. This technique offers unique

benefits for devices, such as highly portable design, reduction in background signal, low power consumption, and fast response.

In general, we are only concerned with the first mode of vibration. This is because of the greatest tip deflection in the 1st mode facilitating measurement. Also, the amplitudes of the higher modes are small at the driving frequencies used, in part because the coupling to the electrostatic field is weaker for higher modes. Finally, the lock-in amplifier used has a limited frequency range; making it difficult to measure the harmonics of higher modes. Each mode of vibration has a particular natural frequency (f_0) and damping ratio. Note the distinction between modes and harmonics. The term "harmonic", which is *defined* as an integer multiple of some fundamental frequency is very often confused with the modes of vibration. The confusion arises because for doubly clamped structures, e.g. violin strings, the frequencies of higher modes of vibration are all integer multiples of the first mode frequency, just as for harmonics. Thus for doubly clamped systems, harmonic and modal frequencies are essentially interchangeable. However, for cantilevers the frequencies of the higher modes are *not* integer multiples of the first, and thus harmonic and modal frequencies are not equivalent.

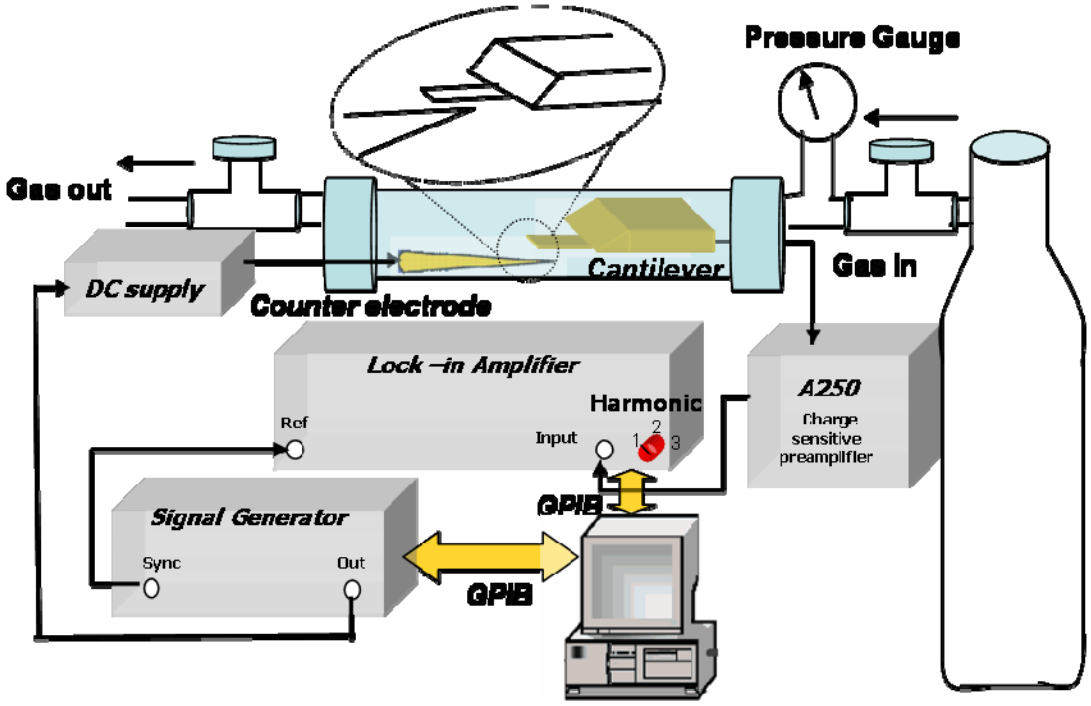

Figure 3.1: A schematic of the experimental set up using our harmonic detection of resonance method for sensing pressure changes. The inset shows the geometry of the cantilever with respect to that of the W tip.

Silicon microcantilevers have been extensively studied as sensors for pressure, temperature, mass and viscosity measurements [14, 66-71]. The ongoing research in this area mainly focuses on the resonance response as a function of pressure in different regimes - the intrinsic regime, the molecular flow regime, the viscous regime, and transition regimes in between. In the intrinsic regime (10^{-8} torr - 10^{-6} torr) due to the low air pressure, air damping is insignificant compared to the intrinsic damping of the vibrating cantilever itself. Hence the resonant frequency f_0 and the quality factor Q are

nearly independent of air pressure p. The collisions of air molecules with the vibrating cantilever cause the damping in case of the molecular region (10^{-6} torr – 10^{-1} torr). For the viscous region ($p > 10^{-1}$ torr), the velocity of the cantilever is always much smaller than the speed of sound in the medium and hence we can consider air as a viscous fluid. However, there can be turbulence, in which case the damping is roughly proportional to the square of velocity [72]. In the molecular region, the dependence of Q on p can be explained by the Christian model [73], which emphasizes that the Q is proportional to $1/p$. Blom *et al.* mainly focuses on dividing the viscous regime into two zones, one with Q independent of p and the other with Q proportional to $1/\sqrt{p}$ [71]. In this chapter, we report the nonlinear dynamics of microcantilevers under different gases with varying pressures at higher harmonics using HDR [2]. The use of different harmonics can enable us to adjust the range of pressures over which the sensor has an efficacious response, enhancing its sensitivity to a particular environment.

The main focus of this investigation is to conduct a characteristic study of a resonating cantilever as a function of chamber pressure over six decades (10^{-3} torr – 760 torr) using the HDR technique described briefly in the previous paragraph [2]. The effects of different gases: He, Ar, H_2, and air are measured and are compared with theoretical results. We performed a separate study to compare the 2nd and 3rd harmonic responses of a silicon microcantilever as a function of p.

Quality factor (Q)

For a harmonic oscillator, the usual definition of the quality factor Q is

$$Q = \frac{2\pi U_i}{U_d} = \frac{2\pi \text{ (stored vibration energy)}}{\text{energy dissipated per period}}$$

It is usually measured at the 1st harmonic of the power curve near resonance in a linear system, that is, a simple harmonic oscillator (SHO). In case of our HDR technique, we do not have a simple harmonic oscillator, nor is it easy to measure the first harmonic response, as it is usually overwhelmed by parasitic capacitance signals. For an SHO, Q is also equal to the resonant frequency (f_0) divided by the full width at half maximum of the resonance peak of a power vs. frequency plot. We will use the following definition of the experimental quality factor Q_E for any harmonic and for cantilever motions that are nearly that of a SHO as well as the motions in which the position of the cantilever affect the spring constant and driving force.

$$Q_E = \frac{f_0}{FWHM} \tag{3.1}$$

where *FWHM* is the full width at half maximum of the resonant peak of a squared amplitude vs. frequency plot, *for any harmonic*. Although this is not the standard Q, it is generally consistent with results predicted for a standard Q as discussed next.

Effect of damping on Q_E

The equation of motion for a real system governed by the damping, a time dependent force (F_0) is given as,

$$m\frac{\partial^2 x(t)}{\partial t^2}+b\frac{\partial x(t)}{\partial t}+kx(t)=F_0\cos(\omega t)$$

where m is effective mass of the 1st mode of vibration of the cantilever, b is damping parameter, k is spring constant , x is the displacement of the cantilever. Further, following Pippard [74] for a damped SHO, the quality factor is identical to Q_E defined above and given as,

$$Q_E=\frac{1}{2}\frac{\omega'}{\omega''},$$

where $\omega''=\frac{b}{2m}$ and $\omega'=\sqrt{\omega_0^2-2\left(\frac{b}{2m}\right)^2}=\sqrt{\left(\frac{k}{m}\right)-2\left(\frac{b}{2m}\right)^2}$,

Since we can determine ω_0 and Q_E, we should be able to calculate the damping, b. Note that we will have to plot the *square* of the amplitude vs. frequency to get Q_E. Thus

$$Q_E=\frac{1}{2}\frac{\omega'}{\omega''}=\frac{1}{2}\frac{\sqrt{\omega_0^2-2\left(\frac{b}{2m}\right)^2}}{\frac{b}{2m}}$$

$$Q_E{}^2=\frac{\omega_0^2-2\left(\frac{b}{2m}\right)^2}{4\left(\frac{b}{2m}\right)^2}$$

$$4Q_E{}^2\left(\frac{b}{2m}\right)^2=\omega_0^2-2\left(\frac{b}{2m}\right)^2$$

$$\left(\frac{b}{2m}\right)^2=\frac{\omega_0^2}{4Q_E{}^2+2}$$

Since in our case $Q_E >> 50$, we can neglect the 2 in the denominator on the right side, and get the damping b as,

$$b \approx m\frac{\omega_0}{Q_E} \tag{3.2}$$

Since we can directly determine angular resonant frequency (ω_0) and Q_E, and estimate m reasonably well, we can estimate the damping, b, with the caveat that our systems are not linear and we use harmonics other than the first.

Pressure dependence of the quality factor

The viscous region: For the viscous region, Hosaka *et al.* gave a direct evaluation of the quality factor [75]

$$Q_p = \frac{2\rho_b d w^2 \omega_0}{6\pi\mu w + (3/2)\pi w^2\sqrt{2\mu(M/RT)\omega_0 p}} \tag{3.3}$$

where d is the thickness, w the width of the cantilever, μ the dynamic viscosity, M the molecular mass of the gas molecules and ρ_b the density of the cantilever beam R, T and p are the gas constant, the absolute temperature and pressure respectively.

As emphasized by Blom *et al*. we can see from equation (3.3) the first (low pressure) part of the viscous region is almost independent of pressure however when the pressure increases, the quality factor prominently shows $1/\sqrt{p}$ dependence.

The molecular region: In the molecular regime the quality factor can be written as [66],

$$Q_p = \frac{\rho_b d \omega_0}{4} \sqrt{\frac{\pi}{2}} \sqrt{\frac{RT}{M}} \frac{1}{p} \tag{3.4}$$

which clearly indicates its $1/p$ dependence taking into account the collisions between the gas molecules and the vibrating cantilever. The total quality factor (Q_E) of the system can be given as

$$\frac{1}{Q_E} = \frac{1}{Q_p} + \frac{1}{Q_{Si}} \tag{3.5}$$

where Q_p is the pressure dependent quality factor and Q_{Si} is the pressure independent intrinsic quality factor. Simplifying equation (3.5) the experimental quality factor in the molecular regime can be written as,

$$\frac{1}{Q_E} = C_1 p + C_2 \tag{3.6}$$

where C_1 is the slope of a plot of $1/Q_E$ vs. p and C_2 is one over the intrinsic quality factor of the cantilever (Q_{Si}). The parameter (C_2) can be used as a measure of the thermal and defect properties of materials.

Resonant frequency and spring softening

Taking into account the softening of the effective spring constant of the system from k to k' [60], the resonant angular frequency of the cantilever driven into resonance using HDR is given by [76],

$$\omega_0' = \sqrt{\frac{k'}{m}} \tag{3.7}$$

with

$$k' = k - \frac{dF_c}{dx} \tag{3.8}$$

where

$$\frac{dF_C}{dx} = -½\left[\frac{d^2C}{dx^2}\right]_{x=0} \{V_{dc}{}^2 + 2V_{dc}V_{ac}\cos(\omega t) + \frac{1}{2}V_{ac}^2[1+\cos(2\omega t)]\} \tag{3.9}$$

where the force (F_c) is proportional to the derivative of the capacitance (C) as a function of the position x of the cantilever.

Experimental Setup

The microcantilevers used in this pressure study are gold-coated silicon tipless microcantilevers from Micromasch, typically 35 μm wide, 2 μm thick and 350 μm long. The microcantilever and a sharpened tungsten tip (acting as a counter electrode) are glued down on the chip carrier in a parallel geometry with ~10 μm gap distance. We used HDR to measure the response of a silicon micro-cantilever (f_0 = ~17 - 21 kHz) mounted on a chip carrier [1, 2, 64]. The experimental setup consists of an A250 charge amplifier, a signal generator, a dc power supply, and a lock-in amplifier as explained before in Fig. 3.1. This chip carrier was then plugged into a board mounted inside a glass chamber which was subjected to changes in pressure and environments. The various experiments carried out on these microcantilevers can be divided into three groups:

(i) Study the effect of pressure on the response of a vibrating cantilever as a function of environment. Using a pump station, the chamber pressure was varied from 10^{-3} torr to ambient pressure (760 torr) under different environments such as air and He. The low pressures (< 10^{-3} torr) are measured using a hot cathode gauge, and (KJLC BDG Series) Bourdon dial gauges are used around ambient pressure. The thermocouple pressure gauge is used for in-between pressures.

(ii) Study the impact of molecular mass on a different cantilever's vibration by back filling the glass chamber (cf. Fig. 3.1) at 760 torr with H_2, He, air and Ar.

(iii) A separate cantilever of the same size was used to study the cantilever's vibration at the 2nd and 3rd harmonics under different chamber pressures in He. We are working with the gases for which we expect negligible physical or chemical absorption or effects due to their dielectric constant. Further, all the measurements are carried out at room temperature and the damping of the vibrating cantilever can be attributed to the internal friction in the cantilever (intrinsic damping), the friction at the support and the surrounding gas.

Results and Discussion

(I) Response to pressure

We started with a new and clean microcantilever having a $Q_E \sim 60$ in ambient air at atmospheric pressure with a gap distance of 8 μm. The water vapor present in the ambient air has been shown to have an insignificant effect on our results. The

microcantilever demonstrated very high Q_E ~ 10,000 at 10^{-3} torr, as shown in Fig. 3.2 which saturated at pressures below 10^{-3} torr (not shown). While studying a different cantilever at lower pressures, the effective spring constant decreased causing the resonant frequency to decrease as shown in Fig. 3.3(a) (equation (3.7)). This could be attributed to the greater amplitudes (and thus higher Q_E) at these pressures that lead to the cantilever spending more time close to the counter electrode thereby resulting in the spring softening (equation (3.8)). There may also be a shift in resonant frequency due to the change in damping. A similar trend was observed in the case of a He environment (Fig. 3.3(b)). The smaller atomic mass of He caused relatively lower damping, contributing to the larger amplitudes and the higher Q_E along with the decrease in the resonant frequency compared to air (Figs. 3.3(a) and 3.3(b)). At ambient pressure the damping parameter is 3.21×10^{-8} Nsm^{-1} under a He environment (calculated using equation (3.2)). $1/Q_E$ showed an approximately linear response (shown by the dotted line) to pressure in the molecular region as predicted by equation (3.6) in both air and He environments. The calculated value of constant C_2, corresponding to $1/Q_{Si,}$ is 1.35×10^{-4} in both air and He and thus is in good agreement with the values reported in the literature ($Q^{-1} = 3\times10^{-4}$ to 1.24×10^{-4}) (see Fig. 3.4) [60]. Similarly the slope of the $1/ Q_E$ vs. pressure plot (C_1) in the molecular region is 7×10^{-4} $torr^{-1}$ in He and the slope calculated using equation (3.4) is 1.43×10^{-4} $torr^{-1}$. Hence the experimental results are consistent with the theoretical model calculations, giving some justification for using our Q_E for the usual Q. We also compared Q_E and the normalized variation of resonant frequency (f_0) as a function of pressure with the results presented by Bianco *et al*. [66] (Figs. 3.5(a), 3.5(b)). Similar

trends are observed in both cases. It is the fractional change in resonant frequency or quality factor which determines the utility of the cantilever as a pressure gauge. In Fig. 3.5 (a) the log scales indicate the fractional changes in quality factor equally well for the two results. Our data followed their experimental values very well (although with some loss in sensitivity) in spite of the difference in the excitation and detection schemes of the microcantilever in the two studies (Fig. 3.5(a)). For Fig. 3.5(b) little change in f_0 is observed with pressure changes. Bianco *et al.* [66] have a larger fractional change in f_0 near atmospheric pressure. But in neither their work nor ours is there a sufficient change in f_0 to be useful as a gauge. In both techniques, the variation is small, but particularly so in the nonlinear HDR system. We get comparatively higher amplitudes at low pressures, as well as a decrease in f_0 [2]. A possible reason for this is that the nonlinearities in our system make higher amplitudes shift the apparent f_0 to lower frequencies, thus canceling the increase seen by Bianco *et al.* [2].

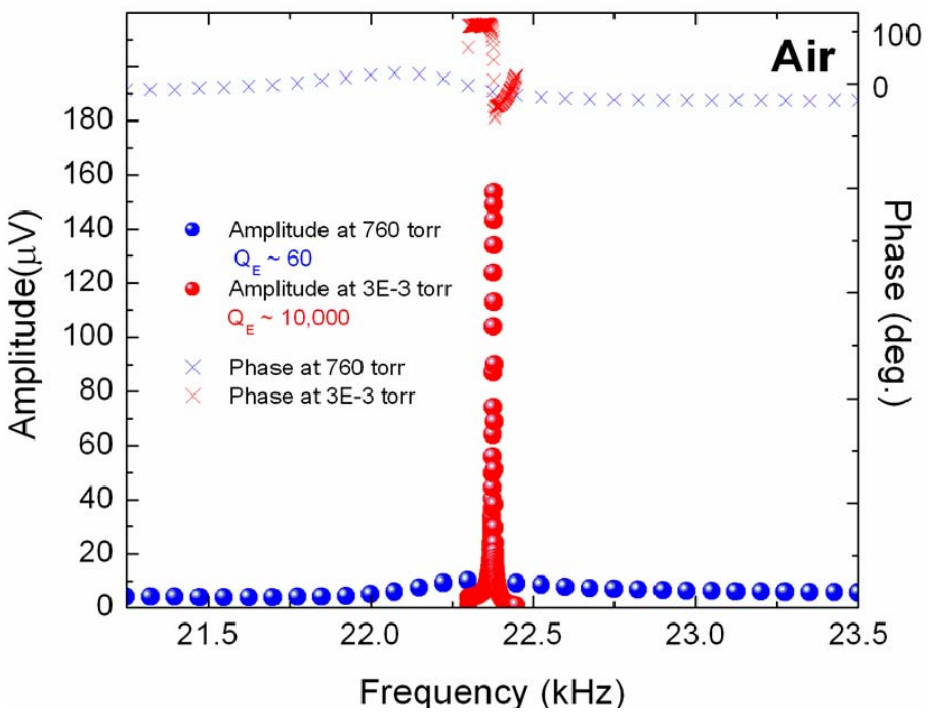

Figure 3.2: Amplitude (bullets) and phase (crosses) of the cantilever near the resonance frequency for 760 (blue) and 3E-3 torr (red) when measured at the 2nd harmonic (V_{dc} = 9 V, V_{ac} = 5 V) with 8 μm gap distance. The large change in the 2nd harmonic signal shows that the HDR technique is a viable method for pressure sensing.

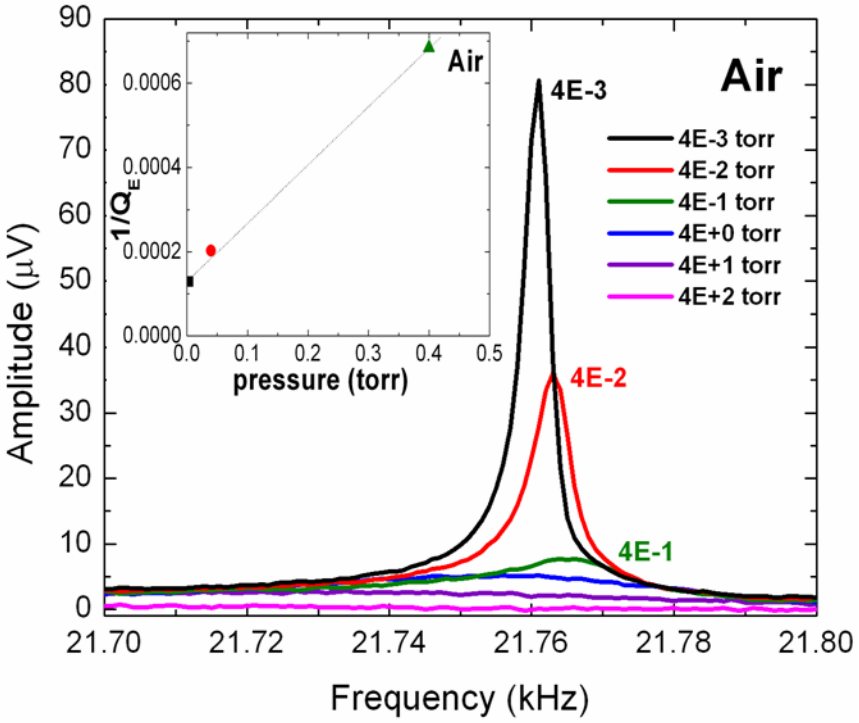

Figure 3.3 (a): Resonance spectra of the 2nd harmonic at different pressures in air. The voltages applied in the molecular regime were V_{dc} = 6.5 V, V_{ac} = 5 V and in the viscous regime were V_{dc} = 8 V, V_{ac} = 5 V. The dc voltages were adjusted in the two pressure regimes so that the microcantilever did not enter into the highly nonlinear region. The inset shows $1/Q_E$ as calculated using equation (3.3) as a function of the chamber pressure when $p > 10^{-1}$ torr and using equation (3.6) when $p < 10^{-1}$ torr.

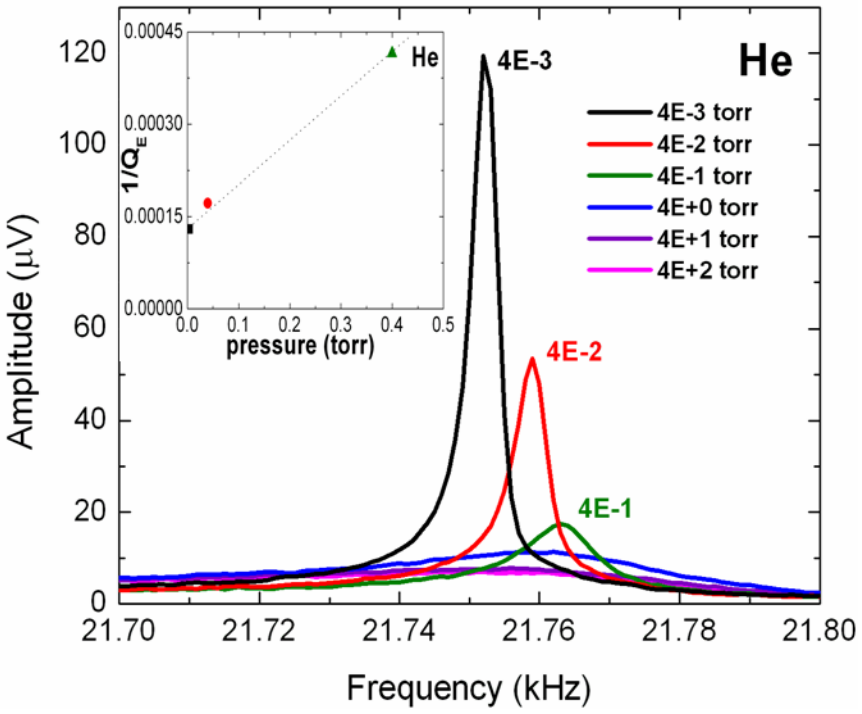

Figure 3.3 (b): Resonance spectra at the 2nd harmonic at different pressures in a helium environment. In the molecular region voltages applied were V_{dc} = 6.5 V, V_{ac} = 5 V and in viscous region were V_{dc} = 8 V, V_{ac} = 5 V. Note the higher sensitivity of the response in a lighter gas. The inset shows $1/Q_E$ as a function of the pressure in a He environment.

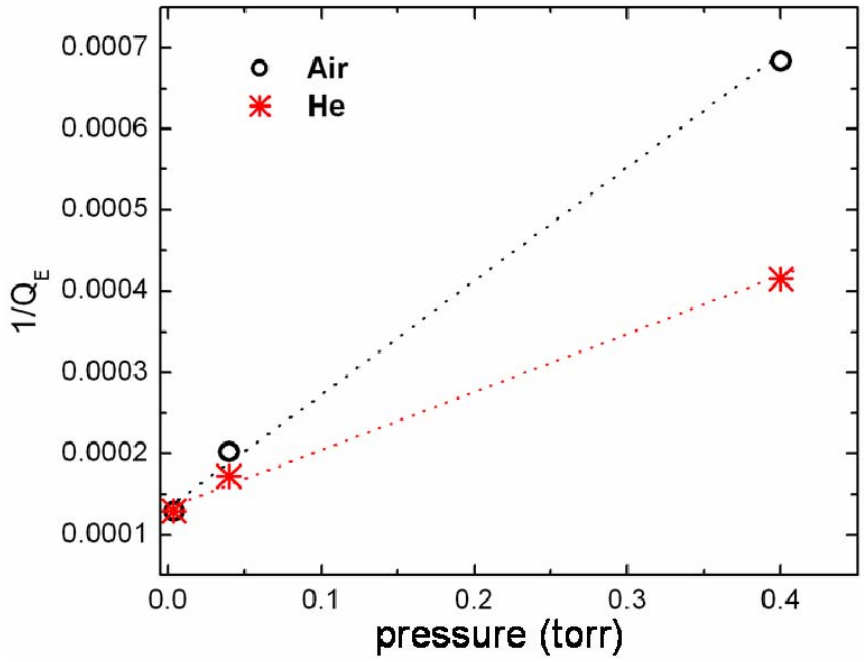

Figure 3.4: $1/Q_E$ as a function of pressure. As detailed in the text, the extrapolation to zero pressure gives the intrinsic damping of the silicon cantilever, which agrees with previous measurements. The slope of the above plot gives the value of the constant C_1 and the intercept gives the constant C_2 (= $1/Q_{Si}$) as discussed in equation (3.6). In the molecular region voltages applied were V_{dc} = 6.5 V, V_{ac} = 5 V and in viscous region were V_{dc} = 8 V, V_{ac} = 5 V.

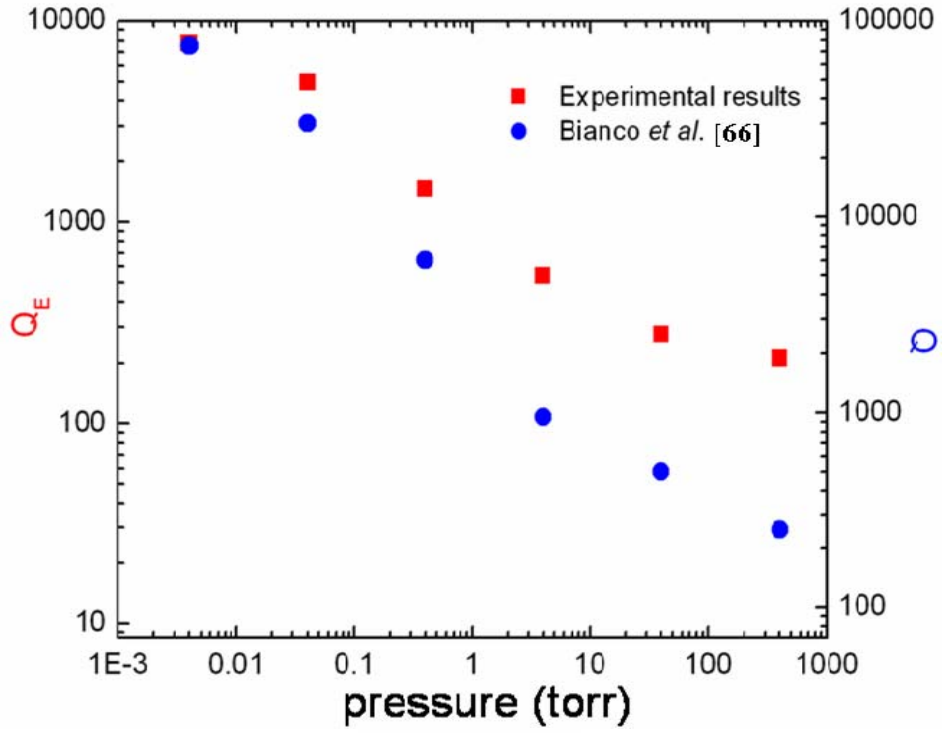

Figure 3.5 (a): Comparison of the experimental results (shown by red squares, left hand axis) for Q_E as a function of pressure using HDR (red squares) and Q as measured by Bianco *et al*. [66] (shown by blue circles, right hand axis) using piezoelectric excitation and optical detection. In the molecular region voltages applied were V_{dc} = 6.5 V, V_{ac} = 5 V and in viscous region were V_{dc} = 8 V, V_{ac} = 5 V.

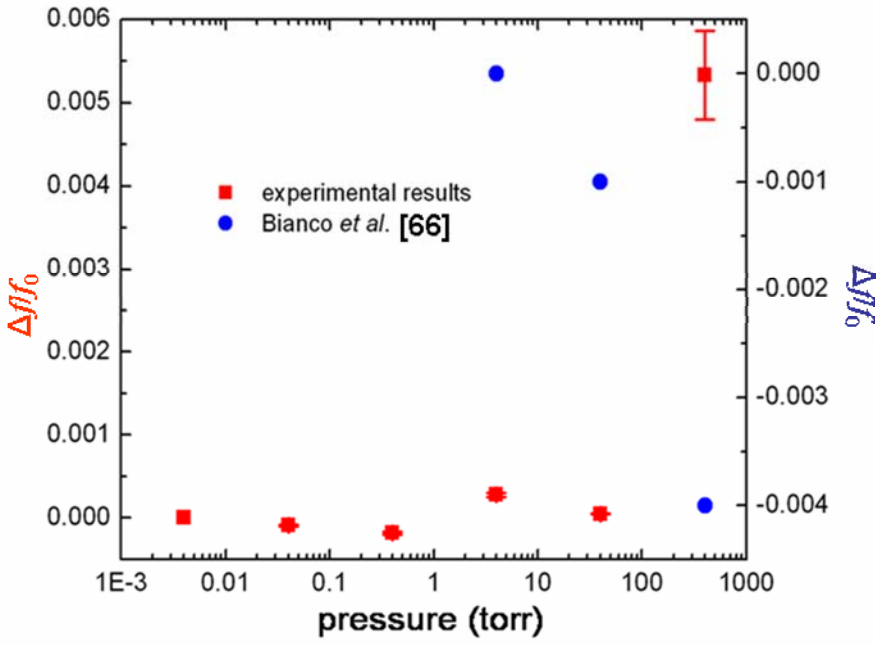

Figure 3.5 (b): Our experimental results (shown by red squares, left hand axis) for the normalized variation of resonant frequency as a function of pressure using HDR and the experimental data presented by Bianco *et al*. [66] (shown by blue circles, right hand axis) in the viscous region. In the molecular region voltages applied were V_{dc} = 6.5 V, V_{ac} = 5 V and in viscous region were V_{dc} = 8 V, V_{ac} = 5 V.

(II) Impact of the gas environment

Equations ((3.3) and (3.4)) show that Q is inversely proportional to the square root of the mass of the gas inside the chamber. It can be seen in Figs. 3.6(a) and 3.6(b) that the resonant frequency, amplitude, and thus the quality factor changed with the change in environment at ambient pressure (760 torr). A different silicon microcantilever

of the same dimensions at 12 μm gap distance showed greatly enhanced response with the change in the gas environment at the same pressure especially in a hydrogen atmosphere with a sharper resonant peak implying a better Q_E. In a H_2 environment the signal amplitude is about three times of that in air. As per the theoretical prediction, in the H_2 environment (M = 2, lightest), the amplitude and Q_E are the highest whereas the lowest amplitude and Q_E are found in the heaviest gas, Ar (M = 40) (Fig. 3.6(a)). The f_0 first increased with a decrease in the mass of the gas molecules from Ar to He, but for H_2 f_0 decreased. See Fig. 3.6(b). The decrease in resonant frequency as the mass of the gas atom decreased from He to H_2 may be due to a weakly observed Duffing behavior in the H_2 environment, in which the cantilever approached the counter-electrode more closely, due to the much larger amplitude, which, as mentioned above, would lead to a lowered effective spring constant. In any case, the differing results demonstrate the ability to differentiate between gases surrounding the cantilever. This can be advantageous as it would be possible to distinguish between different average molecular masses at constant pressure. On the other hand, its can be disadvantageous as like a thermocouple gauge, this would have to be calibrated for different gases to give the correct pressure.

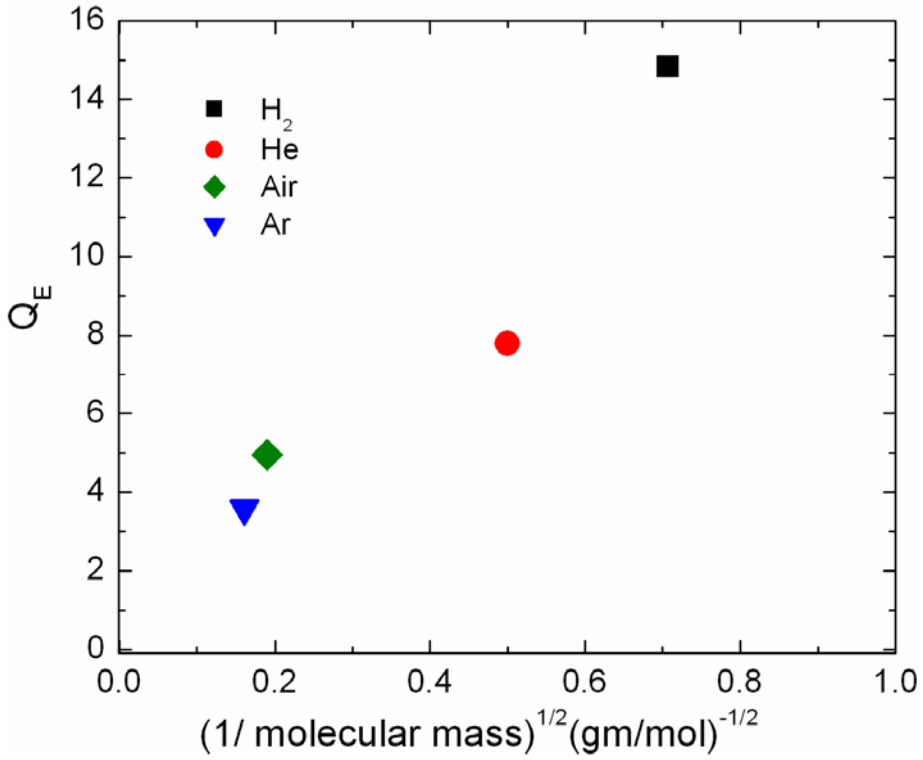

Figure 3.6 (a): Dependence of Q_E on the molecular mass of the surrounding gas measured at the 2nd harmonic at ambient pressure with V_{dc} = 9 V, V_{ac} = 10 V at 12 μm gap distance.

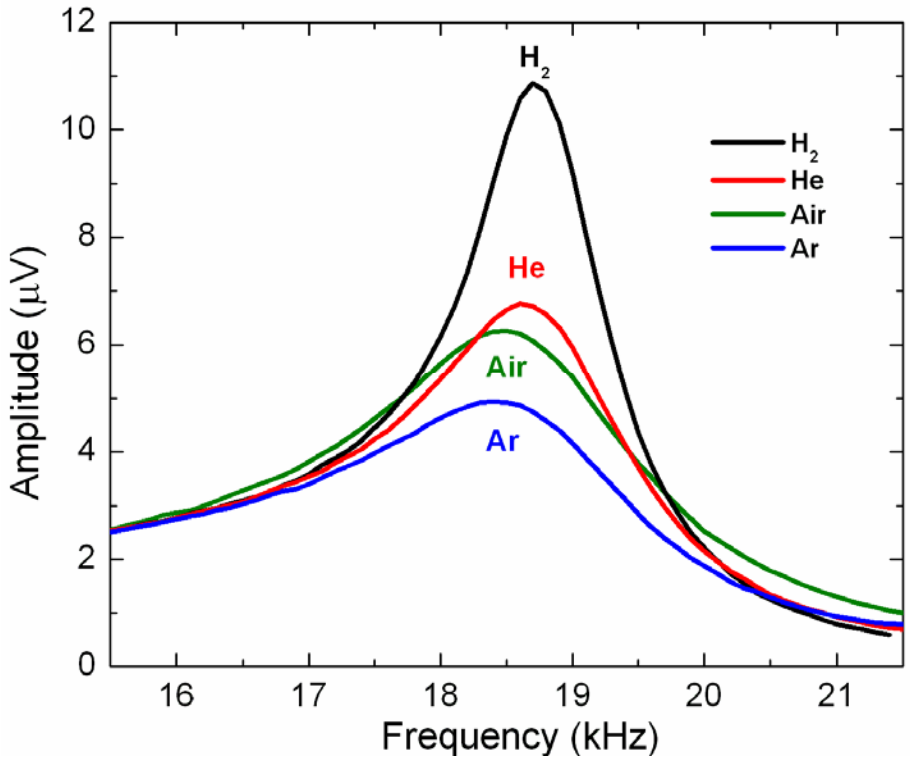

Figure 3.6 (b): Resonance frequency spectra under different gas environments at the 2nd harmonic at ambient pressure with V_{dc} = 9 V, V_{ac} = 10 V.

(III) Response at higher harmonics of the modulated charge

The systematic study of the responses of a different cantilever at higher harmonics in a He environment is conducted. It is observed that the signal amplitude was higher at the 2nd harmonic compared to the 3rd harmonic at the same pressure [2] (Figs. 3.7(a) and 3.7(b)). At the 3rd harmonic, a signal is measured at three times the driving frequency, leading to lower parasitic pickup due to the measurement further away from the driving frequency. Thus due to lower background signal, Q_E is higher at the 3rd harmonic than at

the 2nd harmonic, despite the lower amplitude [2]. For the 2nd harmonic, above 5 torr the amplitude (and thus Q_E) dropped drastically with increase in pressure upto 25 torr, in contrast to the gradual drop in amplitude with constant increase in pressure for the 3rd harmonic. Figures 3.7(a) and 3.7(b) show the nonlinear response of $1/Q_E$ to p in the viscous regime at the 2nd and 3rd harmonics. We started noticing a weak Duffing behavior only at the lowest pressure (5 torr) at the 2nd harmonic due to nonlinearities involved in the system, whereas the 3rd harmonic resonant peak showed obvious bending, indicating a strong Duffing (nonlinear) behavior even below 33 torr, making the Q_E calculation problematic. $1/Q_E$ increased linearly with increasing pressure, and then approached a constant above 100 torr at the 3rd harmonic so we plot the pressure range only up to 230 torr instead of 760 torr (ambient pressure).

At low pressures, f_0 behaved almost the same for both harmonics. The resonant frequency at the 3rd harmonic increased markedly with increasing p, while at the 2nd harmonic it slightly decreased towards the higher pressures (Fig. 3.8(a)). Similarly the signal amplitude at the 3rd harmonic decreased faster in the lower pressure region than the 2nd harmonic where the amplitude dropped more linearly with increase in pressure above 25 torr (Fig. 3.8(b)). These results show that the response of the cantilever at the 3rd harmonic is more sensitive at the lower pressures, whereas the 2nd harmonic can be employed very successfully at an ambient pressure. Thus, the use of a single cantilever at higher (2nd and 3rd) harmonics allows the access to different pressure regions enabling its use for various sensor applications.

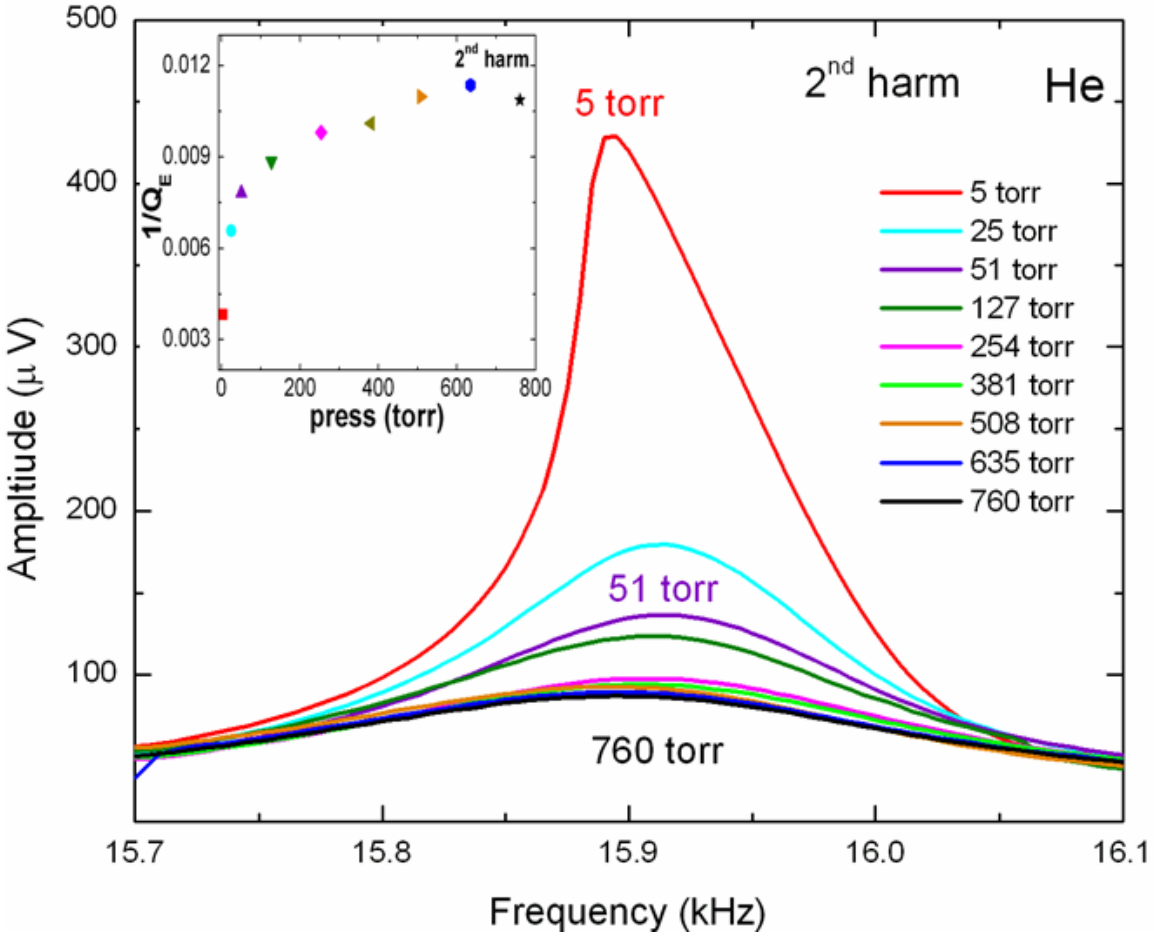

Fig. 3.7 (a): Amplitude response to chamber pressure at the 2nd harmonic. The inset shows the dependence of Q_E on the pressure at the 2nd harmonic at V_{dc} = 9 V, V_{ac} = 4.4 V.

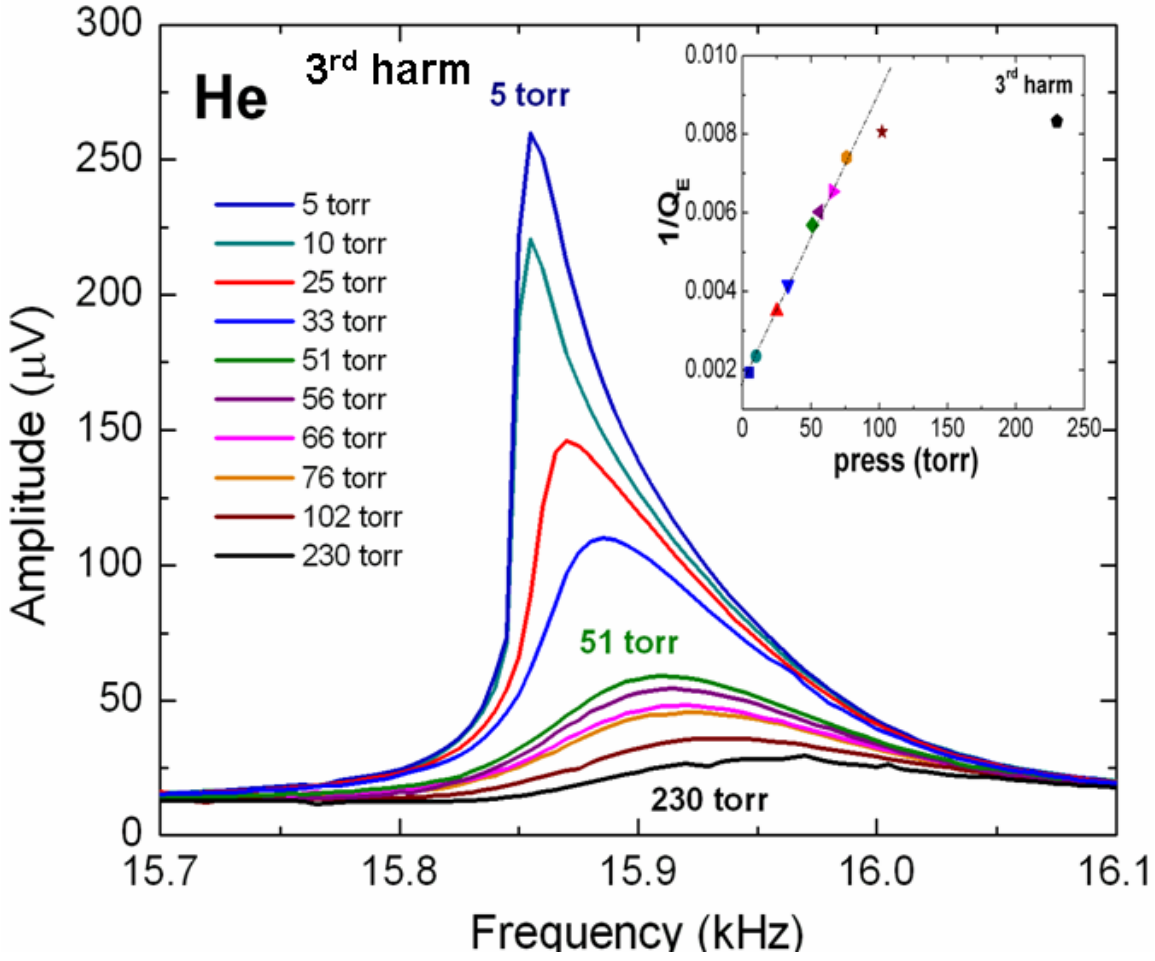

Figure 3.7(b): Amplitude response to chamber pressure at the 3rd harmonic. The inset shows the dependence of Q_E on the pressure at the 3rd harmonic at (V_{dc} = 9 V, V_{ac} = 6.2 V).

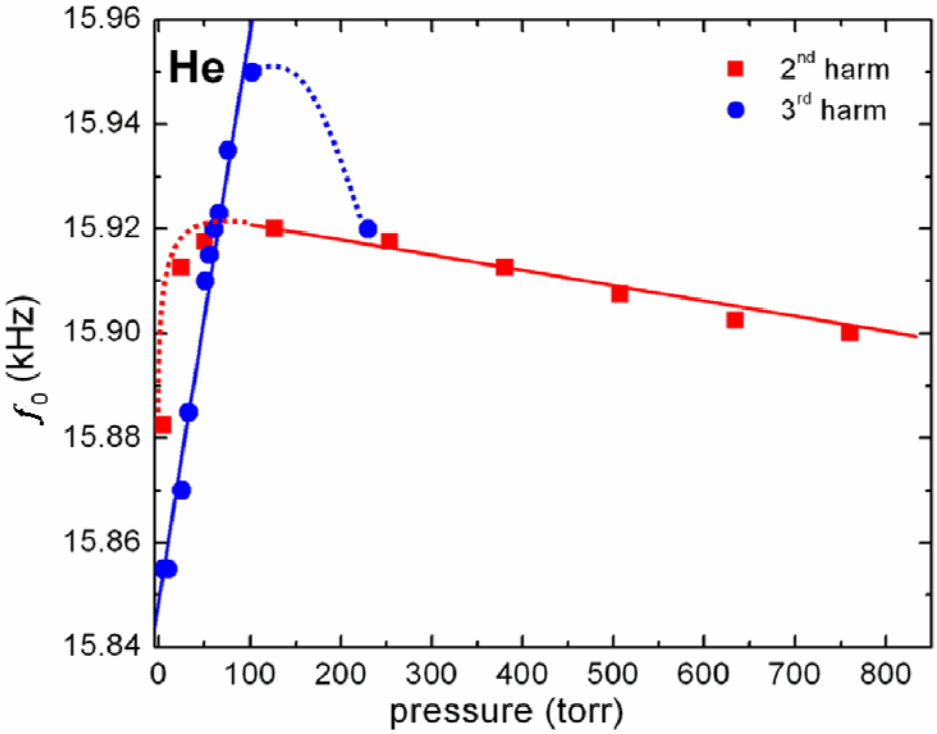

Figure 3.8 (a): Comparison of the resonant frequency of the cantilever as a function of pressure at the 2nd (V_{dc} = 9 V, V_{ac} = 4.4 V) and 3rd (V_{dc} = 9 V, V_{ac} = 6.2 V) harmonics in a He environment. The different harmonics may allow the measurement of the pressure over a larger region than a single harmonic.

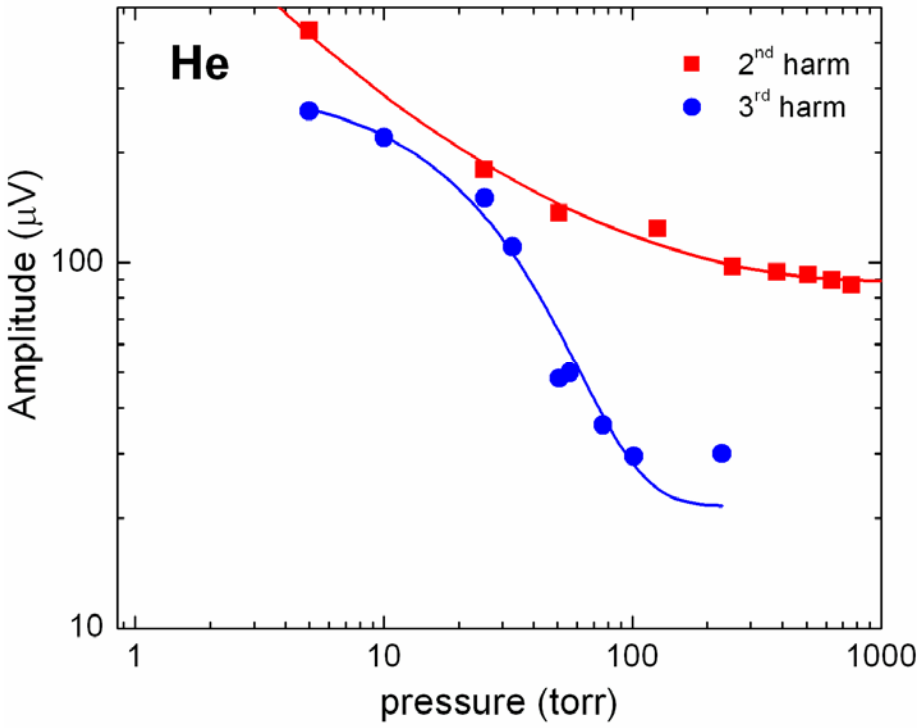

Figure 3.8 (b): Comparison of amplitudes at f_0 of the cantilever as a function of pressure at the 2nd (V_{dc} = 9 V, V_{ac} = 4.4 V) and 3rd (V_{dc} = 9 V, V_{ac} = 6.2 V) harmonics in a He environment. The red line is used as guide to the eye for low pressures at 2nd harmonic and blue line is used for 3rd harmonic.

Conclusions

HDR offers unique features, particularly electrostatic excitation and detection. The microcantilever demonstrates a quality factor of ~10000 at 10^{-3} torr, and a usable response in the range from 10^{-3} to 10^{3} torr. Here we have shown that currently our sensor is fairly sensitive compared to the one presented by Bianco *et al* [66]. The nonlinearities

present in HDR make it special and more useful than the rest of the other resonance detection methods. While the HDR method may not be as sensitive as other techniques, the other techniques are often more bulky, expensive, and prone to errors. Furthermore, it may also be easier to fabricate a device that is all silicon than one which contains piezoelectric and laser components. The responses of Q_E to pressure in the viscous and molecular regions are similar to those measured with a more linear system that used piezoelectric excitation and optical detection [66]. The experimental results are in reasonable agreement with theoretical calculations, despite the nonlinearities involved: Q is inversely proportional to (i) pressure in the molecular region and (ii) the square root of the mass of the gaseous medium. At the 3rd harmonic, the cantilever showed a stronger dependence on p in the low pressure regime, whereas an almost uniform and linear response was observed at the 2nd harmonic over the entire pressure range. The benefit of switching between different harmonics depending upon the pressure regime can provide us with a higher flexibility as a pressure sensor. We are exploring the possibility of using carbon nanotubes/nanostructures which we expect will have lower intrinsic damping for sensing even lower pressures.

.

CHAPTER FOUR

ULTRA-SENSITIVE DUFFING BEHAVIOR OF A MICROCANTILEVER

Introduction

Micro electro-mechanical systems (MEMS) enable the fabrication of fully integrated sensors and actuators for continuously growing range of applications. A characteristic feature of many MEMS devices that has recently received much attention is the nonlinear response to ac driving signals [77]. It has been postulated that nonlinear spectral features may allow a greater dynamic range and enhance the sensitivity [78]. We have been studying the behavior of electrostatically driven and measured cantilevers and noticed that it is possible to drive them hard enough to observe Duffing-like jumps in their amplitude- frequency behavior [74]. Typically in a Duffing resonator, above some critical driving amplitude, the response becomes a double-valued function of frequency in some finite frequency range. The presence of the bistable region results in a dramatic jump transition from a near-zero solution to one of the high amplitudes. Using the Duffing-like behavior of microcantilever provides us with the ability to engineer the ultra-high-sensitivity of this bistability [79, 80]. This Duffing-like behavior could be useful in sensing technologies [81].

Nonlinearity effects on resonance are often described using the classical Duffing equation [82],

$$\ddot{x} + \omega_o^2 x = -2\varepsilon\gamma\dot{x} - \varepsilon\alpha x^3 + E(t) \tag{4.1}$$

where ε is a small parameter, E is an externally applied force, γ is positive viscous damping, ω_0 is the angular resonant frequency and α can be either positive (hard spring) or a negative (soft spring) constant. Here

$$E(t) = Z\cos\Omega t \tag{4.2}$$

where Ω is the angular driving frequency and Z is a constant. Equation 4.1 can be solved by either the method of multiple scales [83] or the method of harmonic balance [82]. However, we do not see the typical Duffing behavior, but rather the behavior which mimics it which could be because of more complex nonlinearities than the classical case. Henceforward we will call these Duffing like effects simply the Duffing behavior. Currently very little is known about the physical mechanisms underlying the Duffing behavior of harmonics other than the first. The published literature mainly focuses on the theoretical understanding of the mechanisms involved in Duffing behavior and proposes its application as a sensor. But we did not find a report that experimentally demonstrates a sensing based on the Duffing behavior.

In this chapter we investigate the properties of an electrostatically driven microcantilever exhibiting Duffing-like behavior using HDR technique. Its potential use as a highly sensitive sensing platform is discussed. We study the effect of damping on the Duffing behavior of a microcantilever in hydrogen, air and vacuum. We also demonstrate the tuning of the transition frequency of a Duffing resonator in both the forward and backward directions by voltage changes and evaluate some potential applications associated with different regimes of frequency tuning. The response of the higher

harmonics of the measured charge on the cantilever induced by an ac voltage that drives the counter electrode is investigated. In particular, we trace the Duffing behavior at the higher harmonics (up to the 6^{th} harmonic) as a function of gap distance between the cantilever and counter electrode.

Mathematical Model

A literature survey shows that the theoretical interpretations of basic Duffing behavior and the related nonlinearities have been extensively used in MEMS devices [78, 84-86]. We will present in this chapter a simple mathematical model of the nonlinearities present in our system leading to Duffing behavior. First the experimental set up for Duffing study using HDR method is discussed [2]. A silicon microcantilever and a tungsten tip (acting as a counter electrode) were brought into a parallel configuration with a gap distance (s) of 8-10 μm inside an evacuable glass chamber (as discussed in previous chapter in Fig. 3.1). We studied its Duffing behavior by driving the microcantilever into the nonlinear regime with appropriate ac and dc voltages applied to the counter electrode using our HDR setup.

Equation of motion

For simplicity, here we assume that the amplitude of the 1st mode is given by the single coordinate x [83], and the force can be given as,

$$F = ma$$
$$F = m\frac{d^2x}{dt^2}$$
$$F = -\frac{d}{dx}\left(\frac{1}{2}CV^2\right) = m\frac{d^2x}{dt^2}$$

where the capacitance $C = C_0 + C_1'x + C_1''x^2 + \ldots$ and the voltage $V = V_{dc} + V_{ac}\cos(\Omega t)$

Hence, the Coulomb force F_C on our cantilever can be written as the spatial derivative of the Coulomb energy [2]:

$$\begin{aligned} F_C &= d[\tfrac{1}{2}C(V_{dc} + V_{ac}\cos(\Omega t))^2]/dx \\ &= \frac{1}{2}\{V^2{}_{dc} + 2V_{dc}V_{ac}\cos(\Omega t) + \frac{1}{2}V_{ac}^2[1+\cos(2\Omega t)]\}\frac{dC}{dx} \end{aligned} \tag{4.3}$$

where C is the capacitance of the cantilever-counter electrode system, and Ω is the angular driving frequency.

When driven by these oscillatory and static voltages, the cantilever is forced according to equation (4.3). This not only creates a force with two harmonically related frequencies, f and $2f$, but also adds the nonlinearities due to the roughly $1/x^2$ dependence of the capacitance. This leads to a significant change in the spring constant with applied voltages and the presence of many harmonics in the deflection, as well as subharmonic resonances.

For an electrostatically driven cantilever, we can write

$$m\frac{d^2x}{dt^2}+\gamma\frac{dx}{dt}+kx=F_C \tag{4.4}$$

where m is the effective mass of the cantilever, k the effective spring constant and γ the damping constant when the cantilever is vibrating in its first mode. The capacitance in (4.3) can be expanded in a Taylor series in terms of the deflection.

$$C(x,t)\approx C_0+C_1x(t)+\frac{1}{2!}C_2x(t)^2+\ldots \tag{4.5}$$

where $C_n=\dfrac{\partial^n C}{\partial^n X}_{x=0}$. Then equation (4.4) becomes

$$\begin{aligned} &m\frac{d^2x}{dt^2}+\gamma\frac{dx}{dt}+kx=F_0+\frac{\partial F}{\partial x}x+\ldots \\ &=\frac{1}{2}(C_1+C_2x+\frac{1}{2}C_3x^2\ldots)\{V^2{}_{dc}+2V_{dc}V_{ac}\cos(\Omega t)+\frac{1}{2}V_{ac}^2[1+\cos(2\Omega t)]\} \end{aligned} \tag{4.6}$$

The time independent term on the right involving C_1 amounts to a zero shift and can be eliminated with the substitution

$$\zeta=x-\left(V_{dc}^2+\frac{1}{2}V_{ac}^2\right)C_1/2k \tag{4.7}$$

The term involving C_2 is equivalent to a softening of the spring constant as the cantilever approaches the counter-electrode. If we set

$$\kappa=k-\left(V_{dc}^2+\frac{1}{2}V_{ac}^2\right)\left(\frac{1}{2}\frac{\partial^2C}{\partial\zeta^2}\Big|_{\zeta=0}+\ldots\right) \tag{4.8}$$

we can write the equation of motion as

$$m\frac{\partial^2\zeta}{\partial t^2}+\gamma\frac{\partial\zeta}{\partial t}+\kappa\zeta=(C_2\zeta+\frac{1}{2}C_3\zeta^2+\frac{1}{6}C_4\zeta^3\ldots)\left[V_{dc}V_{ac}\cos(\Omega t)+\frac{1}{2}V_{ac}^2\cos(2\Omega t)\right] \tag{4.9}$$

From equation (4.9) we can see that (i) the effective spring constant is affected by the applied ac and dc potentials; and (ii) a quadratic term $\frac{1}{2}C_3\zeta^2$ and a cubic "Duffing" term $\frac{1}{6}C_4\zeta^3$ are present in the equation of motion. Note that there are also terms involving ζn in κ. Since the cantilever resonates nonlinearly due to the geometry of the electrodes, when the deflection $x(t)$ is expanded as a Fourier series given by,

$$x(t) = \sum_{n=1}^{N} A_n \cos(n\Omega t + \delta_n) \tag{4.10}$$

many of the *An*'s will be finite. There may also be an additional cubic nonlinearity due to the elastic properties of the beam and nonlinear damping [80].

The response curves for our cantilevers have two stable states due to these nonlinearities (Fig. 4.1), which lead to the so-called "jump" phenomena [83]. When the driving voltage frequency is slowly increased at constant amplitude, the response amplitude will jump up at a frequency less than the resonance frequency (f_0) that is measured at low amplitude. The response amplitude will also jump down at a frequency less than (f_0) when the frequency is decreased from well above f_0. One speaks of "hard" and "soft" springs, in which the dynamic spring constant k_d = dF/dx increases or decreases as x increases. For hard springs, the resonance curve bends toward higher frequency. For soft springs, such as those of our experiments, the resonance peak bends toward lower frequencies. In the frequency domain in which two stable steady-state solutions exist, the initial conditions determine which of these represents the actual

response of the system. Thus, in contrast with linear systems, the steady-state solution of a nonlinear system can depend on the initial conditions [83].

Duffing Mechanism

Figure 4.1 represents the stable steady state solutions under different excitation amplitudes. Referring to Fig. 4.1 we define some terminologies in the A vs. f curves which we use in the experimental data analysis. In the first case where the excitation amplitude is less than the critical amplitude, only one solution exists, and no bistability is possible (Fig. 4.1(a)). For the case when the excitation amplitude equals the critical amplitude, the system is on the edge of the bistability, and there exists one point where A vs. f has an infinite slope showing incipient Duffing (Fig. 4.1(b)). In the case when the excitation amplitude is greater than the critical amplitude the system is in the bistable regime having three possible solutions over some range of frequencies. Two of these solutions are stable. With increasing frequency the solution jumps from the low amplitude stable solution (region I) to another high amplitude stable solution (as shown by solid arrows) bypassing the unstable (experimentally unobservable) solution (shown in red in region II). The large amplitude solution is stable and decreases with increasing driving frequency f and finally enters into region III. In region (III) the system has only one stable solution which with decreasing frequency bifurcates into a stable solution and an unstable (red curve) solution. This stable solution grows in amplitude higher than the stable solution accessible with increasing frequency as f continues to decrease (region II). When the slope becomes infinite, this stable solution drastically collapses to the low

amplitude solution which is stable again (shown by dashed arrows in region I). Figure 4.1(c) shows the expected behavior in the 1st harmonic for a large third order non-linearity [85].

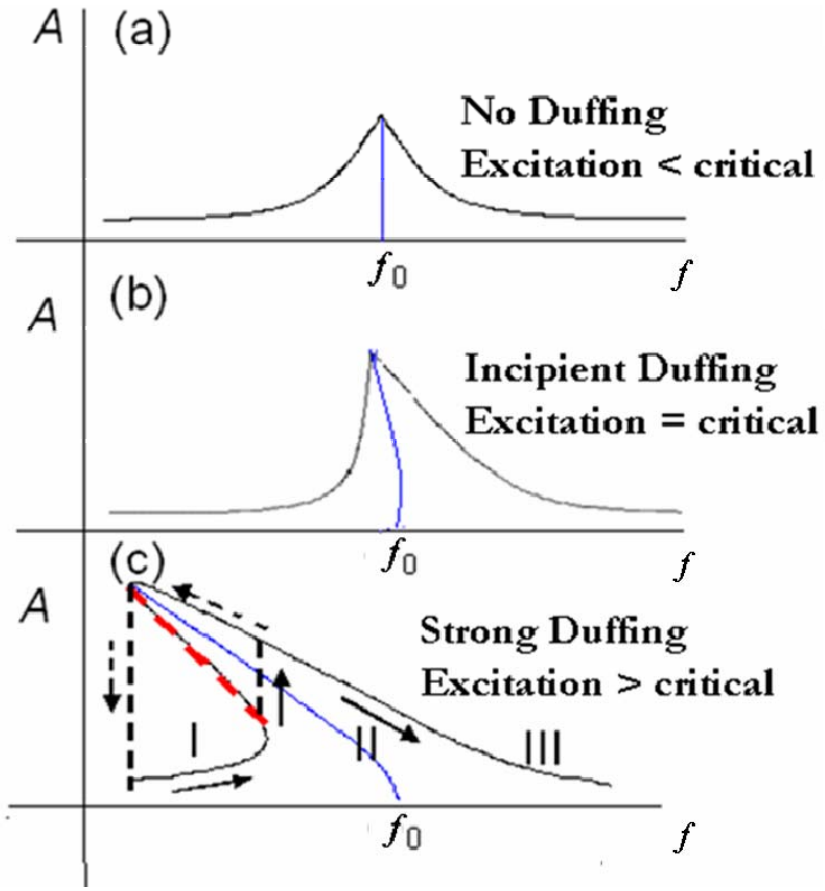

Figure 4.1: Cartoon of steady state solutions under different excitation amplitudes showing three stages of Duffing behavior [78]. The natural resonance frequency (f_0) as a function of A is shown by the blue line which differs from the f.

Experimental Setup

For this study we have used commercially available, one side gold-coated, tipless microcantilevers from Micromasch, typically 35 μm wide, 2 μm thick and 350 μm long. All experiments described in this manuscript are performed at room temperature and on the same cantilever. The response of the resonating microcantilever is compared in air, hydrogen and low vacuum (5 torr) to understand the effect of damping on Duffing behavior. Furthermore, we record the Duffing behavior at higher harmonics (from 3^{rd} to 6^{th}) of the induced charge on the cantilever at two different gap distances between the cantilever and counter electrode (4 μm and 8 μm). Since the non-linearities are sensitive to small changes in geometry, the reproducibility of the results is checked. The sensitivity of our Duffing resonator is measured by (i) pumping down the chamber to 5×10^{-5} torr (ii) changing the pressure to 7×10^{-5} torr, the least change that we could make with our experimental set up, triggering the Duffing behavior by this change in pressure.

Results and discussion

(I) Effect of ac - dc voltages on Duffing behavior

At the 1^{st} harmonic, the detected resonance signal is overwhelmed by the background signal due to the parasitic capacitance and manifests itself as a small peak at the resonance frequency of the cantilever [2]. At the second and higher harmonics of the driving frequency (*f*), the signal stemming from the parasitic capacitance is avoided,

permitting the detection of resonance with good signal to background ratios [2]. Interestingly, the Duffing behavior is more visible and prominent at the 3rd harmonic than at the 2nd harmonic in air [3]. Hence all the experimental results were recorded at the 3rd and higher harmonics of the ac voltage applied to the counter electrode. The ac voltage applied to the counter electrode is swept with both increasing and decreasing *f*. Using a dark field microscope, we estimate that the cantilever deflection amplitude is roughly one quarter of the gap distance with an 8 μm gap distance between cantilever and the counter electrode at 8 V_{dc} and 5 V_{ac}. As seen in Fig. 4.2(a) at V_{ac} = 2 V and V_{dc} = 8.5 V under vacuum (5 torr), Duffing behavior is not observed. A polar plot with the amplitude as the radius and the phase of the lock–in amplifier as the angle for the first harmonic of a damped SHO is nearly a circle starting and ending on the origin. It is traversed counter clockwise with increasing *f* and starts along the 180˚ axis. We find that the signals at higher harmonics also give a similar circle under the experimental conditions described in Fig. 4.2(a). Fig. 4.2(b) is a polar plot of the 2 V_{ac} data of Fig 4.2(a), mapped through the transition with both increasing and decreasing *f*. Note that the circle starts and finishes off the origin. This offset is due to the presence of a coherent background signal present in our experimental setup. The circle seen is the vector sum of the background signal and the signal from the cantilever. The initial dip in the amplitude vs. frequency plot (Fig. 4.2(a)) is then seen to be due to the vector sum of the signal and the background and the dip is shown by the black arrow in the polar plot (Fig. 4.2(b)). Such a dip was not seen in case of hydrogen or air. The inset in each of the following figures is a polar plot of the data in the main panel. As the ac voltage was increased to 3 V, Duffing behavior is

observed for both increasing and decreasing *f*. Thus, consistent with the discussions on Equation of Motion, V_{ac} is one of the key parameters for inducing Duffing behavior. The polar plots consist of circular arcs at high and low *f* when the nonlinearities are large enough to give rise to a Duffing behavior. These arcs are connected by the straight lines at the Duffing jumps (Fig. 4.2(c)). As the nonlinearities grow the decreasing frequency arc changes its curvature as shown in Fig. 4.2(c). Similar Duffing behaviors are seen under various experimental conditions, and are summarized in table 4.1. The experimental results are detailed in subsequent figures.

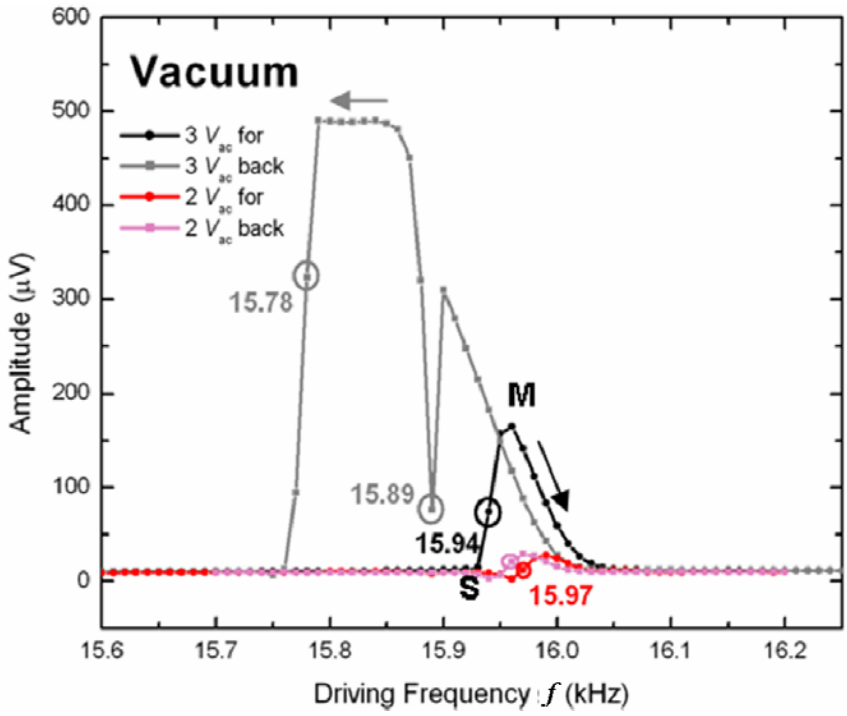

(a)

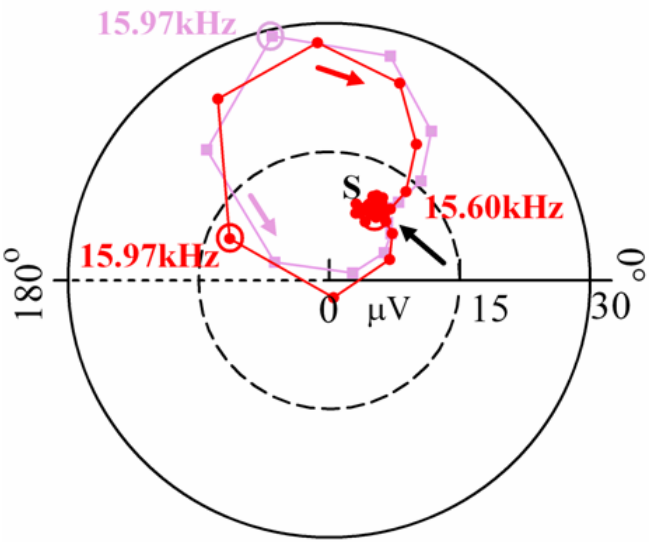
15.97kHz
S
15.60kHz
15.97kHz
180°
0°
0
μV
15
30

(b)

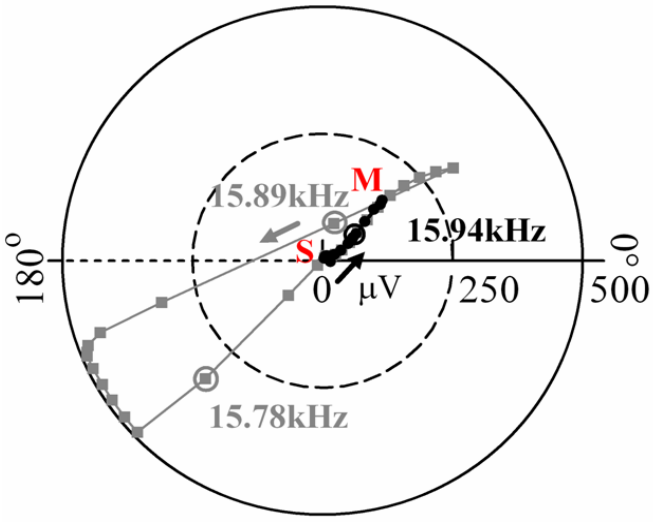
15.89kHz
M
15.94kHz
S
180°
0°
0
μV
250
500
15.78kHz

(c)

Figure 4.2: (a) Frequency spectra under vacuum. Dark circles are used for increasing and light circles for decreasing f. At V_{ac} = 2 V, there are no Duffing jumps. Increasing V_{ac} to 3 V gives a spectrum showing Duffing jumps. The circled points are for comparison with Figs. 4.2(b) and 4.2(c). The points S and M are the start and maxima of the amplitude jumps in both amplitude (Fig. 5.2(a)) and polar (Fig. 5.2(c)) plots with increasing f.
(b) Data at 2 V_{ac} from Fig. 4.2(a) in a polar plot in which the angle is the phase and the radius is the amplitude of the response with increasing (dark circles) and decreasing (light circles), f as a parameter. Tracing the vector amplitude shows why there is a dip in the amplitude near resonance in the amplitude vs. Ω spectrum shown by the black arrow.
(c) Data at 3 V_{ac} from Fig. 4.2(a) in a similar polar plot.

Figure	Gas	# of Harm	Gap size (μm)	V_{ac} (V)	V_{dc} (V)	F_{up}(kHz)[ΔA (μV)]	F_{down} (kHz) [ΔA (μV)]	Step size (kHz)
Fig. 3 ($2V_{ac}$)	vacuum	3	10	2	2	none	none	0.01
Fig. 3 ($3V_{ac}$)	vacuum	3	10	3	3	15.97 [160]	15.79 [500] 15.89 [60]	0.01
Fig. 4	vacuum	3	10	2.6	8.5	15.98 [100]	15.86 [340] 15.8 [465]	0.01
Fig. 5	H_2	3	10	7	8.5	15.86 [235]	15.79[450] 15. 7 [535]	0.001
Fig. 6	air	3	8	9.75	9.6	15.45 [410]	15.42 [410]	0.01
Fig. 7	air	4	8	9.75	9.6	15.44 [170]	15.42 [160]	0.01
Fig. 8	air	5	8	9.75	9.6	15.43 [55]	15.44 [43]	0.01
Fig. 9	air	6	8	9.75	9.6	15.46 [27]	15.44 [23]	0.01
Fig. 10	air	3	4	3	8.5	14.3 [160]	13.7 [140] 12.5 [220]	0.1
Fig. 11	air	4	4	3	8.5	13.9 [58] 14.1 [17]	13.7 [155] 12.5 [120]	0.1
Fig 12	air	5	4	3	8.5	13.8 [95] 14.3 [95]	13.4 [97] 12.3 [93]	0.1
Fig. 13	air	6	4	3	8.5	13.8 [8] 14.2 [8]	13 .5 [7.5] 12.2 [9]	0.1

Table 4.1: Summarizing Duffing behavior under various experimental conditions.

The polar plots corresponding to amplitude data shown in Fig. 3.7(b) at 3rd harmonic is shown in Fig. 4.2 (d) at various pressures. It started with a perfect circle (as expected) at 230 torr slowly growing in amplitude at lower pressures and then leading to

ellipsoidal at 33 torr showing incipient Duffing behavior. Finally we observed circular arcs connected by straight lines exhibiting strong Duffing behavior at 5 torr.

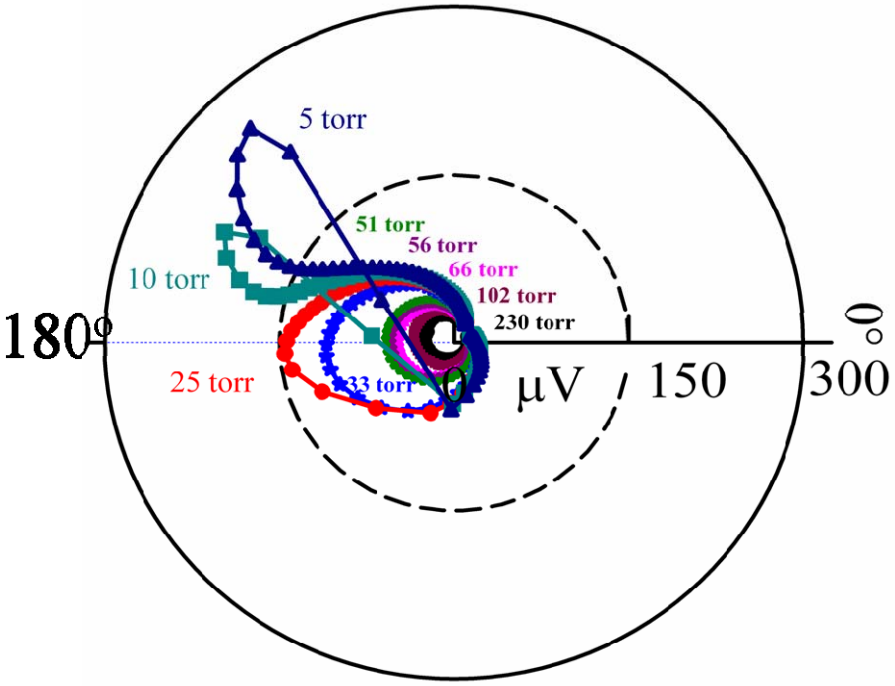

Figure 4.2 (d): Data corresponding to Fig. 3.7 (b) in polar plot under vacuum at 3rd harmonic (V_{dc} = 9 V, V_{ac} = 6.2 V).

(II) Effect of damping on Duffing behavior

The response of the microcantilever at the 3rd harmonic under vacuum (5 torr) and hydrogen (760 torr) with a 10 μm gap distance is shown in figs. 4.3 and 4.4. The microcantilever showed Duffing behavior with both increasing and decreasing *f* in both environments. Under vacuum (5 torr) (V_{ac} = 2.6 V, V_{dc} = 8.5 V) the amplitude jumped

from 10 μV to 100 μV with increasing f and dropped from 465 μV to 10 μV with decreasing f (Fig. 4.3). For the hydrogen environment (V_{ac} = 7 V, V_{dc} = 8.5 V) the signal amplitude jumped from 20 μV to 235 μV with increasing f (Fig. 4.4) and jumped down from 525 μV to 10 μV with decreasing f. As expected, the spectra with increasing and decreasing f overlapped fairly well away from the two transition f's. Hence under both environments a strong Duffing behavior was observed while scanning in the backward direction at the jump down frequency. We find high sensitivity of this Duffing system near its bistability point in a gaseous environment.

Figure 4.5 shows similar data for air, the most strongly damped of the three environments investigated. Data taken at the same gap distance and applied voltages (not shown) showed that higher the damping, higher the transition frequencies, as expected. The portion of the canonical circle on the polar plot that was traversed also increased with increasing damping. Figure 4.5 shows an incipient Duffing behavior having a very small difference ($\Delta_{+-} = f_- - f_+$) in the frequency f_+ at which the amplitude jump is observed with increasing f and the frequency f_- at which the amplitude jumps while decreasing f at the 3rd harmonic in air (V_{dc} = 8.5 V and V_{ac} = 9.75 V) as compared to the previous results under hydrogen and vacuum environments.

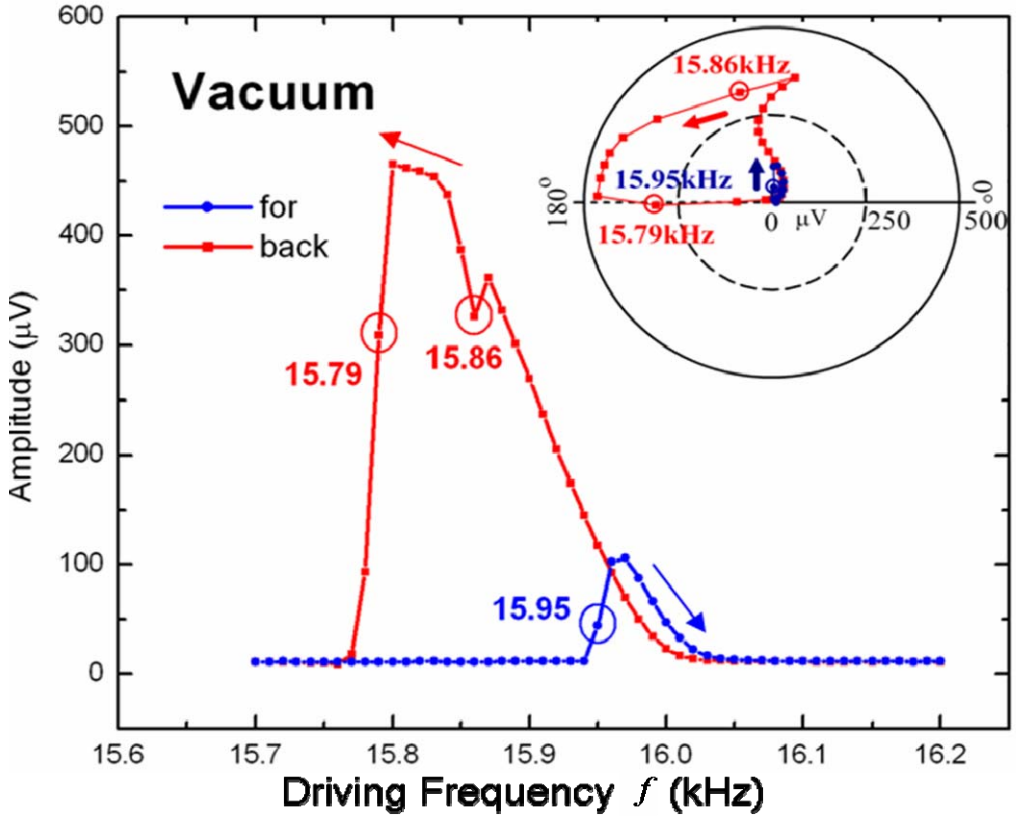

Figure 4.3: Measured frequency spectra under vacuum (5 torr) with increasing and decreasing *f*. The inset shows the polar plot of the same data mapped with increasing and decreasing *f*.

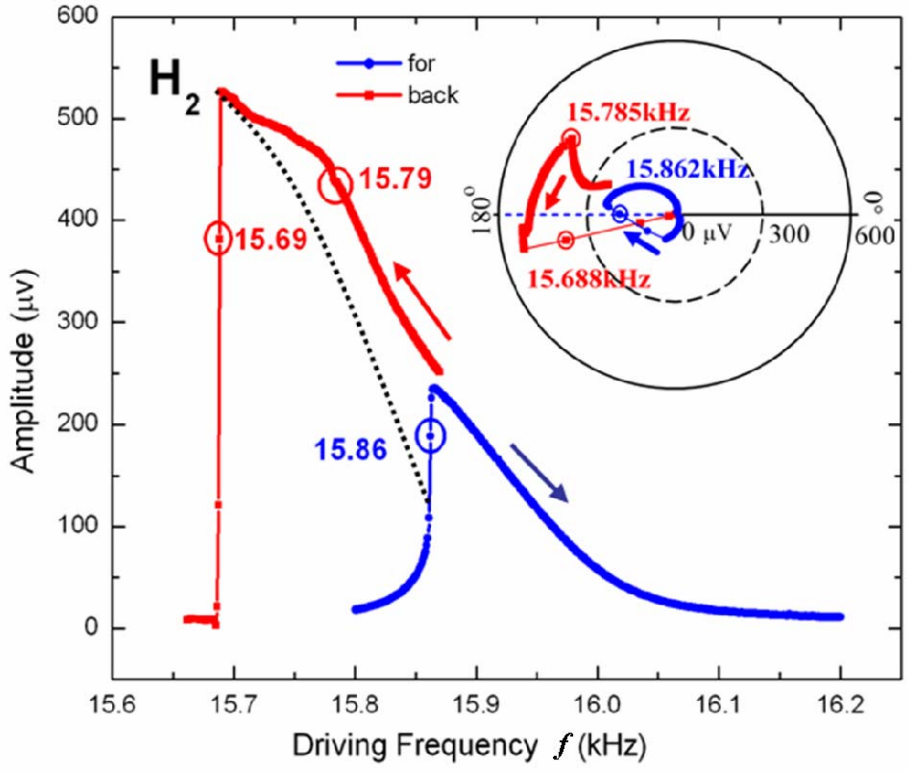

Figure 4.4: Measured frequency spectra under 760 torr of hydrogen with increasing and decreasing *f*. The inset shows the polar plot mapped with increasing and decreasing *f*. The dotted line is a guide to the eye, as a rough indication of where the resonance frequency might be as a function of amplitude. On the polar plot, note that the stable states are largely circular arcs, with an odd change in curvature in the decreasing *f* data near 15.79 kHz. The points that occur in the straight line portions of the polar plot may be in part due to transient and or unstable states.

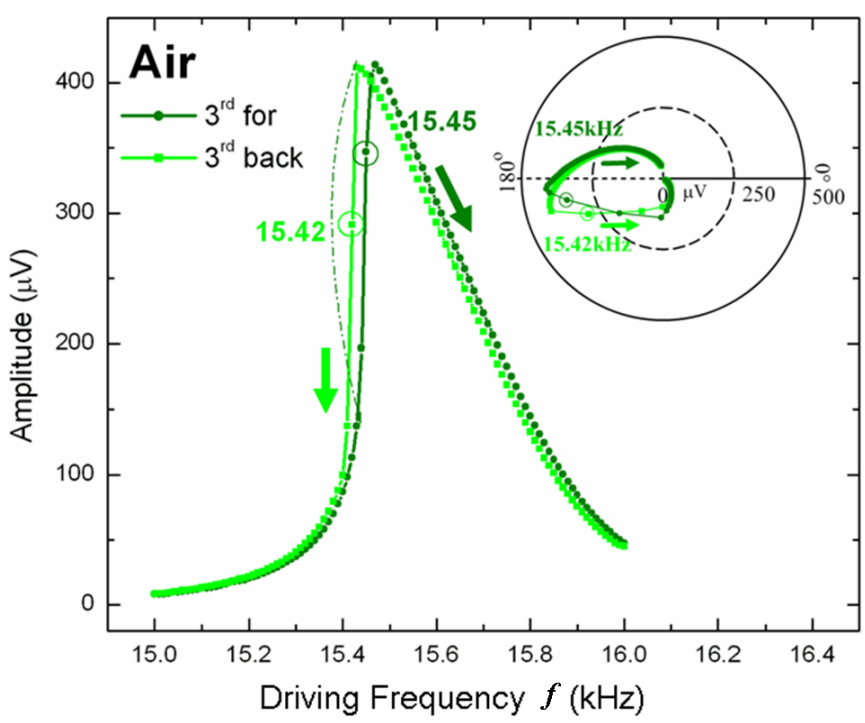

Figure 4.5: Measured frequency spectra in air at 3rd harmonic with an 8 μm gap distance with increasing and decreasing *f*. The inset shows the polar plot mapped with increasing and decreasing *f*.

(III) Duffing behavior at 4th to 6th harmonics at 8 μm gap distance:

Next we discuss about the behavior in air at the 4th, 5th and 6th harmonics. As the harmonic number is increased the magnitude of the signal is decreased along with the decrease in the background except at the 5th harmonic, leaving the signal to background ratio about the same. The signal amplitude dropped from 410 μV at the 3rd harmonic to 170 μV in the 4th harmonic spectrum at *f*. (Fig. 4.6) [11], with slightly stronger Duffing behavior with increasing *f* than with decreasing *f*. The polar plot is shifted by about

180˚. However in the case of the 5th harmonic (Fig. 4.7) Duffing behavior was prominent at ω_+ with a noticeable dip in amplitude very close to the transition while sweeping in either direction. This dip is due to the presence of a larger background signal compared to the resonance, as can be best seen in the polar plot. The background signal is larger, which we believe to be due to the noise at that frequency in our lab. At the 6th harmonic, (Fig. 4.8) the signal to noise ratio is larger, as the coherent background signal is again low, which is obvious from the polar plot. Unlike the general case, from the 4th harmonic to the 6th harmonic the Duffing behavior became stronger with increasing f than with decreasing f. All results shown in Figs. 4.5 - 4.8 were recorded with an 8 μm gap between the cantilever and counter electrode. The time for the transient solution to decay to insignificance as the system goes from one steady state solution to the other is greater with decreasing f [74]. Therefore, typically the jump in amplitude in the forward direction is faster than the backward jump at any harmonic. Duffing behavior observed in air has a promising potential application as an irreversible "alarm" system operating in air as there is a transition between the two stable states at the jump frequencies which cannot be reversed easily.

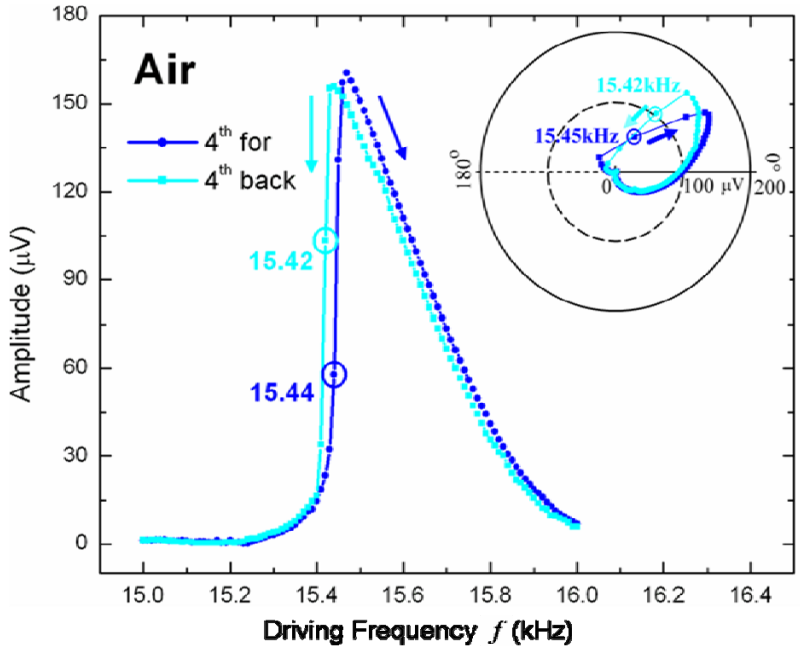

Figure 4.6: Measured frequency spectra in air at 4th harmonic with 8 μm gap distance with increasing and decreasing *f*. The inset shows the polar plot mapped with increasing and decreasing *f*.

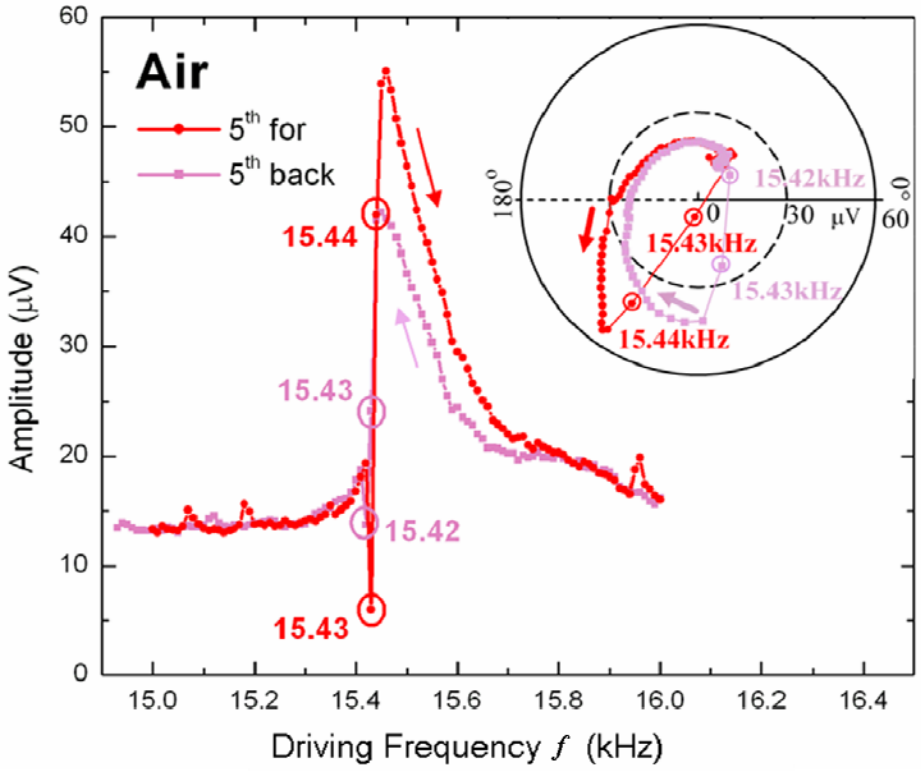

Figure 4.7: Measured frequency spectra in air at 5th harmonic with an 8 μm gap distance with increasing and decreasing *f*. The inset shows the polar plot mapped with increasing and decreasing *f*. The large offset from zero of the polar plot may be due to interfering signals at these frequencies in our lab.

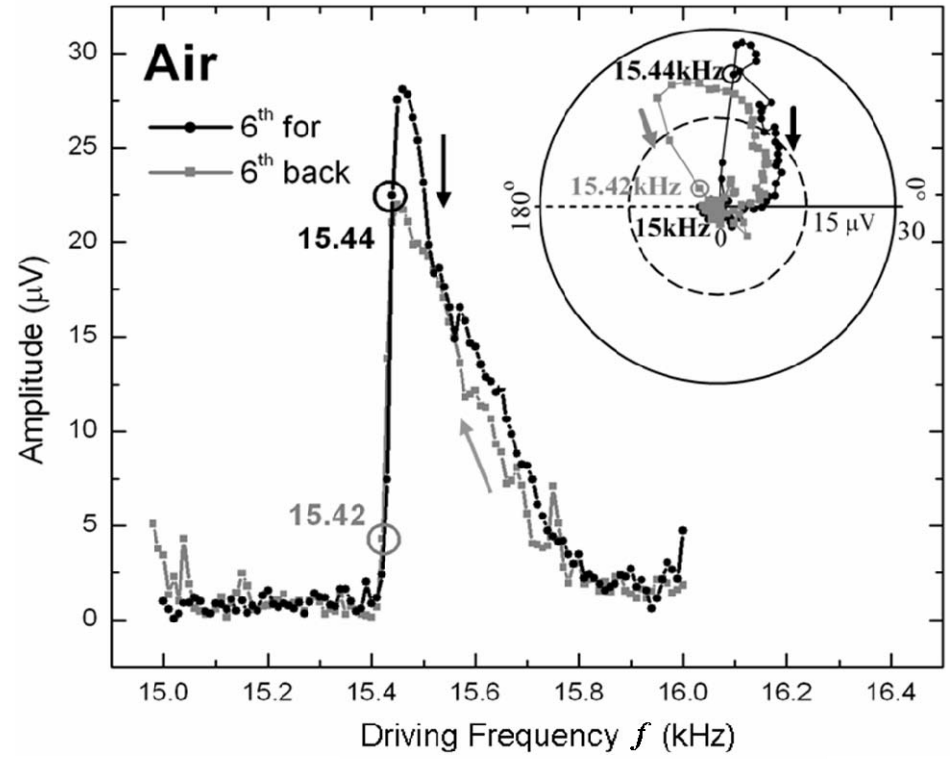

Figure 4.8: Measured frequency spectra in air at 6th harmonic with an 8 μm gap distance with increasing and decreasing *f*. The inset shows the polar plot mapped with increasing and decreasing *f*.

(IV) Duffing behavior at 3rd to 6th harmonics at 4 μm gap distance

To study the distance dependence of the Duffing behavior we decreased the gap distance between the cantilever and counter electrode to 4 μm, lowering V_{ac} and V_{dc} to keep the nonlinearities from increasing too much. Since decreasing the gap should increase the nonlinearities, we expect Duffing jumps to be more prominent. The striking

feature with a small gap distance is that there are often two peaks in the amplitude spectrum. Moreover, the resonance peaks taken with decreasing f spread over a broader range from 12 to 16 kHz for all the harmonics making it difficult to read out the exact f_{0-} from the amplitude plot. As always at the 3rd harmonic, (Fig. 4.9) Duffing behavior was observed more prominently with decreasing f than with increasing f at smaller gap distance. However the Duffing-like jump with decreasing f in air is more complicated than the results recorded with an 8 μm gap distance. The amplitude plot shows an initial drop followed by the usual jump in the amplitude with increasing f. This dip in the amplitude appears as a straight line in the polar plot. Data taken slower would presumably show just a single jump, as a sufficient time at the transition frequency might allow the transient solution to decay, and complete the jump in one frequency step. The jump in the polar vector at f_+ is smaller than at f_- as might be expected for a soft spring.

The maximum amplitude dropped from 290 μV (at the 3rd harmonic) to 155 μV at the 4th harmonic (Fig. 4.10). At the 5th and 6th harmonics the maximum amplitude dropped to 95 μV and 8 μV respectively, which was surprisingly small as compared to 27 μV at the 6th harmonic with an 8 μm gap distance (Figs.4.11 and 4.12). At the 5th and 6th harmonics in the frequency region ~14.5 kHz at f_+ and ~ 13.8 kHz at f_- there is probably only one stable state but the instantaneous drop/jump in amplitude is so sharp that it mimics Duffing behavior. The highlighted 'step' like features (Fig. 4.11) in the frequency spectra in both directions might have potential applications such as switches or frequency filters. Remarkable differences are identified in the amplitude and the phase during the transition at 3rd and 4th harmonics as compared to 5th and 6th harmonics at lower gap

distance. This shows that the Duffing jumps are exaggerated when observed in the higher harmonics of the driving signal. Figure 4.13 shows all the Duffing responses at different harmonics for the 8 μm gap distance. It can be seen that the jump up frequency decreases with increasing harmonic. If this is correct, and not due to timing lags in the lock-in, it implies that the oscillation states of the harmonics are not locked together.

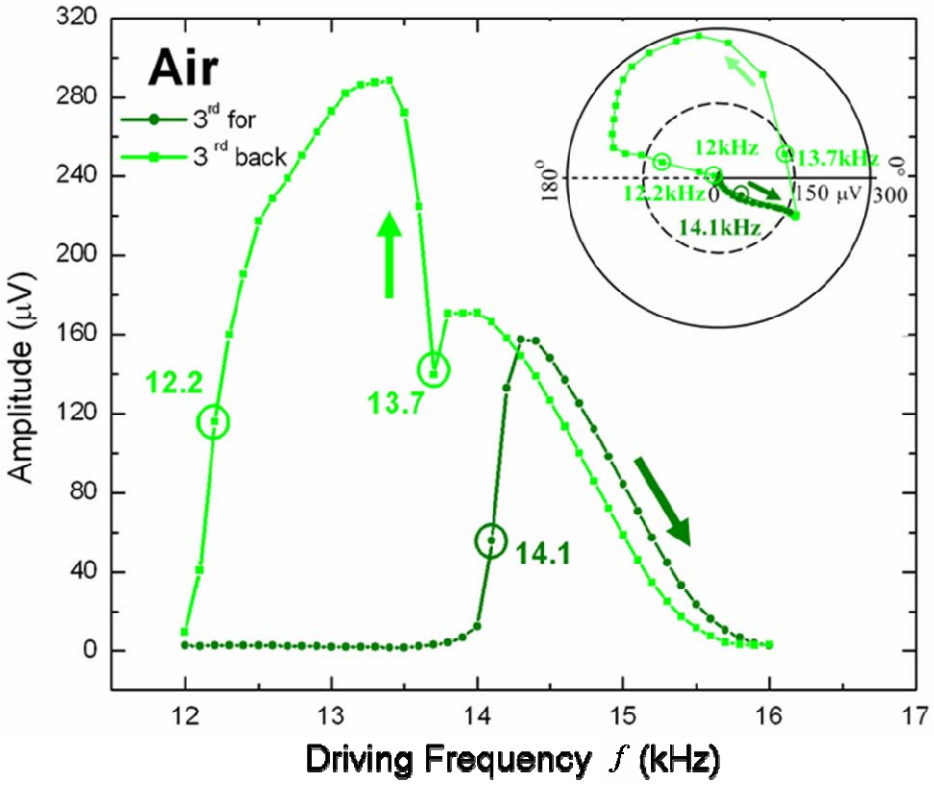

Figure 4.9: Measured frequency spectra in air at 3rd harmonic with a 4 μm gap distance with increasing and decreasing *f*. The inset shows the polar plot mapped with increasing and decreasing *f*.

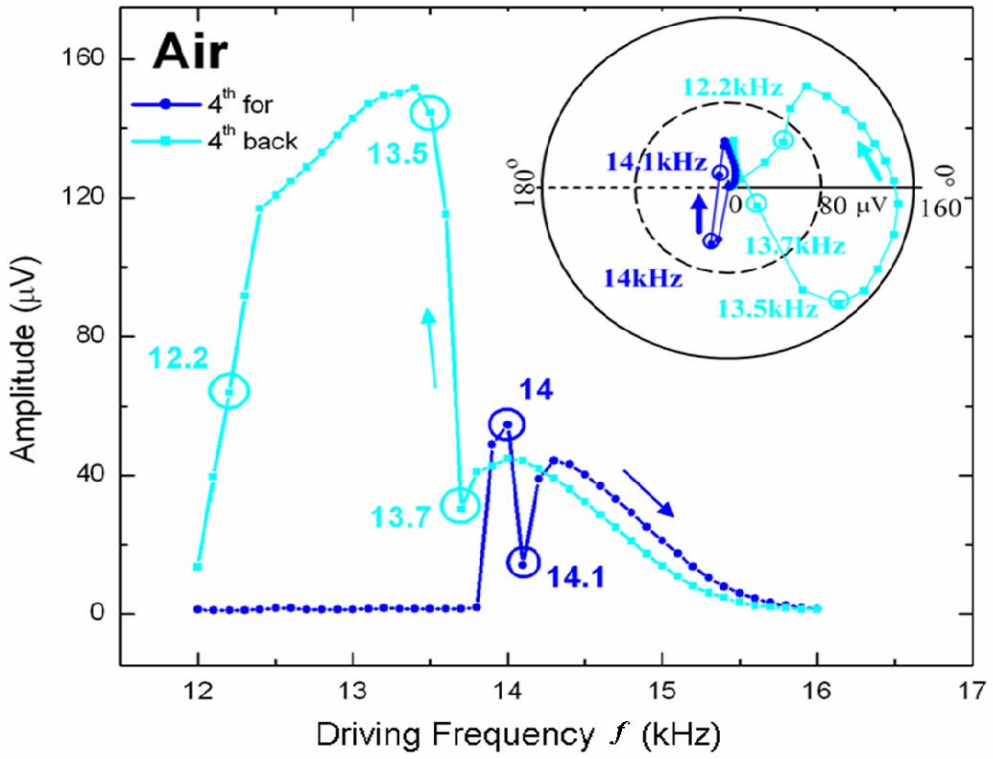

Figure 4.10: Measured frequency spectra in air at 4th harmonic with a 4 μm gap distance with increasing and decreasing *f*. The inset shows the polar plot mapped with increasing and decreasing *f*. The double jumps are observed in both the directions for this and higher harmonics.

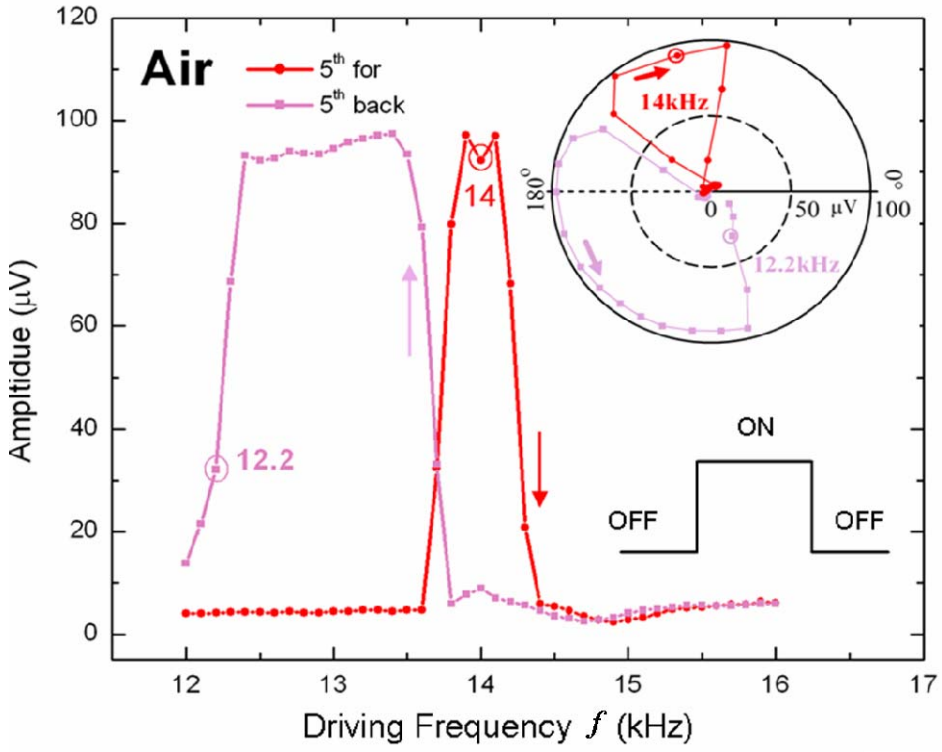

Figure 4.11: Measured frequency spectra in air at 5th harmonic with a 4 μm gap distance with increasing and decreasing *f* showing ON / OFF characteristics. The inset shows the polar plot mapped with increasing and decreasing *f*. Note that large parts of the polar plots are nearly circular arcs, and that the Duffing jumps are nearly straight lines on the polar plots.

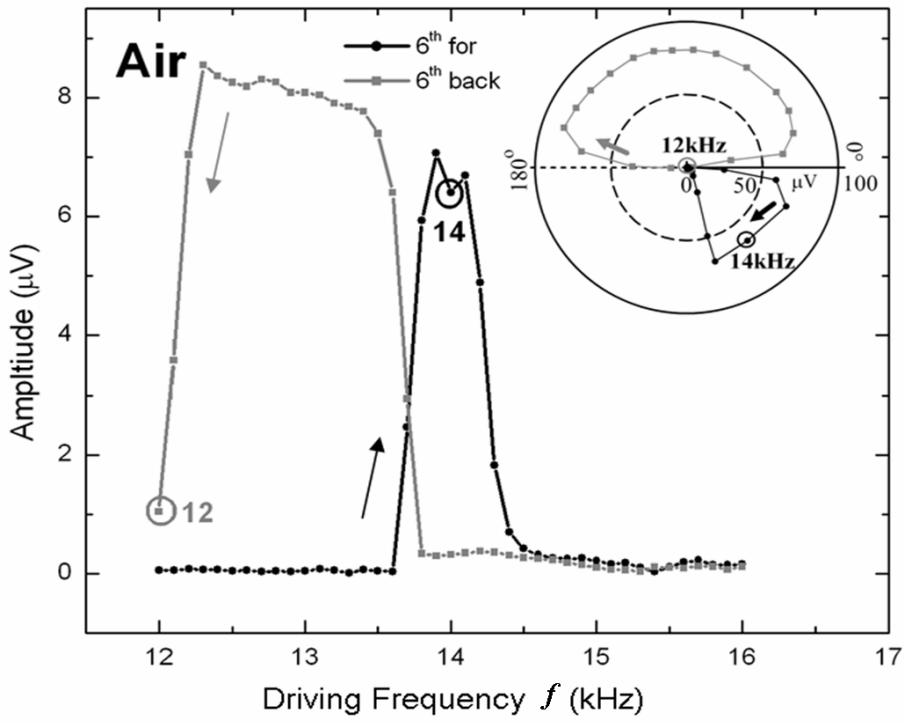

Figure 4.12: Measured frequency spectra in air at 6th harmonic with a 4 μm gap distance with increasing and decreasing *f*. Inset shows the polar plot mapped with increasing and decreasing *f*.

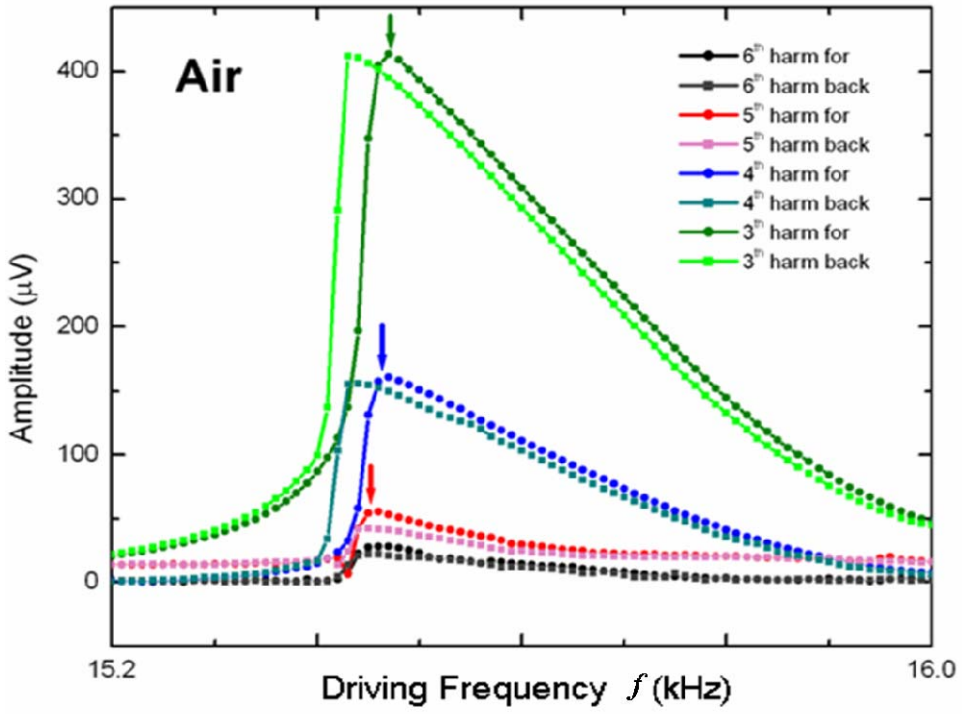

Figure 4.13: Measured frequency spectra in air with increasing and decreasing f at all the harmonics with an 8 μm gap distance (V_{ac} = 9.75 V, V_{dc} = 9.6 V). The arrows indicate that the transition frequencies are different at different harmonics and the frequencies decrease with increasing harmonics.

(V) Sensing the change in pressure using Duffing behavior

The basic principle involved in the use of Duffing oscillator for sensing application is to first adjust the frequency to be in the bistable region where there are two stable states at constant amplitude. In particular, when it is very close (~ 0.1 Hz) to the

transition frequency, a very small change in 'any' variable (like mass, pressure, temperature etc.) that will make subsequent small change in frequency would cause the amplitude (and phase) to jump up or drop down to the other stable state and can be sensed very easily. In order to illustrate this behavior we have carried out one preliminary experiment to show the practicality of using a Duffing cantilever for sensing. First we pumped down the system to 5×10^{-5} torr using the turbo pump. Then we exposed the system to air using a needle valve till the pressure increased to 7×10^{-5} torr keeping frequency constant (the least change we could get with our setup). This caused the resonance frequency to decrease at the 2^{nd} harmonic, making an immediate transition to the other state with an amplitude drop from 490 μV to 150 μV. Hence we could sense the pressure change of 0.00002 torr at 8 μm gap distance using our Duffing resonator (Fig.4.14). The insert in Fig. 4.14 shows the typical Duffing behavior underlying this experiment by varying *f* in small (0.1 Hz) increments at 5×10^{-5} torr. This spectrum is taken just before changing the pressure to 7×10^{-5} torr. To our knowledge, this work represents the first experimental demonstration of sensing a pressure change using the Duffing behavior.

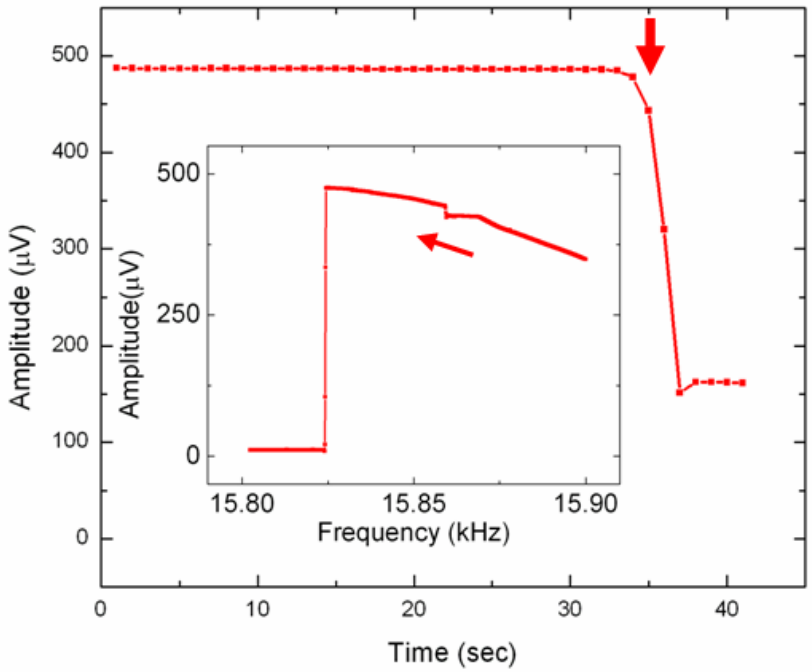

Figure 4.14: Sensing a pressure change from 5×10^{-5} torr to 7×10^{-5} torr using the Duffing behavior at the 2nd harmonic in the backward direction at 8 μm gap distance (V_{ac} = 1.3 V, V_{dc} = 4 V). After ~ 35 sec the pressure was increased as shown by the arrow causing the amplitude to drop instantly from 490 μV to 150 μV. The inset shows the Duffing behavior for this cantilever system as a function of small increments in frequency (0.1 Hz) while scanning in the backward direction at 5×10^{-5} torr just before changing the pressure.

Summary

The understanding of Duffing behavior under varying conditions and parameters provides important insights into the underlying physical mechanisms. Here we have explored the behavior of four of the harmonics of the driving frequency (3rd through 6th)

using an all-electric driving and sensing method. The harmonics that we observe are due to the nonlinearities of the cantilever, the drive system, and the sensing system. The harmonics behave in a complicated matter that has not been studied either analytically or computationally as yet. We observe significantly distinct features in the Duffing behavior at different gap distances and for each of the 4 higher harmonics examined. The rich structure of the harmonics, as illustrated in Figs 4.3 - 4.14, provides rich source of possible applications. The essence of using the Duffing behavior is to prepare the system with a Duffing jump not very far in frequency from the bifurcation point. One then has a bistable system that can be used to sense small changes or store one bit. Each harmonic has a slightly different Duffing behavior as a function of particular gap distance. Thus we can easily create a characteristic fingerprint for any particular variable to be sensed by tuning the different available knobs, such as the harmonics (3^{rd}-6^{th}), gap distances (4 μm, 8 μm) and environments (hydrogen, air and vacuum). We show one simple experiment in which a Duffing jump is triggered by a small pressure change. The usefulness of our Duffing system emphasizes the need for the theoretical understanding of its behavior at the higher harmonics. Based on all the characteristic features of Duffing behavior discussed in this chapter, it offers a wide spectrum of novel potential applications such as band pass filters, logic gates, logic switches, alarm systems and many more yet to be explored.

CHAPTER FIVE

ACTIVE SENSING IN AMBIENT CONDITIONS USING AN ELECTROSTATICALLY DRIVEN SILICON MICROCANTILEVER

Introduction

The advent of inexpensive, mass-producible and sensitive microcantilevers has accelerated the pace of innovations in the field of physical, chemical and biological sensing [13]. The recent developments in microfabrication technology have lead to miniaturization, improved dynamic performance, high precision, and increased reliability. It has been proposed that the high surface-to-volume ratio in microcantilevers ($\sim 10^3$ m^{-1}) can lead to large surface forces because of the surface-molecules interactions inducing the changes in Gibbs free energy [87]. When such interactions are restricted to one surface, the induced differential stress causes the cantilever to bend. Changes in the resonance frequency of the cantilever can also arise from changes in the cantilever mass due to adsorption of the molecules. As discussed in fourth chapter, cantilevers have been found to be useful as potential vacuum gauges, based on the damping of the surrounding gas. [3, 66] Moreover the sensitivity and specificity of microcantilever sensors can be enhanced by carefully optimizing the geometric design of the cantilever. For example, the mass sensitivity of a cantilever is inversely proportional to the square root of (ρd), where ρ is the density of the cantilever material and d is the thickness of the cantilever [13]. The most important figures of merit for any chemical, physical or biological sensor are response time, limit of detection (LOD), specificity, and reproducibility.

Although catalytic combustion, electrochemical galvanic cell, and infrared-based detection schemes are presently in use [88], the development of a capacitive detection based platform could definitely enhance the range of molecules that could be detected and discriminated. In the present chapter, we employ HDR to develop a silicon microcantilever based sensor which can be used for active sensing of gaseous species under ambient conditions. Our sensing platform measures the changes in the mechanical response (in amplitude and/or phase) of the vibrating cantilever in air at its resonant frequency when exposed to several vapors and gases. We demonstrate the detection of changes in the cantilever oscillations when exposed under ambient conditions to gases such as, H_2, D_2, nitrous oxide (N_2O), methane, and water vapor; and puffs of vapors of solvents such as, hexane, benzene, methanol and isopropanol [5]. Since cantilever-based sensors are extremely sensitive displacement sensors, they offer very little intrinsic chemical selectivity. Hence, in this case the chemically selective layers such as polymeric films, self-assembled monolayers, or antibody-antigen layers provide the enhanced chemical sensitivity. Later in this chapter, we also discuss functionalized cantilevers and show the preliminary results of detection of ammonia (NH_3) and hydrogen sulphide (H_2S) using them. Finally, the response of microcantilever when exposed to vapors of different flavors (i.e., the vapor-phase form of several beverages) illustrates this promising approach for an easy-to-use and highly versatile sensing platform.

Experimental Details

All data discussed in this chapter pertain to silicon cantilever whose dimensions are 35 μm width, 2 μm thick, and 350 μm in length. The typical experimental set up of HDR [2] as mentioned in previous studies is slightly modified with bubbler while sensing solvent vapors and artificial flavors (as shown in Fig. 5.1 (a)). The ac signal was swept until the lock-in amplifier detected the f_0 of the microcantilever (~ 18 kHz). All further experiments were carried out by (i) maintaining the microcantilever near its resonant frequency, and (ii) recording the changes in the cantilever response (change in the amplitude ΔA and phase signals $\Delta \Phi$) during a flow of gases or vapors of polar and nonpolar solvents (50 – 800 sccm). Gases such as, protium (H_2), deuterium (D_2), N_2O and CH_4 were brought into the vicinity of the resonating cantilever without passing through the bubbler in a start/stop gas flow mode with a manually controlled valve, shown in Fig. 5.1 (a) and (b). On the other hand, solvent vapors (water, hexane, benzene, methanol and isopropanol) and several beverages (coke, diet coke, cherry coke zero, grape water, orange juice and apple juice) were transported from the bubbler using air and hydrogen in the case of beverages as the carrier gas. In a separate study the sensing cantilever is functionalized to detect toxic gases like ammonia with 11-mercaptoundecanoic acid. We coated the cantilever with a solution of (11-MUA) using a micropipette [11] only on the side opposite to the counter electrode. In this case, the placement of counter electrode with respect to cantilever is just opposite to that of the typical HDR set up. Hence, counter electrode being at the top in the parallel geometry with the cantilever, the molecule that adsorbs on the coating should cause a decrease in the amplitude of the

signal due to the cantilever's bending away from the counter electrode. A 400 *ppm* concentration of ammonia in helium at room pressure was introduced into the sample chamber and three separate measurements were recorded each after five minutes. Whereas while detecting H_2S we used silicon microcantilever of the same dimensions and coated with gold only on the side facing the counter electrode. For this experiment we mixed the hydrogen sulphide gas with helium in the premixing chamber and diluted this mixture even more with helium to get down to *ppm* concentrations.

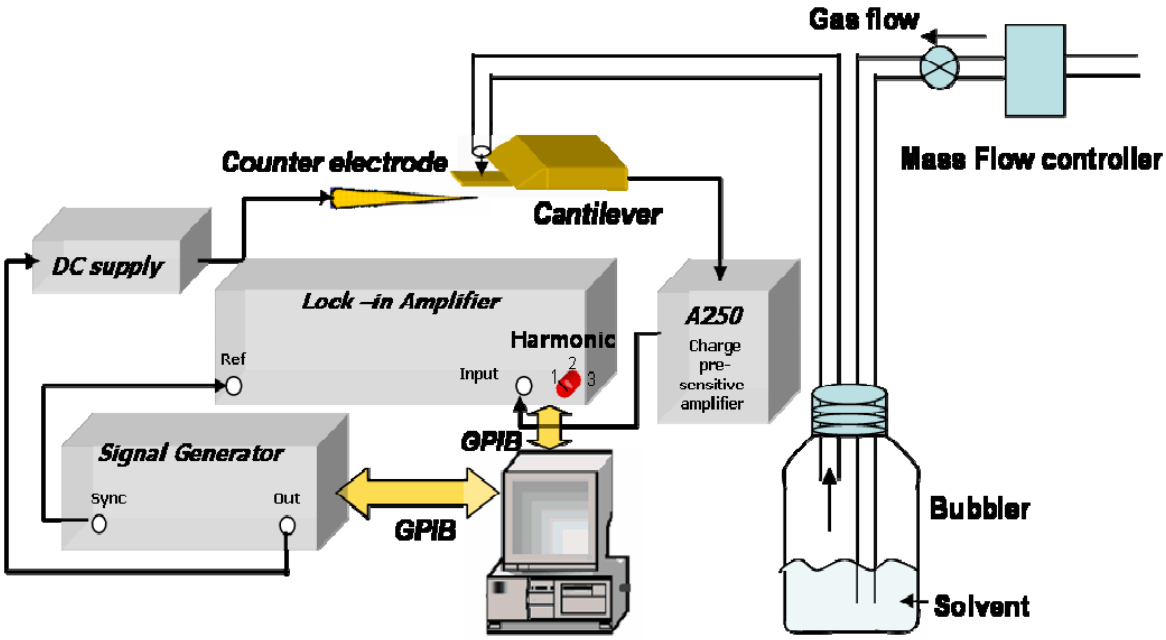

Figure 5.1 (a): Schematic diagram of the HDR system modified for sensing gases and solvents. The test gas is admitted in puffs without the solvent in the bubbler. For testing solvents, the carrier gas is bubbled through the solvent, and the changes in vibration of the cantilever are monitored.

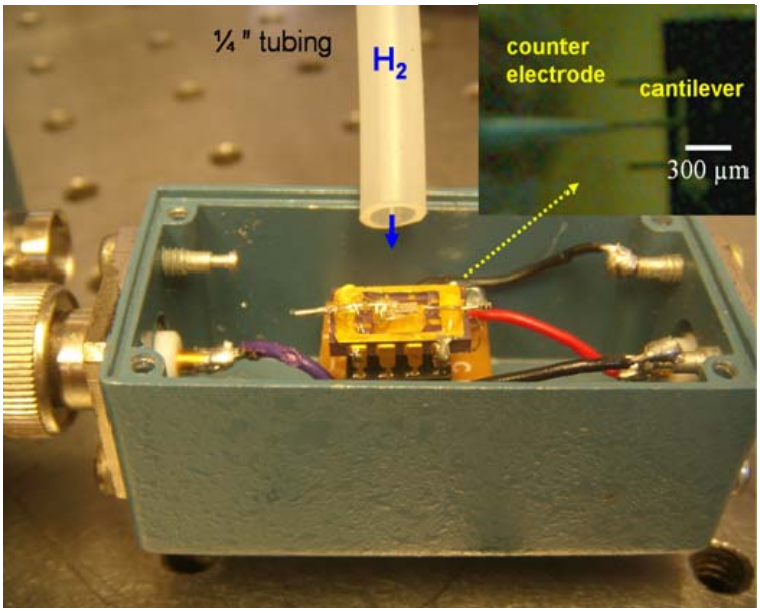

Figure 5.1 (b): Digital photograph of the experimental set up illustrating the chip carrier with cantilever and counter electrode and other electronic connections. The inset shows the optical image of cantilever - counter electrode alignment. The test or carrier gas is passed through ¼ ″ tygon tubing.

Results and Discussion

Sensing of gaseous species

The amplitude and phase signals for a cantilever resonating in air and exposed to 100 sccm of air bubbled through methanol, are compared in Fig. 5.2(a). The peak amplitude increased from 150 µV in ambient air to 170 µV in methanol. Likewise, the phase signal in air which resembles that of a damped SHO, is also sensitive to the

environment around the microcantilever and it decreased upon exposure to methanol. Once we determine f_0 using the phase and peak amplitude, we set the lock - in amplifier very close to f_0 to detect the ΔA and $\Delta \Phi$ induced by change in the environment in the vicinity of the cantilever. $\Delta \Phi$ is defined as $\Phi_A - \Phi_M$, where Φ_A and Φ_M correspond respectively to the magnitude of phase change in air and methanol (see Fig. 5.2(a)). Thus, ΔA and $\Delta \Phi$ signals can serve as sensitive indicators for the presence or absence of specific gases near the resonating cantilever. In Fig. 5.2(b), we plot ΔA and $\Delta \Phi$ for a microcantilever resonating in air and when intermittently exposed to 100 sccm of methanol. The amplitude increases and the phase decreases every time a pulse of the air with methanol is admitted. The response returns to the base line representing the amplitude and phase in ambient air promptly between puffs. The exposure time for each puff was about 30 seconds. While ΔA increased by ~ 6 μV, $\Delta \Phi$ decreased by ~ 5^0, indicating a slight decrease in f_0. The greater increase observed in peak amplitude (~ 20 μV) in Fig. 5.2(a) as compared to the increase in ΔA (~ 6 μV) seen in Fig. 5.2(b) can be attributed to the greater exposure time in the former case as the cantilever is continuously exposed to methanol vapors than the latter.

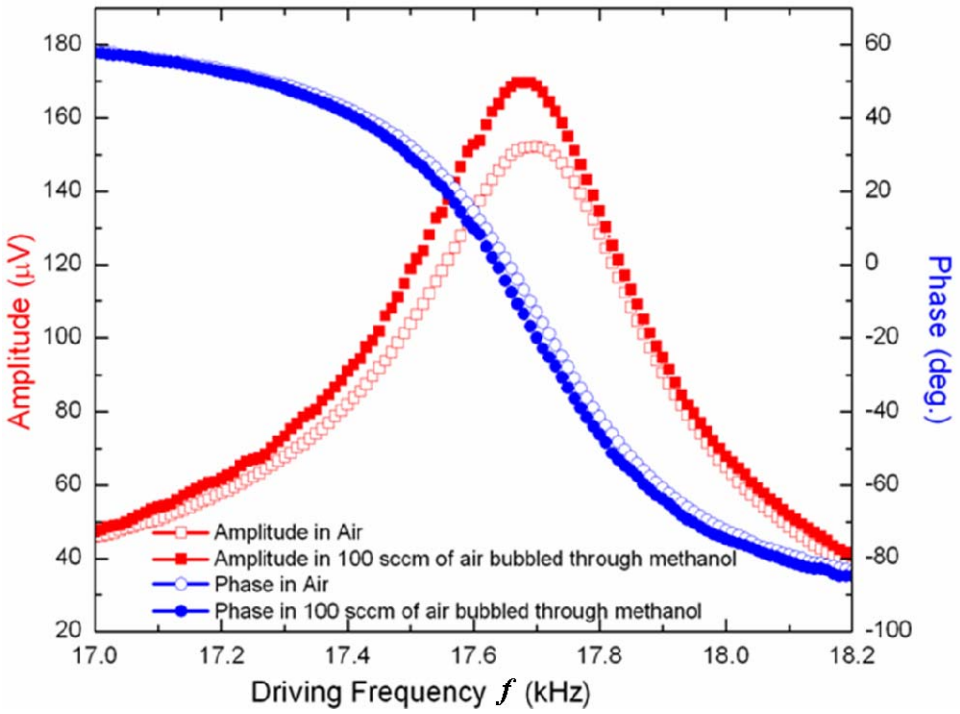

Figure 5.2(a): Response spectrum showing amplitude (solid red squares) and phase (solid blue circles) upon exposure to 100 sccm of air continuously bubbled through methanol. The reference spectrum showing amplitude (hollow red squares) and phase (hollow blue circles) in pure air is shown for comparison.

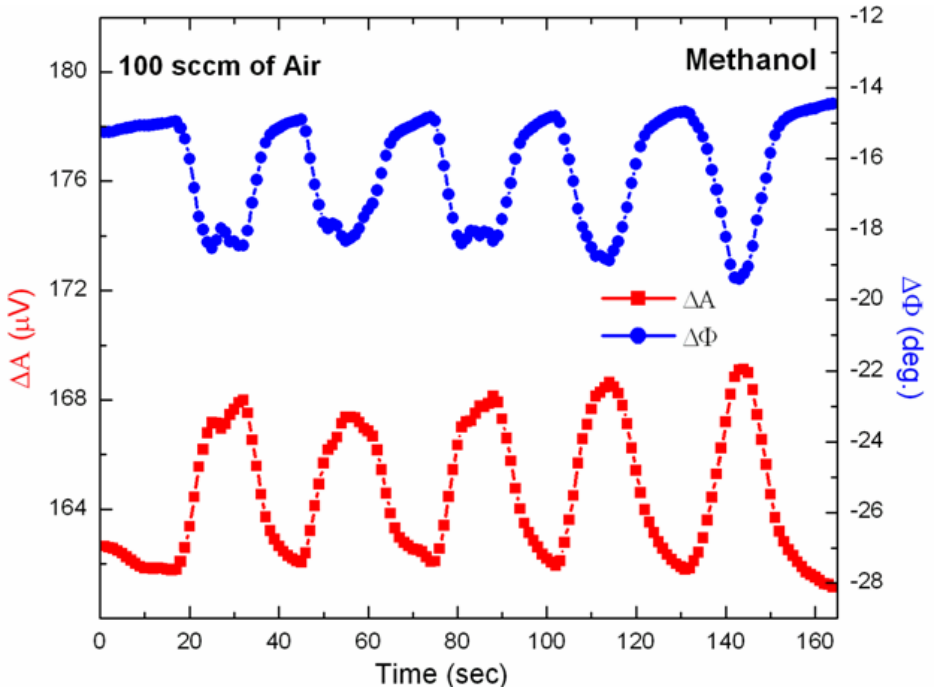

Figure 5.2(b): Response of the cantilever at the selected f_0 = 17.69 kHz showing the ΔA (solid red squares) and $\Delta \Phi$ (solid blue circles) upon exposure to puffs of 100 sccm of air bubbled through methanol.

In general, we observed that when the cantilever is exposed to the vapors of any solvent, the phase always decreases, implying that f_0 always decreases. *But the amplitude response is a function of both the change in maximum peak amplitude at resonance and the value of f_0, and can depend upon the selection of the frequency manually entered into the lock-in amplifier, which might be quite close to f_0 but not accurate. Since the derivative of the amplitude with respect to frequency at the selected frequency changes sign at the actual f_0, the amplitude response can go up or down for the same change in f_0*

depending upon whether the selected frequency is slightly lower or slightly higher than the actual f_0 (see Figs. 5.4(a) and 5.4(b)). But the derivative of the phase with respect to the selected f_0 is nearly constant near resonance. Thus the direction and magnitude of the phase change will always closely indicate the direction and magnitude of the change in f_0. This in turn is determined by the gas cantilever interactions, irrespective of the selection of f_0. Hence it is advisable not to depend on only ΔA but to take into account both ΔA and $\Delta \Phi$ while sensing gases and solvents. For example, in the case of methane, there is a large increase in amplitude but only a small change in phase and thus in f_0 (see Fig. 5.3(a)). The ΔA increased by ~ 14 μV and $\Delta \Phi$ increased by ~ 3^0 when exposed to 100 sccm of methane as seen in Fig. 5.3(b). But when exposed to 100 sccm of nitrous oxide, surprisingly the amplitude increased by ~ 10 μV but the phase and f_0 both decreased as shown in Fig. 5.4(a). Hence the $\Delta \Phi$ increase of $+3^0$ for methane as opposed to the $\Delta \Phi$ drop of -9^0 (Fig. 5.4(b)) for nitrous oxide shows that methane causes an increase in f_0 whereas nitrous oxide causes a decrease in f_0. This can be attributed to the fact that methane has a lower molecular mass and nitrous oxide has a higher molecular mass than air [3].

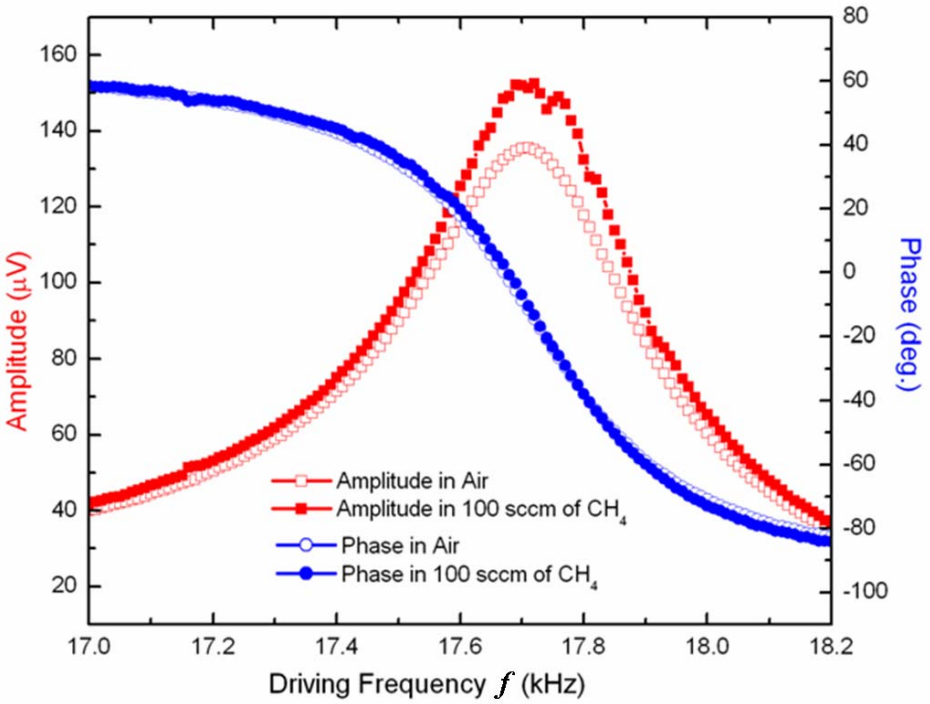

Figure 5.3(a): Response spectrum showing amplitude (solid red squares) and phase (solid blue circles) upon exposure to 100 sccm of methane (CH_4). The spectrum showing amplitude (hollow red squares) and phase (hollow blue circles) in air is shown for reference. ΔA is positive for all choices of selected f_0 with very small change in f_0 and a ~ 15% change in the peak amplitude. The corresponding ΔA and $\Delta \Phi$ plots are shown in Fig. 5.3(b).

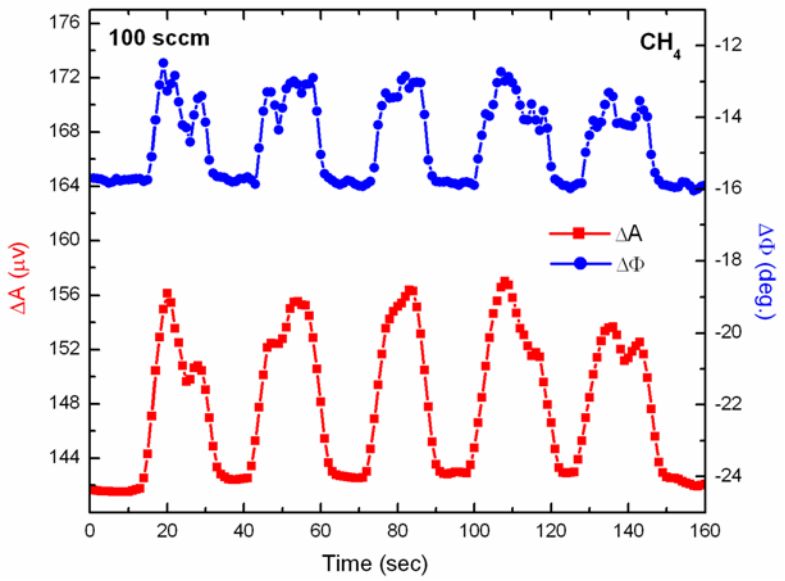

Figure 5.3(b): Response of the cantilever vibration to puffs of methane (CH_4) when the selected f_0 is 17.71 kHz, showing ΔA (solid red squares) and $\Delta \Phi$ (solid blue circles) upon exposure to 30 sec puffs of 100 sccm of methane (CH_4).

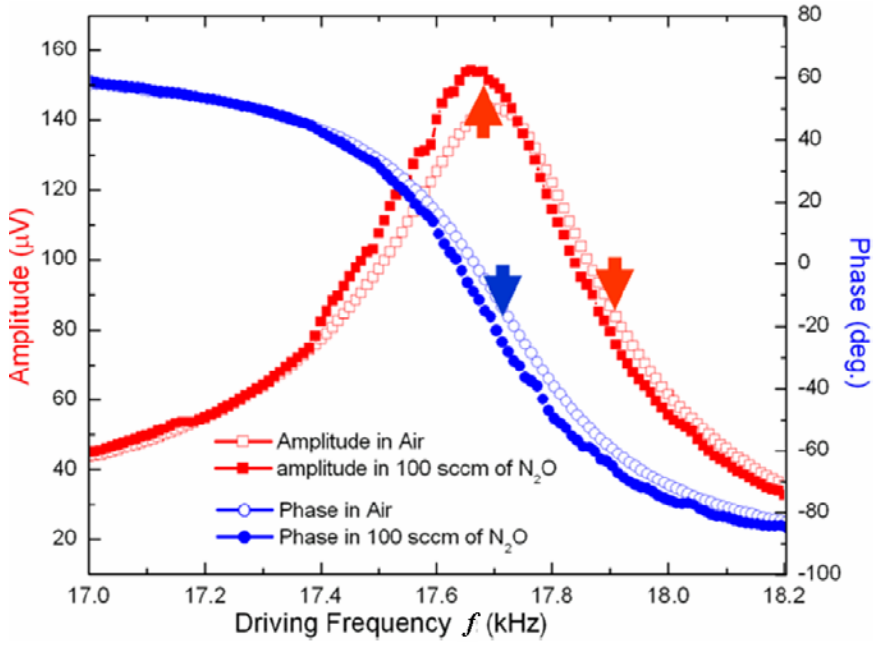

Figure 5.4(a): Response spectrum showing amplitude (solid red squares) and phase (solid blue circles) upon exposure to 100 sccm of nitrous oxide (N_2O). The spectrum showing amplitude (hollow red squares) and phase (hollow blue circles) in air is shown for the reference. With a 10% decrease in peak amplitude and a ~10^0 change in f_0, ΔA can be positive or negative depending on the f_0 selected. If the selected f_0 is 17.7 kHz, there will be increase in the amplitude and ΔA will be positive whereas if the selected f_0 is 17.9 kHz, there will be decrease in the amplitude and ΔA will be negative (as shown by the red arrows). But the $\Delta \Phi$ will always be negative as shown by the blue arrow irrespective of the selected f_0.

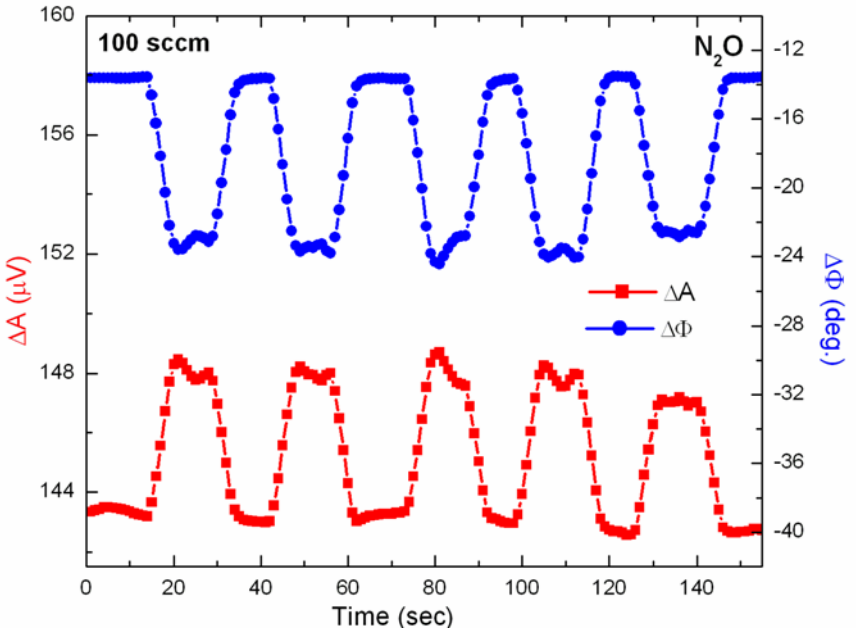

Figure 5.4(b): Response at a selected frequency of 17.7 kHz, showing ΔA (solid red squares) and $\Delta \Phi$ (solid blue circles) upon exposure to 100 sccm puffs of nitrous oxide (N_2O).

In Figs. 5.5(a) and 5.5(c), we plot the amplitude and phase responses for a microcantilever resonating in air and when intermittently exposed to 100 sccm of H_2 and D_2 gases, respectively. ΔA increases every time when exposed to H_2 as does $\Delta \Phi$. The increase in amplitude signal for D_2 is almost half of that for H_2, but there is not much change in the phase and f_0 for either of gas as seen in Figs. 5.5(a) and 5.5(c). It is very unlikely that the observed change in amplitude is due to physisorption of H_2 or D_2 molecules, or due to the influence of their dielectric properties. The observed increase in

amplitude can be due to the changes in the damping factor. At this pressure, the damping γ is inversely proportional to the square root of the atomic mass m [60], so that

$$\Delta\gamma/\gamma \approx -\tfrac{1}{2}\Delta m/m \qquad (6.1)$$

Approximating m for air as 30, Δm for protium is 28 and for deuterium is 26, implying that the effect on damping due to a small amount of H_2 added to air is about the same as D_2, consistent with our experiment. The ΔA and $\Delta \Phi$ exhibit similar trends in case of H_2 and D_2 such as, ΔA increased by ~ 8 μV and $\Delta \Phi$ increased by ~ 4^0 (Figs. 5.5(b) and 5.5(d)). Hence in order to differentiate between H_2 and D_2, we reduced the gap distance between the gas inlet and the microcantilever which might lead to more gas -cantilever interactions. As seen in Fig. 5.5(e), now even the ΔA for H_2 (m = 2) is roughly twice as that for D_2 (m = 4) which illustrates that we can successfully distinguish between the isotopes of hydrogen based on change in the mass. The inset in this figure helps to explain the kind of response observed during this particular experiment.

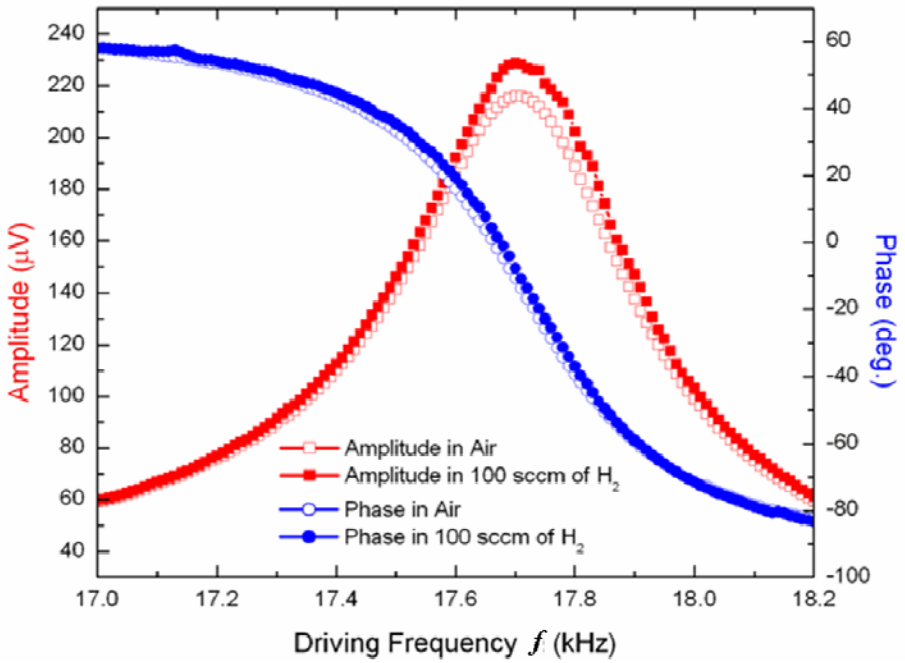

Figure 5.5(a): Response spectrum showing amplitude (solid red squares) and phase (solid blue circles) upon exposure to 100 sccm of protium (H_2). The spectrum showing amplitude (hollow red squares) and phase (hollow blue circles) in air is shown for reference.

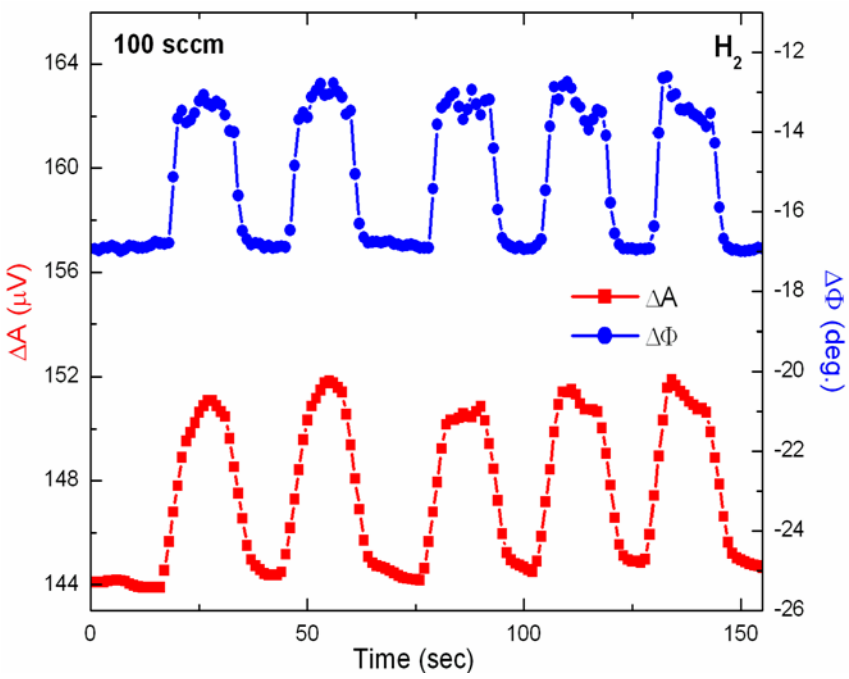

Figure 5.5(b): ΔA (solid red squares) and $\Delta \Phi$ (solid blue circles) upon exposure to puffs of 100 sccm of protium (H_2) at 17.71 kHz. ΔA increases every time when exposed to H_2 as does $\Delta \Phi$. Both return to the base lines representing the amplitude and phase in ambient air promptly.

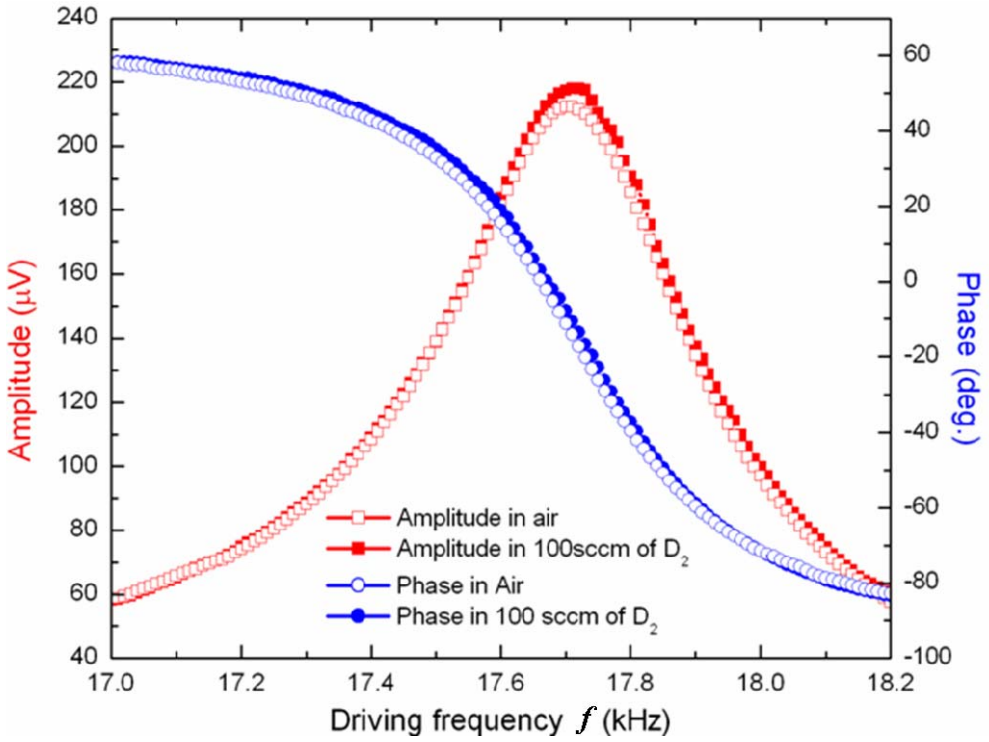

Figure 5.5(c): Response spectrum showing amplitude (solid red squares) and phase (solid blue circles) upon exposure to 100 sccm of deuterium (D_2). The spectrum showing amplitude (hollow red squares) and phase (hollow blue circles) in air is shown for the reference.

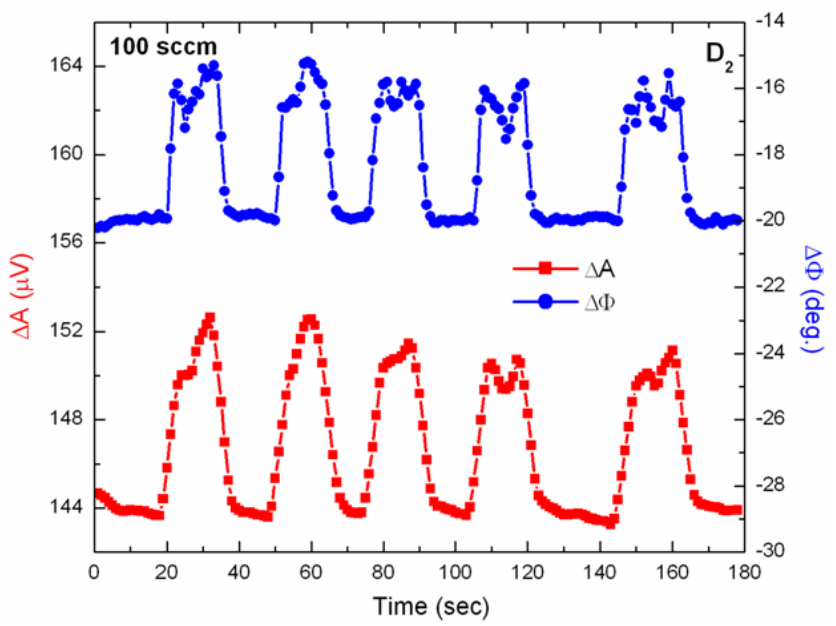

Figure 5.5(d): Response of ΔA (solid red squares) and $\Delta \Phi$ (solid blue circles) upon exposure to 100 sccm of deuterium (D_2) when the selected f_0 = 17.71 kHz. ΔA increases every time when exposed to D_2 with a concomitant increase in $\Delta \Phi$. The responses promptly return to the base lines representing the amplitude and phase in ambient air.

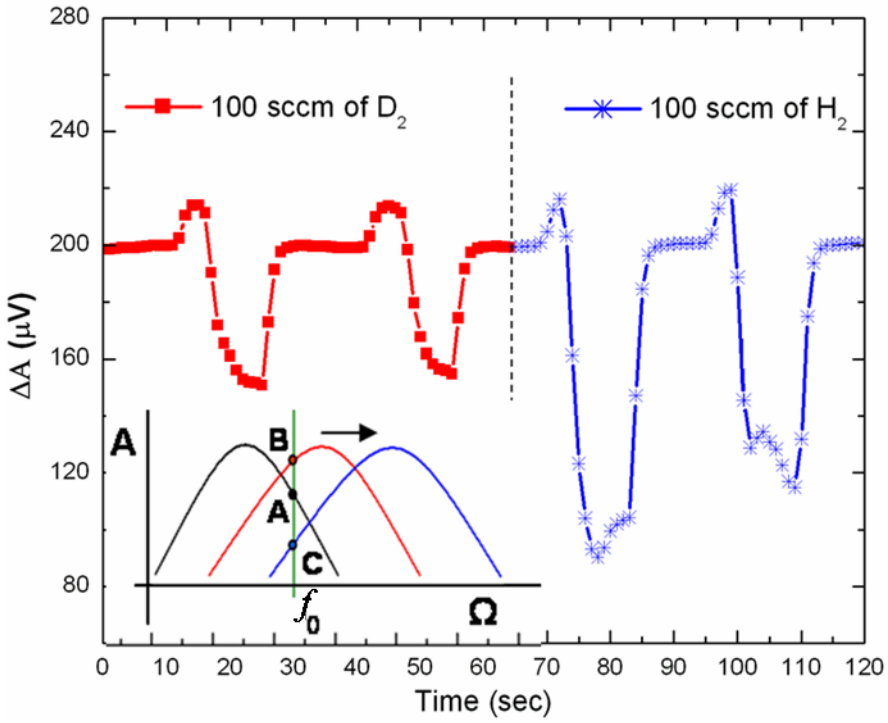

Figure 5.5(e): In a second experiment, ΔA upon exposure to puffs of 100 sccm of deuterium (D_2) (solid red squares) and protium (H_2) (blue crosses) at 17.6 kHz. Consider a response spectrum of a cantilever resonating in air (black peak shown in the inset), when it is exposed to H_2 /D_2 the f_0 increases as observed in previous figures (from black to red to blue peak with time). Hence, once exposed the amplitude will first go up from A (amplitude in air) to B and then amplitude will decrease to C with continued exposure at the selected f_0 (shown by green line). This explains the uncommon response *i.e.* ΔA first increasing and then decreasing every time when exposed to H_2 and D_2. ΔA for H_2 (m = 2) is roughly twice as that for D_2 (m = 4) which illustrates that we can differentiate between the isotopes of hydrogen based on change in the mass.

One would expect the amplitude to decrease in presence of nitrous oxide, since it has a higher '*m'* than air, but the opposite response is observed (Fig. 5.4(a)). It is difficult to predict the response of the cantilever when exposed to a particular gas/vapor as we can't quantify the exact amount of gas coming in contact with the cantilever. Thus the effect of the gas on the cantilever depends not only on the interaction of the gas with the cantilever, but also on our ability to deliver the gas to the cantilever. In fact, in our experimental set up we try to sense puffs of the test gas/vapor. Hence we propose that a gas lighter than air will go up easily without much interaction with the cantilever whereas a heavier gas will spend more time near the cantilever affecting its response to a greater extent. For example, ΔA increases by ~14 μV in presence of methane compared to ~ 8 μV for protium (Figs. 5.3(b) and 5.5(b)). Next we focus on the ΔA and $\Delta \Phi$ changes induced due to various concentrations of H_2. The response showed an increase in both ΔA and $\Delta \Phi$ which increased monotonically as the protium flow was increased from 50 sccm to 800 sccm (Fig. 5.6). The inset shows a typical amplitude response for the microcantilever when exposed to various amounts from 50 sccm to 800 sccm of protium in a start/stop gas flow mode. As expected, larger flow rates give larger changes. In chapter 3 [4] we have already shown that nearly pure protium, helium, air and argon gas atmospheres in a closed chamber have large effects on the damping, proportional to the inverse square root of the molecular mass of the gas. However, in this chapter the concentrations of the test gas are never large enough to allow this kind of discrimination.

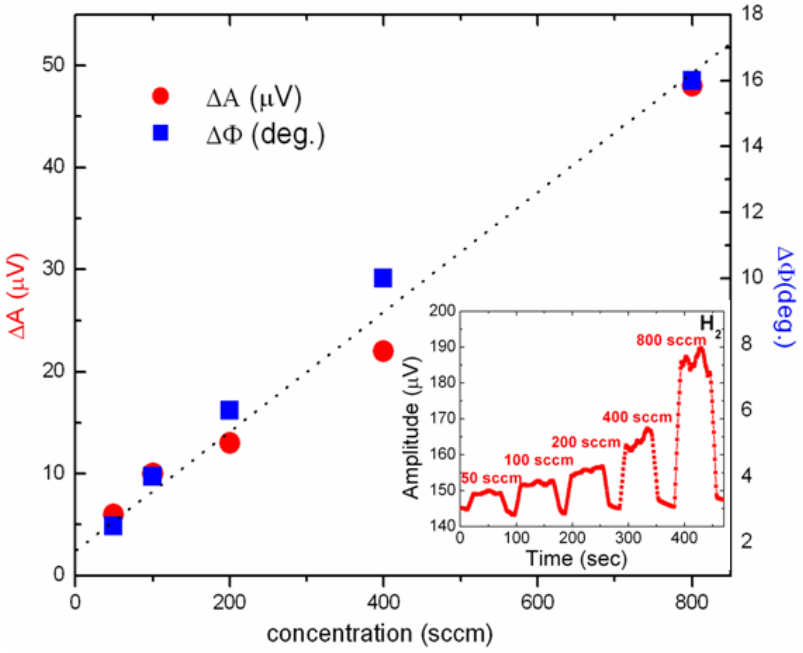

Figure 5.6: Dependence of ΔA and $\Delta \Phi$ (measured at the selected frequency f_0 = 17.71 kHz) on the amount concentration of protium (H_2) molecules present in the vicinity of the cantilever. The inset shows the response spectra upon exposure to puffs of increasing concentration of protium from 50 to 800 sccm. The base line represents the amplitude in ambient air.

Sensing of solvent vapors

The sensing of various polar and non polar solvents (n-hexane, benzene, methanol, iso-propanol and water) showed an increase in amplitude (Fig. 5.7(a)) and decrease in phase (not shown) upon exposure to 100 sccm of air bubbled through all these solvents. It shows that the normalized amplitude $\Delta A/A$ is highest for n-hexane and decreases uniformly with decreasing molecular mass of the solvent vapors under study.

The vapor pressures at room temperature for water, iso- propanol, methanol, benzene and n-hexane are 15, 44, 128, 100 and 127 mm of Hg respectively. Hence due to the lower vapor pressures for water and iso-propanol we get very small response in terms of the changes in amplitude for these two solvents as seen in Fig. 5.7(a). The peculiar trends observed in the normalized amplitude responses of these solvents are correlated to their different dependences on mass, dielectric constant and polarity index (see Fig. 5.7(b)). In general, the normalized amplitude showed a decreasing trend with increase in polarity index, dielectric constant and inverse of mass. Although it was not possible to determine exactly which property determined the result, the previous study would favor the molecular mass of the solvent as the dominant characteristic. As opposed to solvent vapors, while sensing gases, the normalized amplitude decreased with increase in molecular mass of the gas as expected except for methane for reasons we do not understand (as seen in Fig. 5.8).

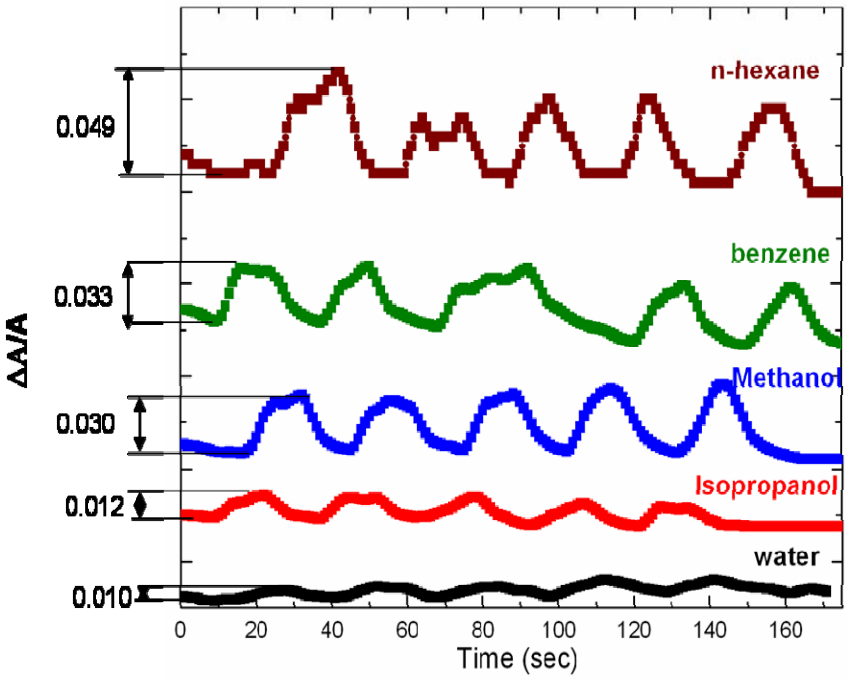

Figure 5.7(a): Normalized amplitude changes upon exposure of the cantilever vibrating near f_0 to 100 sccm of air bubbled through water, iso-propanol, methanol, benzene and *n*-hexane. The numbers on the left axis indicate ΔA/A for each individual solvent vapor.

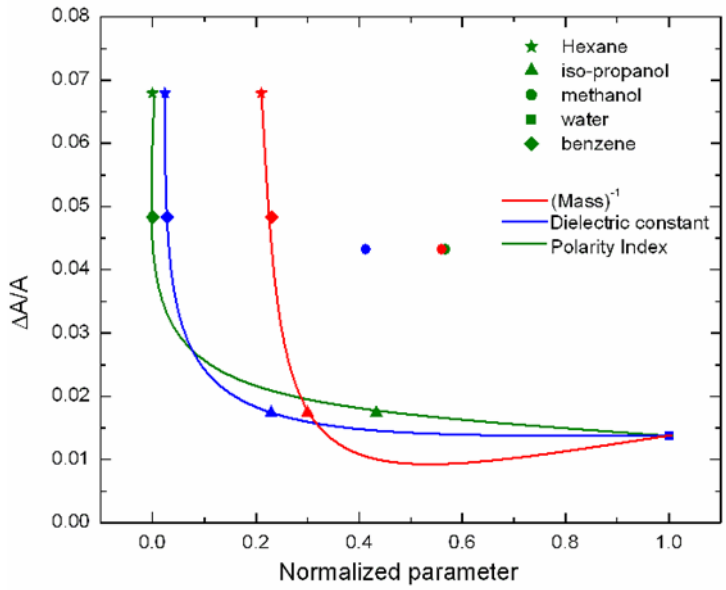

Figure 5.7(b): The normalized amplitude ΔA/A for the solvents methanol, water, iso-propanol, benzene and *n*-hexane plotted as a function of three normalized parameters: the inverse of mass, dielectric constant and polarity index. The normalization of each parameter consisted of dividing the value of that parameter for each solvent by the maximum value of the parameter in this set of solvents. The lines are only guides to the eye. Methanol may interact differently than the other solvents.

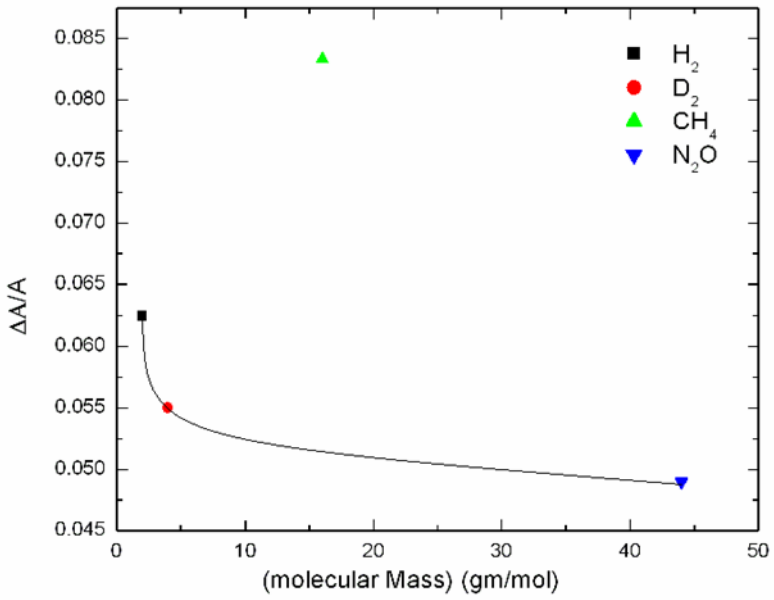

Figure 5.8: Dependence of normalized amplitude on the molecular mass of the gas surrounding the cantilever upon exposure to 100 sccm of protium, deuterium, methane and nitrous oxide. The line is only guide to the eye.

Sensing of different flavors

We have also sensed different natural and artificial flavors such as apple juice, orange juice, grape water, Diet Coca Cola™, Cherry Coca Cola Zero™ and regular Coca Cola™. The response spectra after exposing to 100 sccm of H_2 gas bubbled through these beverages showed that the amplitudes and phases went up (Figs. 5.9 (a) and (b)). We repeated these measurements and each time similar trends were observed. The carbonated drinks (artificial flavors) showed a stronger impact than the natural flavors. Among the natural flavors the highest response was observed for the apple juice whereas the lowest

one was the orange juice. The successful separation among the Diet Coca Cola™, regular Coca Cola™ and Cherry Coca Cola Zero™ was an interesting outcome of our highly sensitive non-functionized microcantilever sensor. It displayed characteristic responses for these natural and artificial flavors.

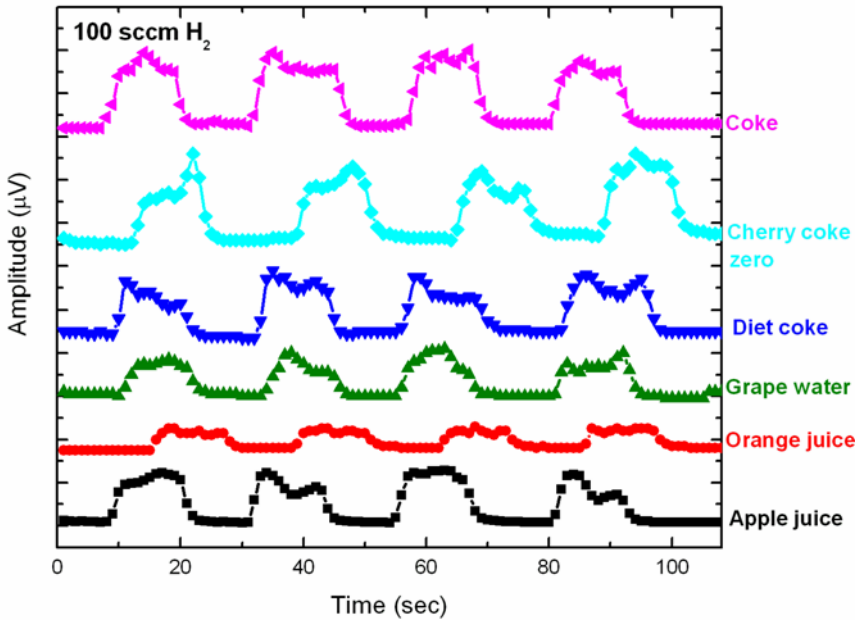

Figure 5.9 (a): Response spectra comparing amplitudes upon exposure to 100 sccm of hydrogen bubbled through different flavors such as grape water, orange juice, Diet Coca Cola™, regular Coca Cola™, Cherry Coca Cola Zero™ and apple juice. The baseline represents the amplitude in ambient air.

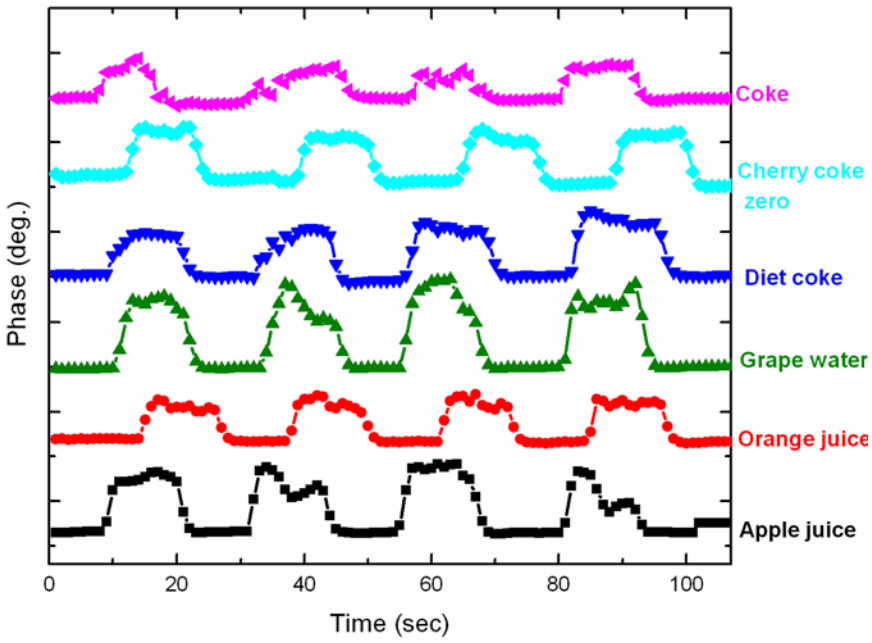

Figure 5.9 (b): Response spectra comparing phases upon exposure to 100 sccm of hydrogen bubbled through different flavors such as grape water, orange juice, Diet Coca Cola™, regular Coca Cola™, Cherry Coca Cola Zero™ and apple juice. The base line represents the phase in ambient air.

Sensing of toxic gases

The silicon microcantilever of the same dimension was coated with 11-mercaptoundecanoic acid in order to detect toxic ammonia gas. Ammonia can be detected as it forms reversible hydrogen bonds with the acidic tail of the 11-MUA [11]. Figure 5.10 (a) compares the resonant frequency of the cantilever before and after it was functionalized. It shows a distinct upshift in the resonant frequency from 21.8 kHz to

22.7 kHz, which could be attributed to the stiffening of the cantilever after coating and the amplitude, was damped. Under ideal conditions (immersion of the cantilever in 11-MUA solution for over 10 hours), the sulfur end of the molecules will bind to the gold surface, and the molecules self-assemble perpendicular to it. With our present configuration of chip, immersion of the cantilever was not possible, and so the 11-MUA solution was simply placed dropwise onto it and allowed to evaporate. Though the sulfur-gold bonds formed quickly within this time, a well-organized monolayer did not have time to self-assemble before evaporation. Thus, the molecular organization of the cantilever coating is not uniform, resulting in fewer binding sites for the ammonia per unit area. Three separate measurements recorded after exposure to 400 *ppm* of ammonia in helium show 7.0, 7.3, and 10.3 % decrease in the signal amplitude, respectively (Fig. 5.10 (b)), demonstrating the reproducible detection of the binding of ammonia. Between measurements, the chamber was flushed with helium, and the signal amplitude increased to its former intensity, showing the reversible nature of the ammonia binding. While both the detection limit and response are less than ideal, this rough experiment demonstrates the first proof of principle of sensing a gas via electrostatic detection of cantilever resonance using HDR.

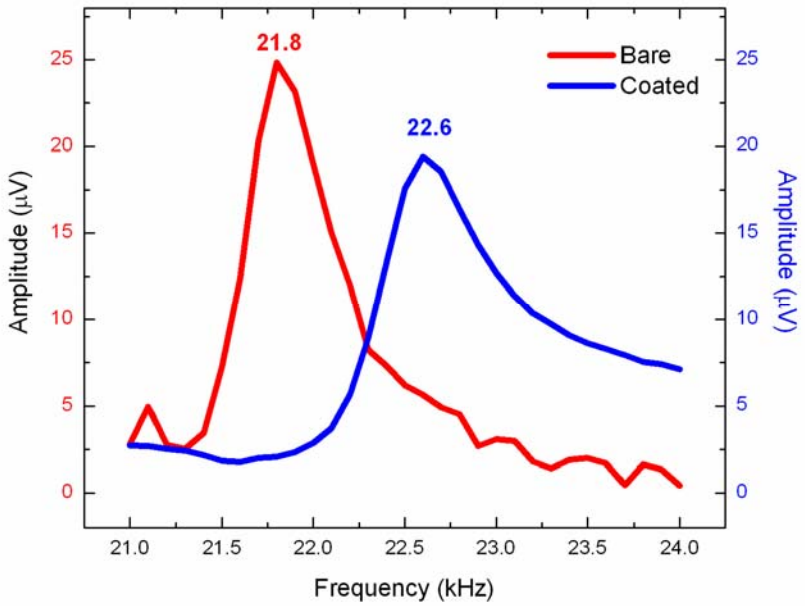

Figure 5.10 (a): Resonance spectra showing upshift in the resonant frequency (blue) after functionalizing the cantilever with 11-MUA. The red spectrum shows the resonance frequency of uncoated microcantilever.

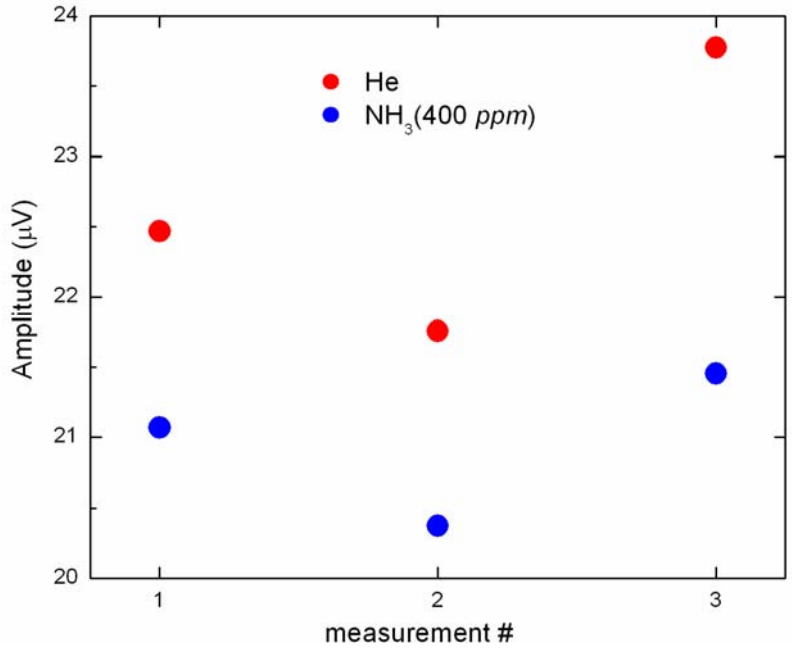

Figure 5.10 (b): Three separate measurements showing the change in amplitude when exposed to 400 *ppm* of ammonia in helium (solid blue circles). The amplitude in pure helium environment (solid red circles) dropped by 7.0, 7.3, and 10.3 % respectively, in presence of ammonia in these measurements.

When exposed to various amounts of H_2S, we noticed a monotonic rise in the size of signal with increase in the concentration of hydrogen sulphide gas in helium from 0 to 100 *ppm* in the chamber (Fig. 5.11). The sulphur-gold affinity causes the cantilever to bend towards the counter electrode leading to greater signal with higher concentrations. There is not only change in resonant frequency as we go from pure helium to helium mixed with hydrogen sulphide but we also observed the change in the amplitude of signal. The complete saturation of gold coated cantilever with sulphur led to the highest

amplitude and increase in the resonant frequency. The validity of this behavior is checked by repeating the experiment with the same cantilever.

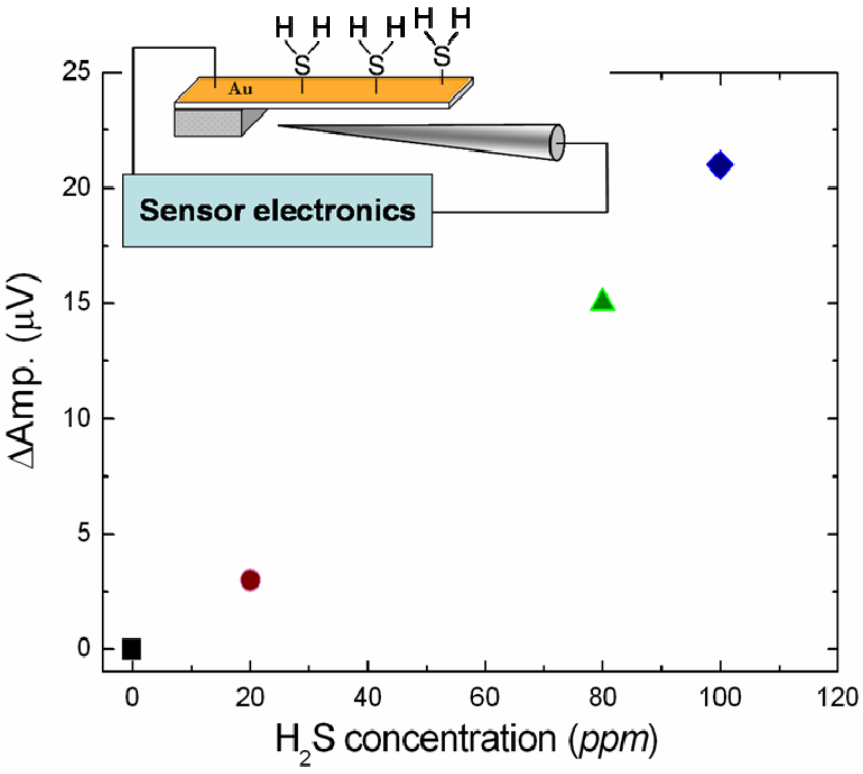

Figure 5.11: The ΔA signal increases monotonically with the increase in the concentration of hydrogen sulphide gas in helium from 0 to 100 *ppm* in the chamber. A concomitant downshift in f_0 from 18.23 kHz (at 0 *ppm*) to 18.10 kHz (at 100 *ppm*) was observed.

Conclusions

We have demonstrated qualitative sensing of different gases and solvent vapors. This sensor platform features a reasonable selectivity and rapid response. It is clear from

the above experiments, that any chemical specie carries a particular 'fingerprint' while using HDR based on the criteria that involve 1) the static (dielectric effects) and dynamic capacitance between the cantilever and counter electrode, 2) the detection of trace amounts of adsorbed molecules through a shift in the resonant frequency, 3) variations in the environment which affect the mechanical damping of the microcantilever. At present the exact mechanisms of these responses are not fully understood and further investigation is in progress. Most of these measurements are promising approaches to a completely new class of easy to use miniaturized sensor systems. The functionalized sensor has potential applications in the area of selective detection of multielement/ multicomponent systems. Further development would involve optimizing the geometry and configuration of the cantilever and counter electrode, functionalizing the cantilever to suit the gas(es) to be detected, and improving the electronics.

The functionalized cantilevers showed different responses when exposed to ammonia and hydrogen sulphide. This may be due to: (i) Our method depends on the oscillator non-linearities. A small change in the gap distance can have a large effect on the non-linearities and hence the amplitude at the 2nd harmonic which we measure. (ii) The energy involved in a cantilever's motion is equal to ½ kA^2 (= ½ $mf_0^2A^2$) in SHO which remains constant. Hence, if the resonant frequency increases due to stiffening of cantilever as in case of ammonia, it decreases the amplitude. For hydrogen sulphide, the amplitude went up causing the resonant frequency to downshift as f_0A is constant.

CHAPTER SIX

DETERMINATION OF CARBON NANOTUBE DENSITY BY GRADIENT SEDIMENTATION

Introduction

As discussed earlier, in chapters 2 and 3 HDR is a versatile technique and it can used to determine the mechanical properties such as Young's modulus of silicon microcantilever using equation (2.27),

$$E = \frac{\rho A (f_i)^2 l^4}{(\beta_i)^2 I_y} \tag{2.27}$$

Hence, if we can measure the resonant frequency (f_0) of micro- or nanocantilevers using HDR and determine their densities (ρ), then we can calculate their respective Young's modulus. In order to demonstrate the feasibility of using HDR at the nanoscale, we have driven individual multi-walled carbon nanotube (MWNT) into resonance and determined its Young's modulus. However, MWNTs grow with a dominant inner/outer diameters and length, depending on the growth parameters used in the experiment. Therefore, accurate knowledge of the MWNT density is essential in the determination of its Young modulus. In this chapter, a gradient sedimentation technique[89] is described which provides densities for MWNTs and single walled carbon nanotubes (SWNTs) that agree very well with respected computed densities.

Carbon nanotubes (CNTs) have revolutionized the scientific community with fundamentally interesting properties and potential for numerous applications owing to their unique electrical, optical, thermal, and mechanical properties [90-93]. Surprisingly,

a fundamental physical property, viz. the density of CNTs, has received relatively little attention. Since density is directly associated with the intrinsic structure of the CNT, it can be used to quantify its purity after separation from the as-prepared soot. Moreover, since the presence of defects alters the structure of a CNT, the density may also serve as a measure of the quality of the CNTs.

A SWNT can be formed by folding a single graphene sheet into a seamless tube with a diameter of ~1 nm. The most important synthesize techniques for SWNTs are pulsed laser vaporization, chemical vapor deposition and electric arc discharge. Depending upon how the grapheme sheet is rolled into a SWNT, there are three classes of SWNTs with different chiralities, viz. armchair, zigzag, and chiral nanotubes [90]. The unit cell of an individual SWNT is dictated by its chirality leading to different lattice parameters and densities. Simulations by Gao et al. [94] verified this dependence showing that the (10,10) armchair tubes possess a lattice parameter of $a_{(10,10)}$ = 16.78 Å and a density of $\rho_{(10,10)}$ = 1.33 g/cm^3. The corresponding values for a (17,0) zigzag tube are $a_{(17,0)}$ = 16.52 Å and $\rho_{(17,0)}$ = 1.34 g/cm^3, and $a_{(12,6)}$ = 16.52 Å and $\rho_{(12,6)}$ = 1.40 g/cm^3 for a chiral (12,6) tube. A MWNT is formed when several SWNTs with increasing tube diameters self-assemble concentrically into a single carbon nanotube [90]. For a typical MWNT with an outer diameter of 8-15 nm and an inside diameter of 3-5 nm, the density is reported to be around 2.1 g/cm^3 [95].

The density gradient sedimentation method is widely used for measuring the densities or molecular weights of macromolecules, as well as for separating colloids and minerals. In this method, a sodium metatungstate-water solution is centrifuged to form a

density gradient in the centrifugal field. The macromolecule sediments to a position in the gradient where its density closely matches with the density of the solution. This technique can separate macromolecules with remarkably small differences in density. With this technique, in a standard centrifuge cell at 40 000 rpm using cesium chloride gradient solution, a density difference of 0.014 g/cm^3 in macromolecules results in a well defined band spanning ~0.5 mm which strongly emphasizes its high resolution capability [89]. For this study, the sodium metatungstate ($Na_6[H_2W_{12}O_{40}]$, abbreviated as NamW) solution was selected to determine the densities of CNTs because of NamW's high density (3.12 g/cm^3 at 25 °C), low viscosity at high concentration, and high solubility in water [89]. For samples available in small amounts or low concentrations, this technique is more convenient and accurate than other conventional techniques [96].

Experimental Procedure

Gradient Centrifugation: NamW-water solution was prepared by adding NamW (2.82 g/mL, Acros Organics) to the distilled water at a volume ratio of 7: 9 (NamW/H_2O) [97]. CNTs (~ 0.5 mg) were added to 3 mL of NamW-water solution in a Beckman polyallomer centrifuge tube (11mm $\times$ 60 mm). Centrifugation was performed with a Beckman SW56 rotor at 23 000 rpm and 20 °C. After 60 hr of centrifugation, well-defined bands were formed and their distances from the meniscus were measured. The gradients were fractionated in 200-μL fractions, and each fraction was weighed on a Mettler H20T balance.

Carbon Nanotube Samples: The pristine SWNT (p-SWNT) bundles and isolated SWNTs (iso-SWNT) used in this study were synthesized by the electric arc discharge and chemical vapor deposition (CVD) methods, respectively [1]. The ultrasonic agitation of pristine SWNTs in a 3:1 mixture of concentrated H_2SO_4 and HNO_3 resulted into acid-treated SWNTs (acid-SWNT). This acid treatment makes SWNTs soluble in water with abundant carboxyl end-groups formed at defect sites and terminals [98]. MWNTs were synthesized using two methods: (i) a thermal decomposition of a ferrocene-xylene mixture [99] and (ii) by striking an electrical arc discharge between two graphite electrodes in an inert Ar atmosphere [100]. All these CNTs samples were characterized after sedimentation by transmission electron microscopy (TEM) and micro-Raman spectroscopy. Fractionated CNT samples were stained with uranyl acetate and deposited on 300-mesh copper grids for TEM characterization with a Hitachi 7600 microscope. The micro-Raman data for SWNTs was gathered using a TRIAX 550 single-grating spectrometer (groove density 1200 grooves/mm) equipped with a liquid nitrogen-cooled charge-coupled device (CCD). An Ar ion laser with a wavelength of 514.5 nm was used to excite Raman scattering from the CNTs using 50 × objective of a Leica microscope.

Results and discussion

After centrifugation, the well-defined bands formed corresponding to each of the CNT structures are shown in Figure 6.1. The different structures sedimented at different levels in gradients prepared under identical conditions (see Fig. 6.1).

Micro-Raman Spectroscopy

The various bands seen in Fig.6.1 were confirmed to contain MWNTs, p-SWNT bundles, or iso-SWNTs using micro-Raman spectroscopy as demonstrated in Figure 6.2. The micro-Raman spectrum of iso-SWNTs (shown in green), show the signature radial breathing modes (RBM) at 157 and 266 cm^{-1} implying SWNT diameters of 1.58 and 0.93 nm respectively at room temperature. The nanotube diameters were estimated using the empirical relation,

$$d_t = 248/\omega_{RBM},$$

where d_t and ω_{RBM} refer to the tube diameter and the RBM mode angular frequency [101]. The peaks present at ~520 and ~950 cm^{-1} correspond to the Raman modes of the Si substrate The tangential (G) band is observed at 1588 cm^{-1} with disorder induced band (D-band) of negligible intensity [90]. Lorentzian lineshape of the RBM in the Raman spectra suggested that the SWNTs are isolated. In the Raman spectrum of arc-prepared MWNTs, a pronounced D-band is also observed at 1357 cm^{-1} in addition to the G-band at 1581 cm^{-1}. However, p-SWNT bundles show the RBM and G-bands at 170 and 1588 cm^{-1}, respectively. The lineshape of the G-band in each spectrum of pristine SWNTs hints that the 514.5 nm excitation couples to isolated semiconducting SWNTs [102].

Figure 6.3 shows the density profile along the length of a NamW gradient. The density data, obtained by weighing each gradient fraction of 200 μL, show the linear dependence on the distance of the gradients from the meniscus. The solid circle on the straight line indicates the position of the sharp band formed by the p-SWNT bundles (see

Figure 6.1b). The density corresponding to this position from the meniscus in the gradient is 1.90 g/cm^3. The densities of other forms of SWNTs and MWNTs were calculated using a similar approach and are presented in Table 6.1. The experimental deviation was calculated for the enlisted densities in Table 6. 1 using three independent experiments as,

$$\sqrt{\sum (\rho - \bar{\rho})^2 / (n-1)}$$

where ρ is the density measured for each experiment, $\bar{\rho}$ is the mean density, and $n = 3$.

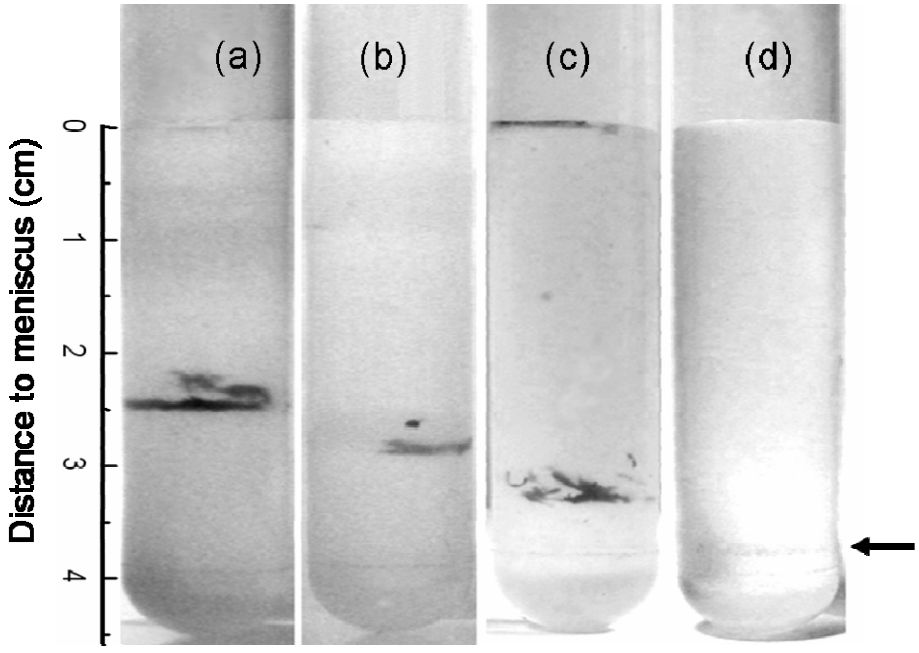

Figure 6.1: Various structures of CNTs, including (a) acid-SWNT, (b) p-SWNT, (c) MWNT and (d) iso-SWNT, form bands at different levels in gradients prepared and run identically.

	acid-SWNT	p-SWNT	iso-SWNT	MWNT (CVD)	MWNT (Arc Discharge)
density (g/cm^3)	1.74 ± 0.04	1.87 ± 0.03	2.13 ± 0.04	2.09 ± 0.02	2.11 ± 0.03

Table 6.1: The measured densities of various structures of CNTs. The data represent means of three independent experiments and the numbers following "±" are standard deviation.

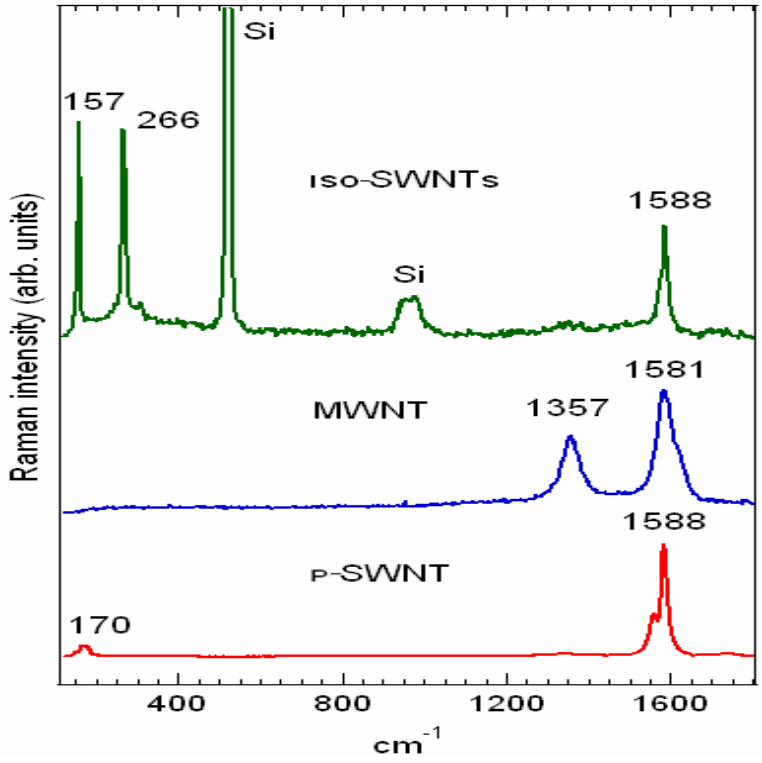

Figure 6.2: Raman characterization of MWNTs, p-SWNTs and iso-SWNTs. The two peaks in the spectrum of iso-SWNTs marked by "Si" were from silicon substrate.

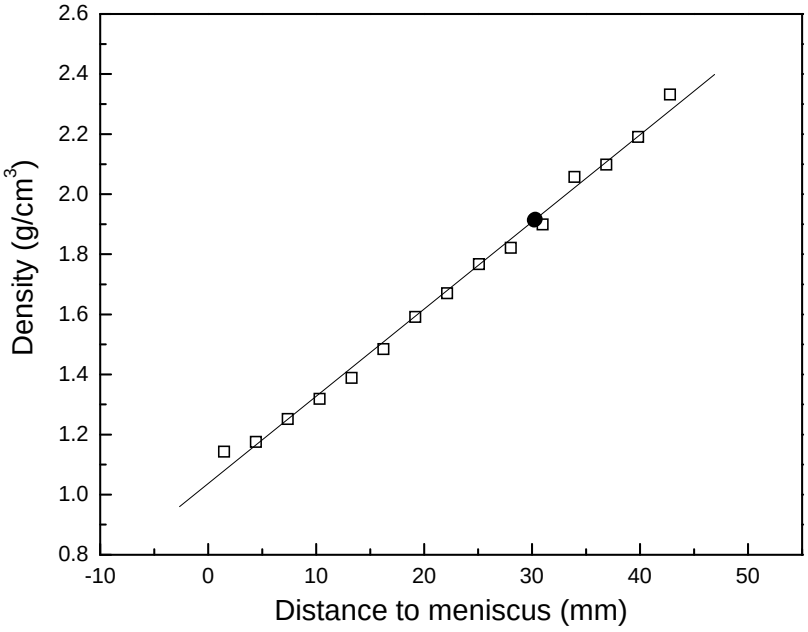

Figure 6.3: The density profile along the length of a gradient obtained from p-SWNTs. The density data, obtained by weighing each gradient fraction of 200 μL, fit a straight line $y = 0.2903x + 1.0371$, where x is the distance from the meniscus to a particular fraction and y is its density. The solid circle on the trendline of the density gradient indicates the position of a sharp band corresponding to p-SWNTs. The density of this point in the gradient is 1.90 g/cm^3.

Transmission Electron Microscopy (TEM)

Extensive TEM studies were conducted to determine (i) diameter distribution of individual SWNTs within a p-SWNT bundle, (ii) distribution of p-SWNT bundle diameters, and (iii) distribution of MWNT diameters (Figure 6.4). From Gaussian analysis of the histograms shown in Figure 6.4, the mean diameters of individual tubes in

p-SWNT bundles, p-SWNT bundles, and of MWNTs were determined to be 1.44 ± 0.04, 8.00 ± 0.11, and 49.26 ± 2.16 nm, respectively.

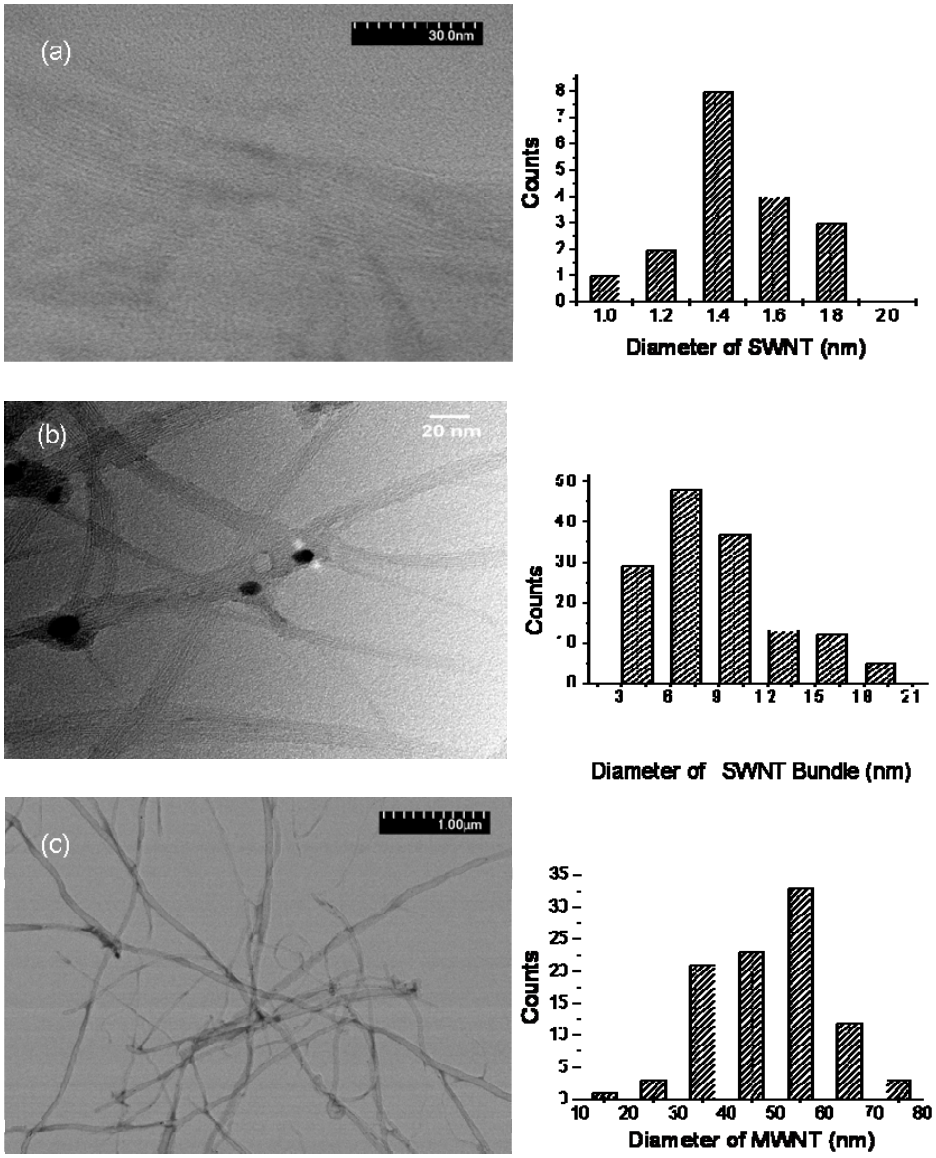

Figure 6.4: TEM images obtained from (a) SWNTs, (b) SWNT bundles and (c) MWNTs. Diameter histograms of each structure were acquired by TEM. From Gaussian analysis of the histograms, the mean diameters of individual p-SWNTs, p-SWNT bundles, and MWNTs were determined to be 1.44 ± 0.04, 8 ± 0.11 and 49.26 ± 2.16 nm, respectively.

Theoretical Model

The experimentally determined diameters were used in the model described further to estimate the densities of p-SWNT bundles and MWNTs. The density of an individual SWNT was computed by considering it as a rolled honeycomb sheet of length L and diameter D_{SWNT}. Density ρ_{SWNT} is given as

$$\rho_{SWNT} = \frac{m}{V} = \frac{N_C m_C}{L\pi \frac{D_{SWNT}^2}{4}} = \frac{\pi \frac{D_{SWNT}}{D_2} \frac{L}{D_2}}{L\pi \frac{D_{SWNT}^2}{4}} Zu = \frac{4Zu}{D_{SWNT} D_2^2} \tag{6.1}$$

where N_c and m_c correspond to the number and mass of the carbon atoms. In equation (6.1), D_2 = 2.83 Å is the longest distance between carbon atoms in a single hexagonal lattice [90], Z is the atomic mass for carbon atom and u is the atomic mass unit (1.6605×10^{-27} kg). Following a similar rationale the density of a SWNT bundle can be written as:

$$\rho_{Bundle} = \frac{m}{V} = \frac{n_{SWNT} N_C m_C}{L\pi \frac{D_{Bundle}^2}{4}} = \frac{n_{SWNT}\pi \frac{D_{SWNT}}{D_2} \frac{L}{D_2}}{L\pi \frac{D_{Bundle}^2}{4}} Zu = \frac{4 n_{SWNT} D_{SWNT} Zu}{D_{Bundle}^2 D_2^2} \tag{6.2}$$

where D_{Bundle} is the bundle diameter which can be expressed as:

$$D_{Bundle} = D_{SWNT}\left(2n_{tier} + 1\right) + 2n_{tier} D_{il} \tag{6.3}$$

n_{SWNT} = 1, 7, 19, 37, 61 is the number of SWNTs in each tier and n_{tier} is the number of tiers for each bundle, and D_{il} = 3.38 Å is interlayer spacing shown in Fig. 6.5(a) [90].

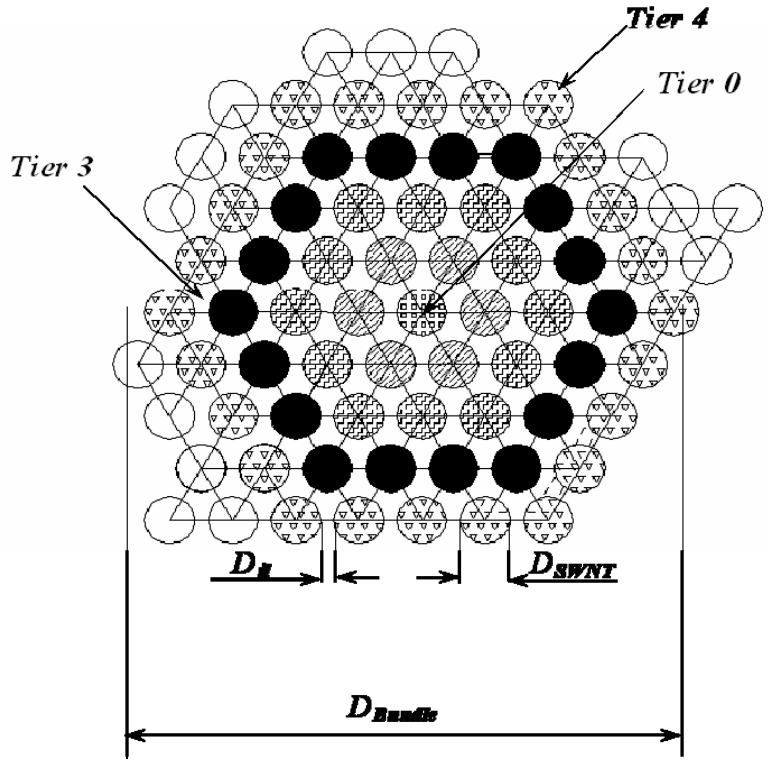

Figure 6.5(a). The density of SWNT bundles was computed based on the arrangement of SWNTs in tiers.

As discussed in Fig. 6.4, the samples used in this study exhibit a Gaussian distribution in diameters for individual and bundled SWNTs. Therefore, we express the $n_{SWNT}D_{SWNT}$ term in equation (6.2) for a bundled SWNT as

$$n_{SWNT}D_{SWNT} = \sum_{i=1}^{n} A_i D_i e^{-\frac{(D_i - D_o)^2}{2\sigma^2}} \tag{6.4}$$

where A_i, D_i, D_o, and σ are obtained from a Gaussian fit to the experimental diameter distribution of individual SWNT within a bundle (see Fig. 6.4) [102]. A_i, D_i, D_o and σ correspond to the weighting factor, binning diameter, median diameter and the standard deviation, respectively. Substituting equations (6.3) and (6.4) in equation (6.2) gives

$$\rho_{Bundle} = \frac{4Zu}{D_{Bundle}^2 D_2^2} \sum_{i=1}^{n} A_i D_i e^{-\frac{(D_i - D_o)^2}{2\sigma^2}} \tag{6.5}$$

It is a well known fact that residual catalysts are present in pristine SWNTs. Next we discuss our model calculations taking into account the presence of catalyst particles. We consider the measured density of SWNT bundles ($\rho_{measured}$) in terms of the density and volume of bundled SWNTs and catalyst particles as follows:

$$\rho_{measured} = \frac{m}{V} = \frac{m_{Carbon} + m_{Catalyst}}{V_{Bundle}} = \frac{m_{Carbon} + m_{Catalyst}}{\frac{m_{Carbon}}{\rho_{Bundle}}} = \rho_{Bundle} \frac{m_{Carbon} + m_{Catalyst}}{m_{Carbon}} = \rho_{Bundle} \left(1 + \frac{m_{Catalyst}}{m_{Carbon}}\right) \tag{6.6}$$

In equation (6.6), we neglect the volume of the catalyst in comparison to the volume of the SWNT bundle. The quantity $m_{Catalyst} / m_{Carbon}$ is determined as 0.26 from the atomic composition of the anode (C = 95 at.% : Ni = 4 at.% : Y = 1 at. %). Using equation (6.5), the densities of SWNT bundles with sizes ranging from 1 to 15 nm were calculated and plotted (dashed line passing through solid triangles) in Fig. 6.5(b). When residual catalyst particles present in the SWNT bundles are taken into account, the calculated densities (solid line passing through crosses in Fig. 6.5(b)) are computed as described by equation (6.6). We also include the experimentally determined densities of

iso-SWNTs, acid-SWNTs and p-SWNTs in the same figure which agree reasonably well with the computed densities represented by the solid trace. Furthermore, our calculated density for a SWNT bundle in the absence of catalyst particles is in good agreement with that reported from a molecular dynamic simulation for a 10 nm diameter bundle [94]. As seen in Fig. 6.5(b), the computed density for bundled SWNTs in presence of catalyst particles is in good agreement with the experimental values. Thus it confirms the presence of catalyst particles in the SWNT bundles as seen in the TEM images (Fig. 6.4).

Next we discuss the density calculations for MWNTs. The density of MWNT can be computed in the continuum limit in which a MWNT is treated as a cylinder of thickness h and length L [103]. Therefore, the MWNT density can be expressed as:

$$\rho_{MWNT} = \frac{m}{V} = \frac{m_{MWNT}}{V_{MWNT}} = \frac{\rho_{graphite}\sum V_{W_i}}{L\pi\left(R_o^2 - R_i^2\right)} = \frac{\rho_{graphite} hL\sum_{i=1}^{n_w} \pi D_{w_i}}{L\pi\left(R_o^2 - R_i^2\right)} \tag{6.7}$$

where $\rho_{graphite}$ and h are the density and thickness of a single graphite layer (graphene). D_{wi} corresponds to the diameter of the i^{th} wall in the MWNT. R_i and R_o define the inner and outer radii of the MWNT (Fig. 6.5(c)). High resolution TEM studies showed that the interlayer space for a MWNT ranges from 0.34 to 0.39 nm, increasing with decreasing tube diameter. The distance D_{il} from one shell to the neighboring shell of a MWNT with diameter D is given by [102]:

$$D_{il} = 0.344 + 0.1e^{-\frac{D}{2}} \tag{6.8}$$

Note the diameters in equation (6.8) are in nm. The diameter of a MWNT with "i" number of walls is given by

$$D_{w_i} = 2R_i + 2(i-1)D_{il} = 2R_i + 2(i-1)\left(0.344 + 0.1e^{-\frac{D_{w_{i-1}}}{2}}\right)10^9 \tag{6.9}$$

where we substitute equations (6.8) in (6.9) so that the diameter of a MWNT with i number of walls is expressed in terms of the diameter of the $(i\text{-}1)^{th}$ wall. With equations (6.8) and (6.9) substituted in equation (6.7), the density of MWNT is given by,

$$\rho_{MWNT} = \frac{h\rho_{graphite}\sum_{i=1}^{n_W}\left[2R_i + 2(i-1)\left(0.344 + 0.1e^{-\frac{D_{w_{i-1}}}{2}}\right)10^9\right]}{\left(R_o^2 - R_i^2\right)} \tag{6.10}$$

As in the case of SWNTs, the presence of the catalyst particles need to be accounted in our model, for MWNTs before we compare our calculated densities to those obtained in our experiments the presence of the catalyst particles should be taken into account as

$$\rho_{measured} = \rho_{MWNT}\left(1 + \frac{m_{Catalyst}}{m_{Carbon}}\right) \tag{6.11}$$

The density of MWNT whose diameter distribution is shown in Fig. 6.4(c) is calculated to be 2.14 g/cm^3 using equation (6.11). This value is in good agreement with the other two theoretical predictions from [95] and [104] and is listed in Table 6.2. The densities of MWNT synthesized by CVD and electrical arc discharge used in this study are measured to be 2.09 and 2.11 g/cm^3, respectively.

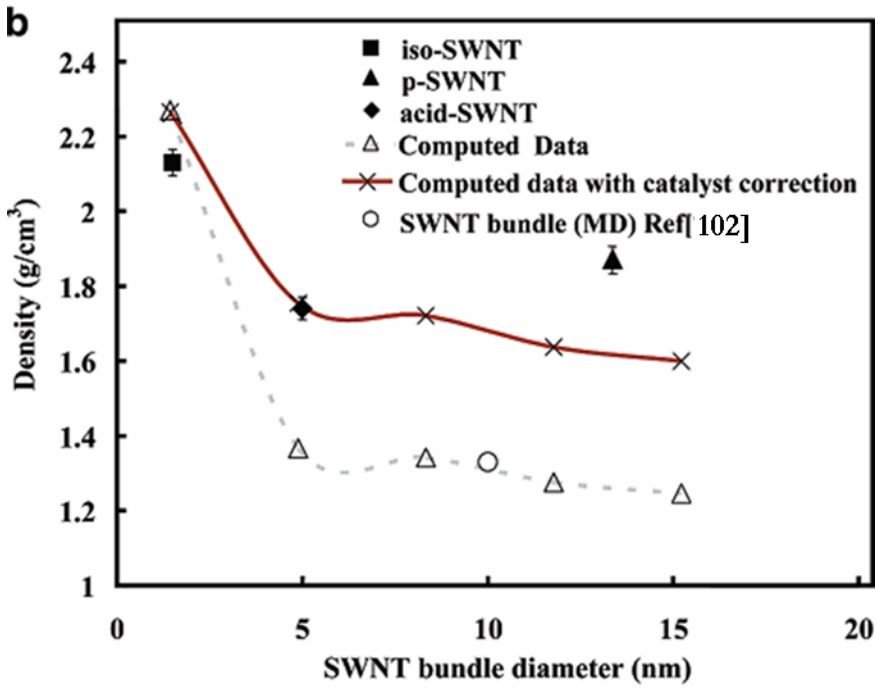

Figure 6.5(b): The density of SWNTs plotted as a function of the diameter of bundles. Both computational (crosses, open triangles, and open circle) and experimental (solid square, solid triangle, and solid diamond) densities are presented.

The density of acid-SWNT is measured to be 1.74 ± 0.04 g/cm^3, which is 0.13 g/cm^3 less than the density of p-SWNT (see Fig. 6.1 (a) and (b)). The decrease in the density can be attributed to the structural transformation from p-SWNT to acid-SWNT. The localized ultrasonication causing acidic oxidation disrupted the close-packed triangular lattice formation of individual p-SWNTs. The carboxyl groups formed subsequently at the ends and sides of the tubes made individual tubes hydrophilic thus separating from each other in the water network. The scattered spatial disposition reduced

the density. In case of MWNTs we observed two bands, one close to the meniscus corresponding to amorphous carbon and the second corresponding to MWNTs. However, among all CNT structures, iso-SWNTs have the highest density (as can be seen in Table 6.1).

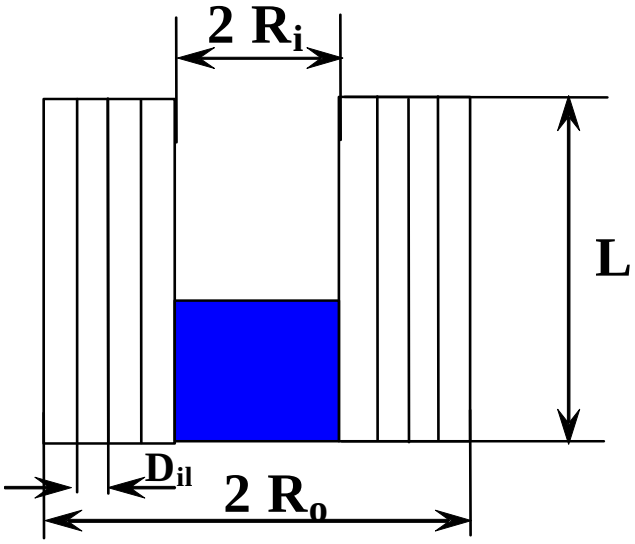

Figure 6.5(c). Illustration of MWNT based on the continuum hypothesis. The multi-shells are treated as a continuum medium with thickness *h* and length *L*.

Density (g/cm^3)	outer tube diameter (nm)	inner tube diameter (nm)	Source
2.16	33.6	~ 10	[104]
~ 2.1	8 - 15	3 – 5	[95]
2.14	50	10	model (this work)
2.09	48	~ 10	measured density for CVD-grown MWNTs (this work)
2.11	50	~ 15	measured density for electric arc-grown MWNTs (this work)

Table 6.2: Measured and Computed Densities of MWNTs compared with those reported in the literature.

Measuring resonance in a nanocantilever (MWNT) using HDR

To test the limits of sensitivity offered by our HDR technique, the former post doctorate (Jay Gaillard) [105] in our group measured the resonant frequency and phase for cantilevered MWNTs. A MWNT was mounted on a sharpened gold-coated W probe tip by applying a dc voltage (~3-7 V) between the tip and a mat of MWNTs on a SEM tape. The MWNT was manipulated parallel to a gold-coated W tip (counter electrode) over the dark field microscope with ~ < 1 μm gap distance (the same geometry reported in chapter 3 for Si microcantilever). The MWNTs used in this study were grown by a chemical vapor deposition method described earlier with an average diameter of ~ 50 nm [99].

Figure 6.6 displays typical resonance and phase (shown in green open circles) spectra for a MWNT. To verify the amplitude peak corresponding MWNT, the signal (shown in red solid circles) in Fig. 6.6 in the absence of the MWNT for the same tungsten probe geometry was compared with the amplitude signal (shown in blue solid circles) with MWNT.

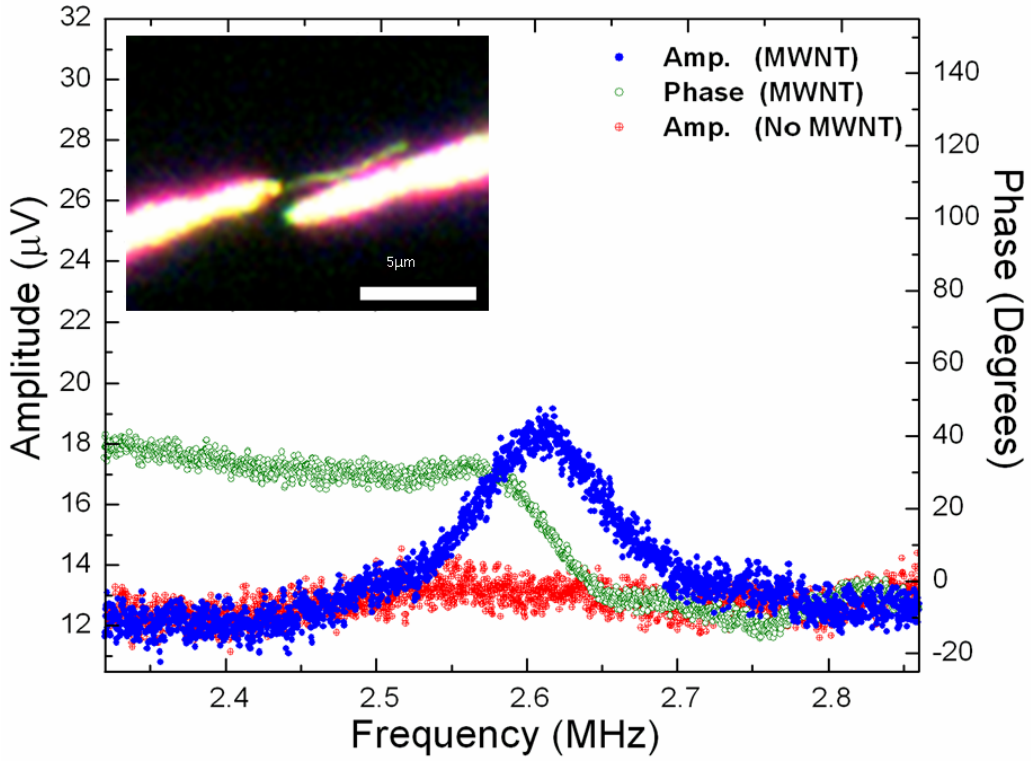

Figure 6.6: The amplitude (solid circles) and phase (open circles) spectra of a MWNT (7 µm long and 50 nm in diameter) near resonance measured under ambient conditions. The inset shows an optical dark field image of the MWNT placed parallel to the W tip (counter electrode) with 5 µm scale bar [2].

The second former post doctorate (Razvan Ciocan) [1] used a slightly different geometry between the MWNT and W probe tip acting as a counter electrode for measuring the resonance of MWNT. In this case, a gold-coated W probe tip is brought in close proximity to and aligned with the MWNT over a dark field optical microscope as shown in Fig. 6.7(a) An ac voltage (V_{ac}) along with a dc voltage (V_{dc}) applied to counter electrode induce charges on the MWNT. The electrostatic force, (F_C) between the charges residing on the MWNT and the counter electrode causes the MWNT to oscillate (see Fig. 6.7(b)).

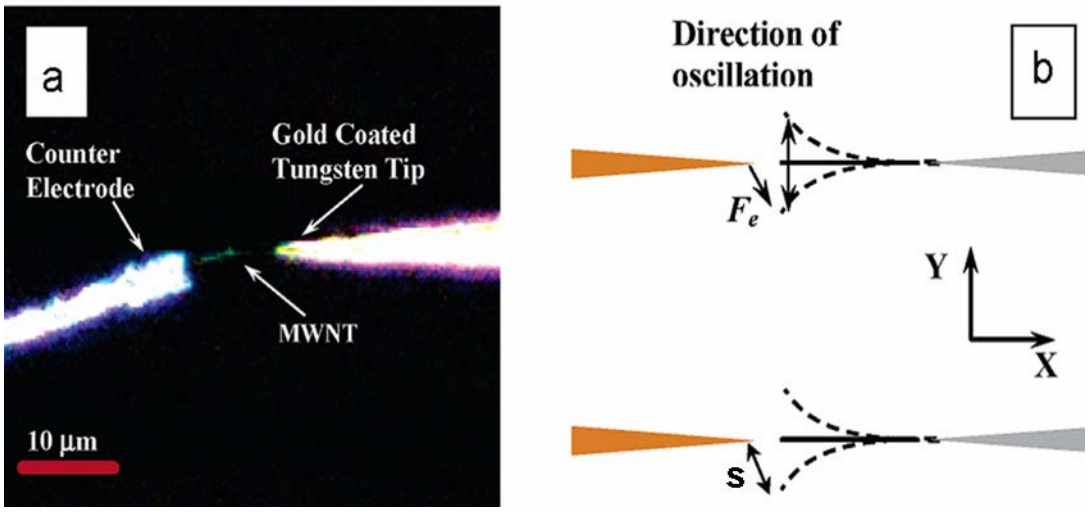

Figure 6.7 (a): Dark field microscope image of the geometrical setup for the MWNT and the counter electrode assembly. The MWNT is facing the end of counter electrode in its very close proximity (see text). (b) A schematic of mechanical oscillations induced in a MWNT by the force (F_C), when the MWNT and the counter electrode are separated by a distance (s).

The typical resonance spectra for a CVD grown MWNT (10 μm long and 57 nm in diameter) is shown in Fig. 6.7 (c). The resonant frequency at second mode for a MWNT is around 2.42 MHz. No noticeable changes in the traces for the amplitude (dark circles) and phase (dark triangles) can be discerned near resonance when the MWNT is absent.

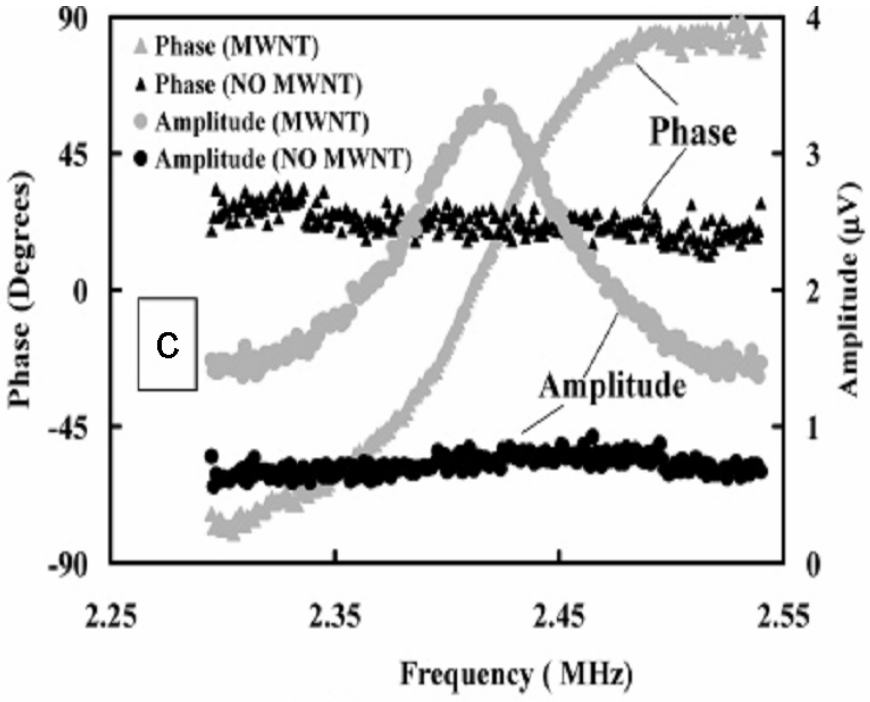

Figure 6.7 (c): The amplitude (light circles) and phase (light triangles) spectra near the resonance of MWNT. The amplitude (dark circles) and phase (dark triangles) signals obtained for the same geometry of W probe tip in the absence of MWNT.

For a MWNT clamped at one end, the resonant frequency (f_i) of the ith mode of vibration is given by [51],

$$f_i = \frac{\beta_i^2}{8\pi}\frac{1}{L^2}\sqrt{\frac{(D_i^2 + D_O^2)E}{\rho}} \tag{6.12}$$

where L is the tube length, D_o and D_i are the outer and inner tube diameters, respectively. ρ is the density of the MWNT and the β_i values are determined from the boundary conditions to be $\beta_1 = 1.875$, $\beta_2 = 4.694$, and $\beta_3 = 7.855$ [51].

The experimentally measured resonant frequency of the MWNT (L = 10 μm, D_i = 17 nm and D_0 = 57 nm) at second mode is 2.42MHz as seen in Fig. 6.7 (c). The density of a MWNT used for this calculation is determined using gradient sedimentation method and listed in Table 6.2 as ρ = 2110 kg/m^3. The bending modulus (E) of this MWNT is computed using equation 6.12. Since three resonant frequencies are measured, three values of E are calculated. A least squares fit to the data and gives $E \sim 29.6$ GPa [1].

Conclusions

The densities of carbon nanotube samples having various structures were determined precisely with the equilibrium density gradient sedimentation technique using sodium metatungstate as the gradient-generating agent. Bundled, isolated and acid-treated SWNTs and MWNTs formed sharp well-defined bands at the respective densities. This can be attributed to the differences in structural features of CNTs resulting in distinguishable differences in densities. Transmission electron microscopy (TEM) and

micro-Raman spectroscopy provided significant evidence to confirm the structure of the material in each band. The measured densities for bundled, isolated, and acid-treated SWNTs and MWNTs are 1.87, 2.13, 1.74, and 2.1 g/cm^3 respectively. These were found to be in good agreement with the theoretical computations based on their structures. HDR is an appropriate method to electrically actuate and detect resonances in nanoscale cantilevers. Besides leading to nanoscale sensors, HDR is a powerful tool for determining fundamental mechanical properties of 1D materials. As an example, the Young's modulus of CNTs has been discussed in this chapter. The key parameter, viz. the density of CNTs, required in equation (6.12) was obtained by the gradient sedimentation method.

APPENDICES

Appendix A

Procedure for making sensor chip

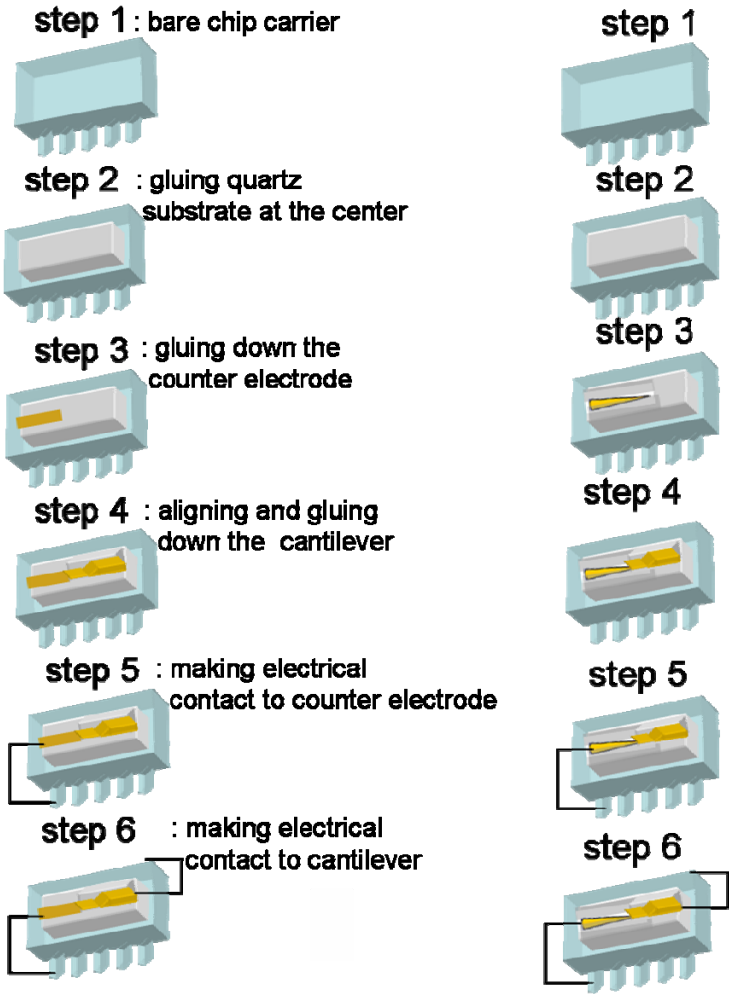

Figure A-1: A schematic diagram showing all the steps involved in the procedure for fabricating a sensor chip with two geometries for the electrodes. The left series show the geometry wherein a rectangular gold strip acts as counter electrode whereas a tungsten tip acting as counter electrode is depicted in the right series.

Two different geometries for the electrodes were developed and tested for experiments described in this dissertation. The schematic of each step is shown in Fig. A-1. In the first geometry, we start with a commercially available rectangular chip carrier (0.5″× 0.3″) on which a quartz substrate (0.3″ × 0.2″) is glued using the 5 minute epoxy (step 2). Next, a rectangular strip (0.15″ × 0.0014″) of gold (~ 80-100 nm thick) is fabricated using standard masking wire technology and thin film evaporation (step 3). This thin rectangular strip of gold acts as a counter electrode (Fig.A-1, left series). With the help of a dark field microscope and a XYZ stage, a gold coated silicon microcantilever (Micromasch, 35 μm wide, 2 μm thick and 350 μm long) is brought close to the counter electrode and aligned parallel to the counter electrode with a gap distance of ~ 8-10 μm. The HDR signals are monitored and the microcantilever position is adjusted until a maximum signal is obtained (step 4). Then the cantilever is glued, and the electrical contacts to the chip carrier are established (steps 5 and 6). Subsequently, we had to develop an improved design for the counter-electrode since the field between the gold stripe and the microcantilever often led to undesirable snapping of the microcantilever into the gold stripe when driven into resonance at small gap distances. This problem was overcome by using a conical-shaped tungsten tip (discussed in Appendix B) as the counter electrode. Therefore, in our improved design we adopt an identical procedure wherein the conical tip is first glued to the chip carrier, and the microcantilever is manipulated and glued after strong HDR signals are obtained (Fig.A-1, right series). This chip design was used for all experiments discussed in this dissertation.

Appendix B

Procedure for etching tungsten probe tips

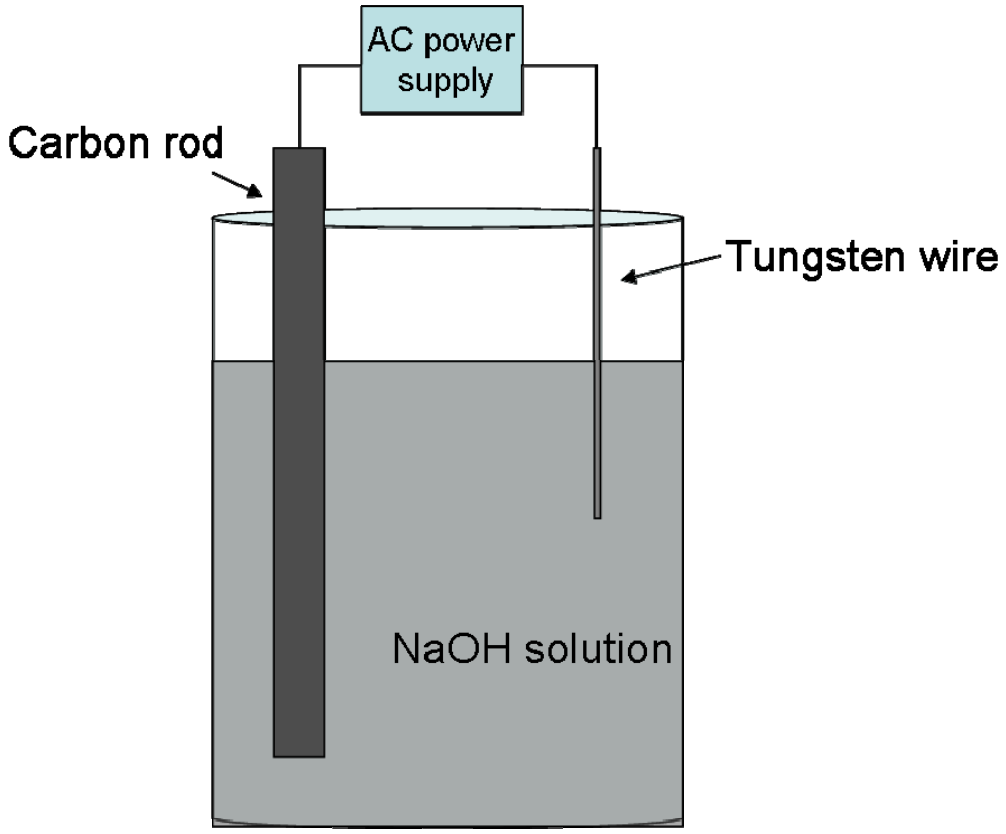

Figure B-1: A Schematic of tungsten wire immersed in NaOH solution with a carbon rod serving as an electrode. The tungsten tip etches from the bottom to the desired length in this solution

The schematic for etching a tungsten tip is illustrated in Fig. B.1. A carbon rod (dia. ~ 3 mm) serves as an one of the electrodes in a electrolyte (2 M NaOH solution in

de-ionized water) contained in a glass beaker. A 0.1 mm dia., tungsten wire is dipped into this solution such that its tip is about 1 inch below the surface of the solution. The ac voltage applied across the carbon rod and tungsten wire is controlled using a variac and it results in a current flow between the wire and the rod. During the etching process, bubbles rapidly form around the immersed wire making it difficult to see its tip. After about 30 seconds of etching, the wire begins to reduce in length and diameter. When its dipped length is etched from 1 inch to few (2-5) mm, the tip acquires a very sharp profile. This method can easily etch the ends of the tips to ~100 nm in diameter and the sharpest tip that we have etched in our lab so far is about 15 nm in diameter. The process takes less than a minute, which allows the user to etch a large number of tips in a short period of time. After etching the sharp tips, each tip is subjected to a three step cleaning process. In first step, the tip is dipped in deionized water to dilute the NaOH followed by rinsing with acetone which completely cleans off the residual NaOH. Finally it is again dipped in purified water to clean off the acetone (since acetone leaves behind residue).

Appendix C

Operating principle of Mass flow controllers

Figure C-1: Alicat Scientific Mass flow controller used in order to control the flow rates of different gases under study during our measurements. By clicking the MODE button on the display we select the particular gas and on the next screen enter the required flow rate [106].

We have used 16 Series Mass and Volumetric Precision Gas Flow Controller (Fig. C-1) for all our measurements reported in chapter 5. All M and V Series Gas Flow Meters are based on the accurate measurement of volumetric flow. The volumetric flow rate is determined by creating a pressure drop across a unique internal restriction, known

as a Laminar Flow Element (LFE), and measuring the differential pressure across it. The restriction is designed so that the gas molecules are forced to move in parallel paths along the entire length of the passage; hence laminar (streamline) flow is established for the entire range of operation of the device. In order to get an accurate volumetric flow rate, the gas whose flow rate is being measured must be selected in the menu. This is important because the device calculates the flow rate based on the viscosity of the gas at the measured temperature. If the gas that is being measured is not what is selected in the menu, an incorrect value for the viscosity of the gas will be used in the calculation of flow, and the resulting output will be inaccurate in direct proportion to the difference in the two gases viscosities.

Therefore, while studying the effect of deuterium (D_2) on the response of vibrating microcantilever in chapter 5, an equivalent flow rate of hydrogen (H_2) was calculated by taking into account the viscosities of H_2 and D_2.

$$\frac{Q_{H_2}}{Q_{D_2}} = \frac{\eta_{D_2}}{\eta_{H_2}} \tag{C.1}$$

where Q is volumetric flow rate and η is the absolute viscosity of the particular gas. Substituting Q_{D2} = 100 sccm, η_{D2} = 0.0001185 poise and η_{H2} = 0.0000865 poise in equation (C.1), we calculated the equivalent flow rate of H_2. As D_2 is not listed in the select gas menu, we selected H_2 in the menu of the mass flow controller and adjusted the flow rate to 139 sccm in order to get 100 sccm of deuterium.

Appendix D

Equipment List

1. Stanford Research Systems SR 830 Lock-in Amplifier.

2. Stanford Research Systems DS345, 30 MHz synthesized Functional generator.

3. Amptek (A-250) charge sensitive pre-amplifier.

4. Epiphot 200 dark field/bright field microscope with a 50x, 8.4 mm long working distance objective lens.

5. TRIAX 550 single-grating Raman spectrometer (groove density 1200 grooves/mm) equipped with a liquid nitrogen-cooled charge-coupled device (CCD).

6. Beckman centrifuge with SW56 rotor.

7. Hitachi 7600 Transmission electron microscope.

REFERENCES

[1] R. Ciocan *et al.*, Nano Lett. **5**, 2389 (2005).

[2] J. Gaillard *et al.*, Rev. Sci. Instrum. **77**, 073907 (2006).

[3] G. Keskar *et al.*, Sens. Actuators A (2008).

[4] G. Keskar *et al.*, IEEE Sensors J. (2008).

[5] G. Keskar *et al.*, Sens. and Transducers **91**, 1 (2008).

[6] H. L. Tuller, and R. Micak, Current Opinion in Solid State & Materials Science **3**, 501 (1998).

[7] V. L. Nickolay, J. S. Michael, and G. D. Panos, Review of Scientific Instruments **75**, 2229 (2004).

[8] C. Ziegler, Anal Bioanal Chem **379**, 946 (2004).

[9] D. Then, A. Vidic, and C. Ziegler, Sensors and Actuators B-Chemical **117**, 1 (2006).

[10] P.G. Datskos, T.Thundat, and V. L. Nickolay, Encyclopedia of Nanoscience and Nanotechnology **5**, 551 (2004).

[11] P. L. and, and X. Li, J. Micromech. Microeng. **16**, 2539 (2006).

[12] F. M. Battiston *et al.*, Sensors and Actuators B-Chemical **77**, 122 (2001).

[13] T. Thundat, a. P. I. Oden, and R. J. Warmack, *Microcantilever Sensors* (Microscale Thermophysical Engineering, 1997), Vol. 1, p. 185.

[14] P. I. Oden *et al.*, Appl. Phys. Lett. **68**, 3814 (1996).

[15] J. Fritz *et al.*, Science **288** (2000).

[16] M. K. Baller *et al.*, Ultramicroscopy **82**, 1 (2000).

[17] R. Raiteri, and H. J. Butt, Journal of Physical Chemistry **99**, 15728 (1995).

[18] S. J. Oshea *et al.*, Journal of Vacuum Science & Technology B **14**, 1383 (1996).

[19] D. R. Baselt, G. U. Lee, and R. J. Colton, Journal of Vacuum Science & Technology B **14**, 789 (1996).

[20] Z. Y. Hu, T. Thundat, and R. J. Warmack, Journal of Applied Physics **90**, 427 (2001).

[21] T. Thundat *et al.*, Applied Physics Letters **64**, 2894 (1994).

[22] P. G. Datskos, and I. Sauers, Sensors and Actuators B-Chemical **61**, 75 (1999).

[23] H. P. Lang *et al.*, Analytica Chimica Acta **393**, 59 (1999).

[24] D. Lange *et al.*, in Smart Structures and Materials1998), pp. 233.

[25] R. Berger *et al.*, Microelectronic Engineering **35**, 373 (1997).

[26] T. Thundat *et al.*, Applied Physics Letters **66**, 1695 (1995).

[27] T. Thundat *et al.*, Applied Physics Letters **66**, 1563 (1995).

[28] C. Rossel *et al.*, Journal of Applied Physics **79**, 8166 (1996).

[29] R. P. Cowburn, A. M. Moulin, and M. E. Welland, Applied Physics Letters **71**, 2202 (1997).

[30] S. Porthun, L. Abelmann, and C. Lodder, Journal of Magnetism and Magnetic Materials **182**, 238 (1998).

[31] C. F. Q. G. Binning, C. Gerber, Phys. Rev. Lett **56** (1986).

[32] R. Berger *et al.*, Applied Physics Letters **69**, 40 (1996).

[33] J. R. Barnes *et al.*, Nature **372**, 79 (1994).

[34] J. K. Gimzewski *et al.*, Chemical Physics Letters **217**, 589 (1994).

[35] Rüdiger Berger *et al.*, Science **276** (1997).

[36] R. Berger *et al.*, Chemical Physics Letters **294**, 363 (1998).

[37] H. Wenhai, S. M. Lindsay, and J. Tianwei, Applied Physics Letters **69**, 4111 (1996).

[38] A. Schemmel, and H. E. Gaub, Review of Scientific Instruments **70**, 1313 (1999).

[39] F. Ernst-Ludwig *et al.*, Review of Scientific Instruments **65**, 639 (1994).

[40] M. A. Lantz, S. J. O. Shea, and M. E. Welland, Applied Physics Letters **65**, 409 (1994).

[41] R. Irene, and P. Roger, Journal of Applied Physics **87**, 526 (2000).

[42] S. J. O'Shea *et al.*, Nanotechnology **16**, 602 (2005).

[43] J. Teva *et al.*, Ultramicroscopy **106**, 808 (2006).

[44] I. Voiculescu *et al.*, Ieee Sensors Journal **5**, 641 (2005).

[45] D. Rugar, H. J. Mamin, and P. Guethner, Applied Physics Letters **55**, 2588 (1989).

[46] G. Meyer, and N. M. Amer, Applied Physics Letters **53**, 1045 (1988).

[47] P. Poncharal *et al.*, Science **283**, 1513 (1999).

[48] M.-F. Yu *et al.*, Physical Review B **66**, 073406 (2002).

[49] S. T. Purcell *et al.*, Physical Review Letters **89**, 276103 (2002).

[50] J. Gaillard, M. Skove, and A. M. Rao, Applied Physics Letters **86**, 233109 (2005).

[51] Z. L. Wang, P. Poncharal, and W. A. de Heer, Pure and Applied Chemistry **72**, 209 (2000).

[52] P. I. Oden *et al.*, Applied Physics Letters **69**, 3277 (1996).

[53] M. Tortonese, R. C. Barrett, and C. F. Quate, Applied Physics Letters **62**, 834 (1993).

[54] V. Ferrari *et al.*, Ieee Transactions on Ultrasonics Ferroelectrics and Frequency Control **43**, 601 (1996).

[55] D. L. DeVoe, and A. P. Pisano, Journal of Microelectromechanical Systems **6**, 266 (1997).

[56] C. L. Britton *et al.*, Ultramicroscopy **82**, 17 (2000).

[57] J. Verd *et al.*, Journal of Microelectromechanical Systems **14**, 508 (2005).

[58] G. Abadal *et al.*, Nanotechnology **12**, 100 (2001).

[59] K. L. Ekinci, and M. L. Roukes, Review of Scientific Instruments **76**, 061101 (2005).

[60] M. D. Ventra, S. Evoy, and J. R. Helfin, *Introduction to Nanoscale Science and Technology* (Springer, New York, 2004), pp. 405.

[61] J. F. Nye, *Physical properties of crystal* (Oxford press, 1957), p. 144.

[62] M. P. Blencowe, and M. N. Wybourne, Applied Physics Letters **77**, 3845 (2000).

[63] A. Bertz *et al.*, Sensors and Actuators a-Physical **93**, 163 (2001).

[64] J.D. Taylor *et al.*, in *Frontiers in Nanoscience and Nanotechnology*, edited by A. N.,Y. Fu (Oxford University Press 2008).

[65] http://www.angelfire.com/electronic2/spm/etching.html

[66] S. Bianco *et al.*, J. Vac. Sci. Technol. B **24**, 1803 (2006).

[67] S. Weigert, a. M. Dreier, and M. Hegner, Appl. Phys. Lett. **69**, 2834 (1996).

[68] F. Shen *et al.*, Sens. Actuators A **95**, 17 (2001).

[69] R. Sandberg *et al.*, J. Micromech. Microeng. **15**, 1454 (2005).

[70] J. Mertens *et al.*, Ultramicroscopy **97**, 119 (2003).

[71] F. R. Blom *et al.*, J. Vac. Sci. Technol. B **10**, 19 (1992).

[72] L. D. L. and, and E. M. Lifshitz, *Course of Theoritical Physics* (Butterworth Washington, DC/Heinemann, London, 1987), Vol. 6.

[73] R. G. Christian, Vacuum **16**, 175 (1966).

[74] A. B. Pippard, *The Physics of Vibration* (Cambridge University Press, Cambridge, 1978), Vol. 1, p. 252.

[75] H. Hosaka, K. Itao, and S. Kuroda, Sensors and Actuators a-Physical **49**, 87 (1995).

[76] D. Sarid, *Scanning Force Microscopy* (Oxford, New York, 1994), p. 169.

[77] A. Isacsson, J. M. Kinaret, and R. Kaunisto, Nanotech. **18**, 195203 (2007).

[78] S. Zaitsev *et al.*, IEEE proceedings (2006).

[79] H. W. Ch. Postma *et al.*, App. Phys. Lett **86**, 223105 (2005).

[80] I. Kozinsky *et al.*, App. Phys. Lett **88**, 253101 (2006).

[81] R. Almog *et al.*, Phys. Rev. Lett **98**, 078103 (2007).

[82] S. K. De., and a. N. R. Aluru, J. Microelectromech. Sys. **15**, 355 (2006).

[83] A. H. Nayfeh, and D. T. Mook, *Nonlinear oscillations* (Wiley - Interscience, 1995), pp. 163.

[84] M. V. Requa, and K. L. Turner, App. Phys. Lett **88**, 263508 (2006).

[85] J. J. Yao, and N. C. MacDonald, J. Micromech. Microeng. **6**, 257 (1996).

[86] J. S. Aldridge, and A. N. Cleland, Phys. Rev. Lett. **94**, 156403 (2005).

[87] L. A. Pinnaduwage *et al.*, Appl. Phys. Lett. **83**, 1471 (2003).

[88] Certified Air Safety (http://www.certifiedairsafety.com).

[89] B. Plewinsky, and R. Kamps, Makromolekulare Chemie-Macromolecular Chemistry and Physics **185**, 1429 (1984).

[90] M. Terrones, Annual Review of Materials Research **33**, 419 (2003).

[91] J. Chen *et al.*, Science **282**, 95 (1998).

[92] S. Ciraci *et al.*, Journal of Physics-Condensed Matter **16**, R901 (2004).

[93] D. Tasis *et al.*, Chemical Reviews **106**, 1105 (2006).

[94] G. H. Gao, T. Cagin, and W. A. Goddard, Nanotechnology **9**, 184 (1998).

[95] Q. Huang *et al.*, Journal of Materials Chemistry **15**, 1995 (2005).

[96] Manual of Weighing Applications, Part 1; Sartorius AG: Gottingen,,Germany, 2004.See http://www.sartorius.com/fileadmin/sartorius_pdf/ Prospekt/englisch/DensityDeterminationManual.pdf.

[97] Q. Lu *et al.*, Journal of Physical Chemistry B **110**, 24371 (2006).

[98] K. A. Williams *et al.*, Nature **420**, 761 (2002).

[99] R. Andrews *et al.*, Chemical Physics Letters **303**, 467 (1999).

[100] R. B. Mathur *et al.*, in *National Conference on Carbon, Indo-Carbon*2001), p. 226.

[101] A. M. Rao *et al.*, Science **275**, 187 (1997).

[102] C. H. Kiang *et al.*, Physical Review Letters **81**, 1869 (1998 http://www.wag.caltech.edu/foresight/foresight_2.html.).

[103] S. Govindjee, and J. L. Sackman, Solid State Communications **110**, 227 (1999).

[104] D. Qian *et al.*, Applied Physics Letters **76**, 2868 (2000).

[105] J. B. Gaillard, in *Department of Physics and Astronomy* (Clemson University, Clemson, 2006).

[106] Alicat Scientific (http://www.alicatscientific.com).